UNIVERSITAT POLITÈCNICA DE CATALUNYA

Escola Tècnica Superior

d'Enginyeria de Camins, Canals i Ports de Barcelona

Institut Flumen – CIMNE

PHD DISSERTATION

SPACEBORNE SAR IMAGERY FOR MONITORING THE INUNDATION IN THE DOÑANA WETLANDS

Author:

Belén Martí-Cardona

Advisor:

Dr. Josep Dolz Ripollés

Co-advisor:

Dr. Carlos López Martínez

Dissertation submitted to obtain the degree of

DOCTOR OF PHILOSOPHY
BY THE UNIVERSITAT POLITÈCNICA DE CATALUNYA

CIVIL ENGINEERING PROGRAM

Barcelona, April 2014

ANNEXES

Annex 1:
Flood Maps for the 2006-2007 Hydrologic Year

This Annex includes twenty-two flood maps showing the flood extent evolution in the Doñana wetlands during the 2006-2007 hydrologic cycle. The flood maps were produced from Envisat/ASAR imagery following the methodology presented throughout this document and evidence the utility of the SAR imagery and the proposed method for the detail monitoring of the inundation in the Doñana marshes.

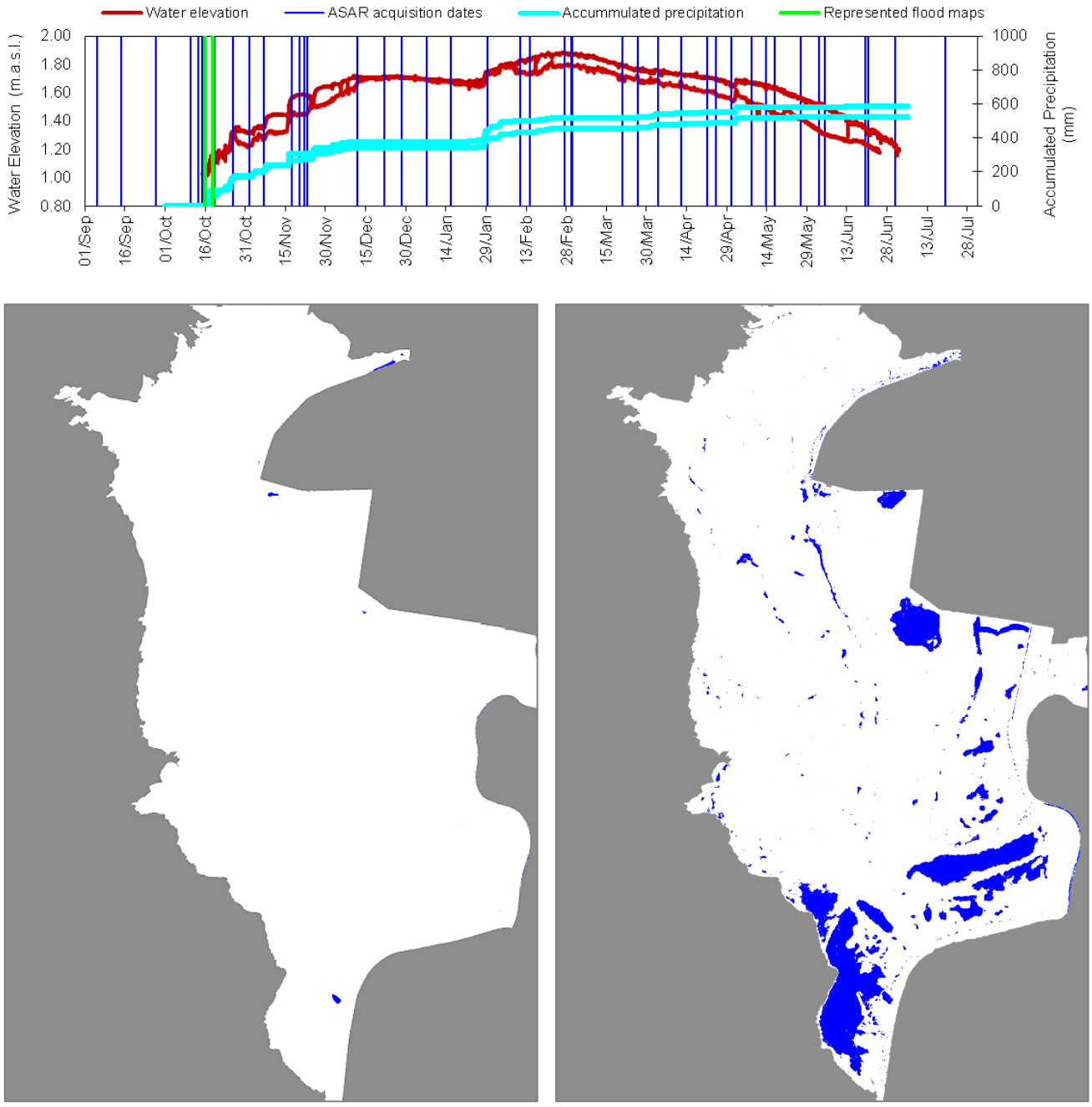

16 October 2006 19 October 2006

Fig. A1.1. Water elevation and accumulated precipitation evolution in the Doñana wetland during the 2006-2007 hydrologic year. Flood maps derived from Envisat/ASAR scenes for the two dates highlighted in green on the water elevation evolution chart.

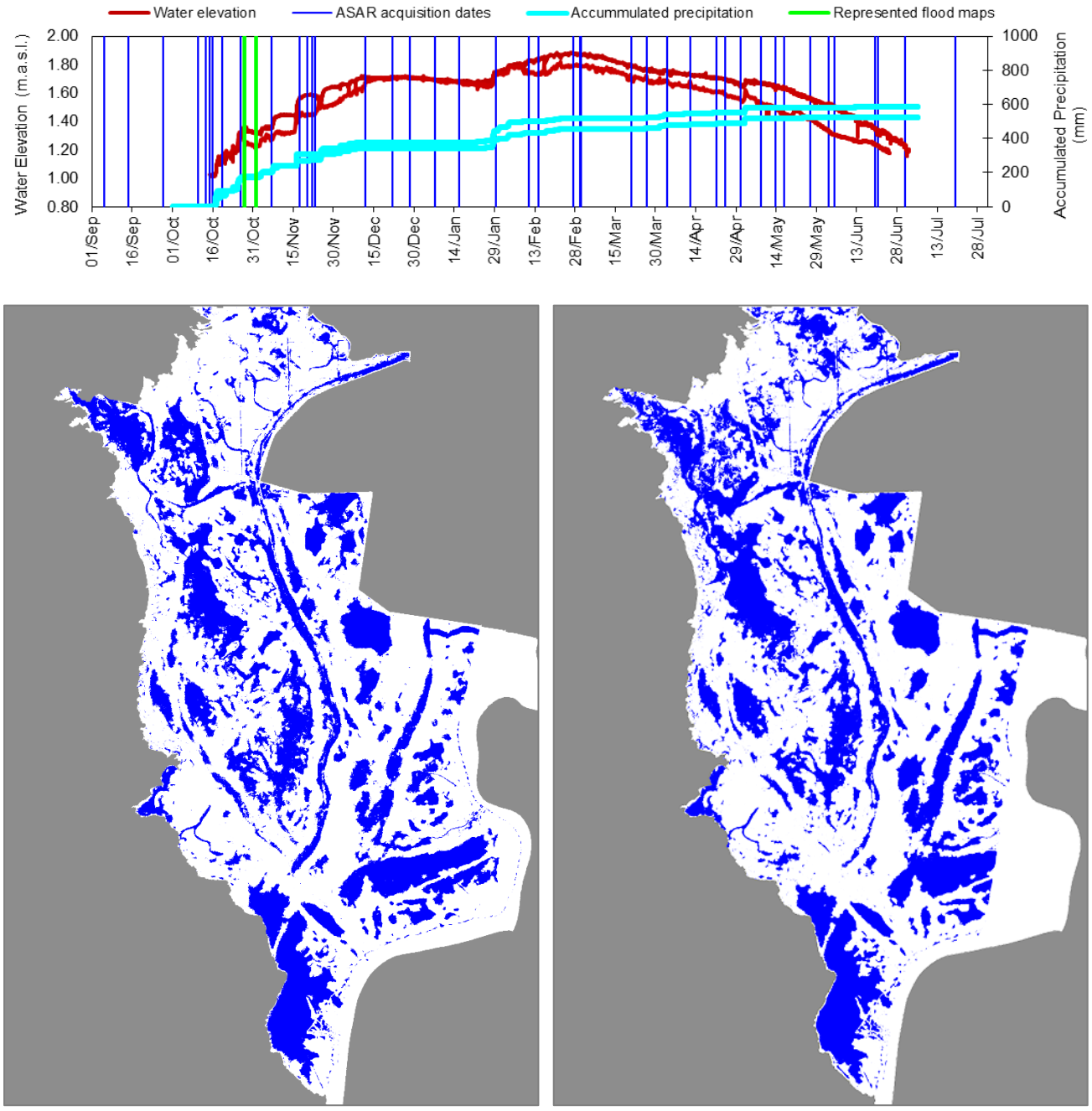

28 October 2006 1 November 2006

Fig. A1.2. Water elevation and accumulated precipitation evolution in the Doñana wetland during the 2006-2007 hydrologic year. Flood maps derived from Envisat/ASAR scenes for the two dates highlighted in green on the water elevation evolution chart.

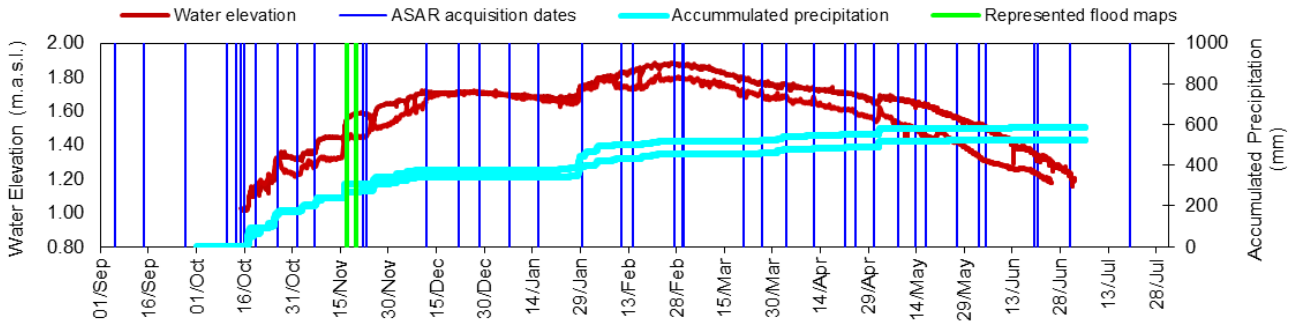

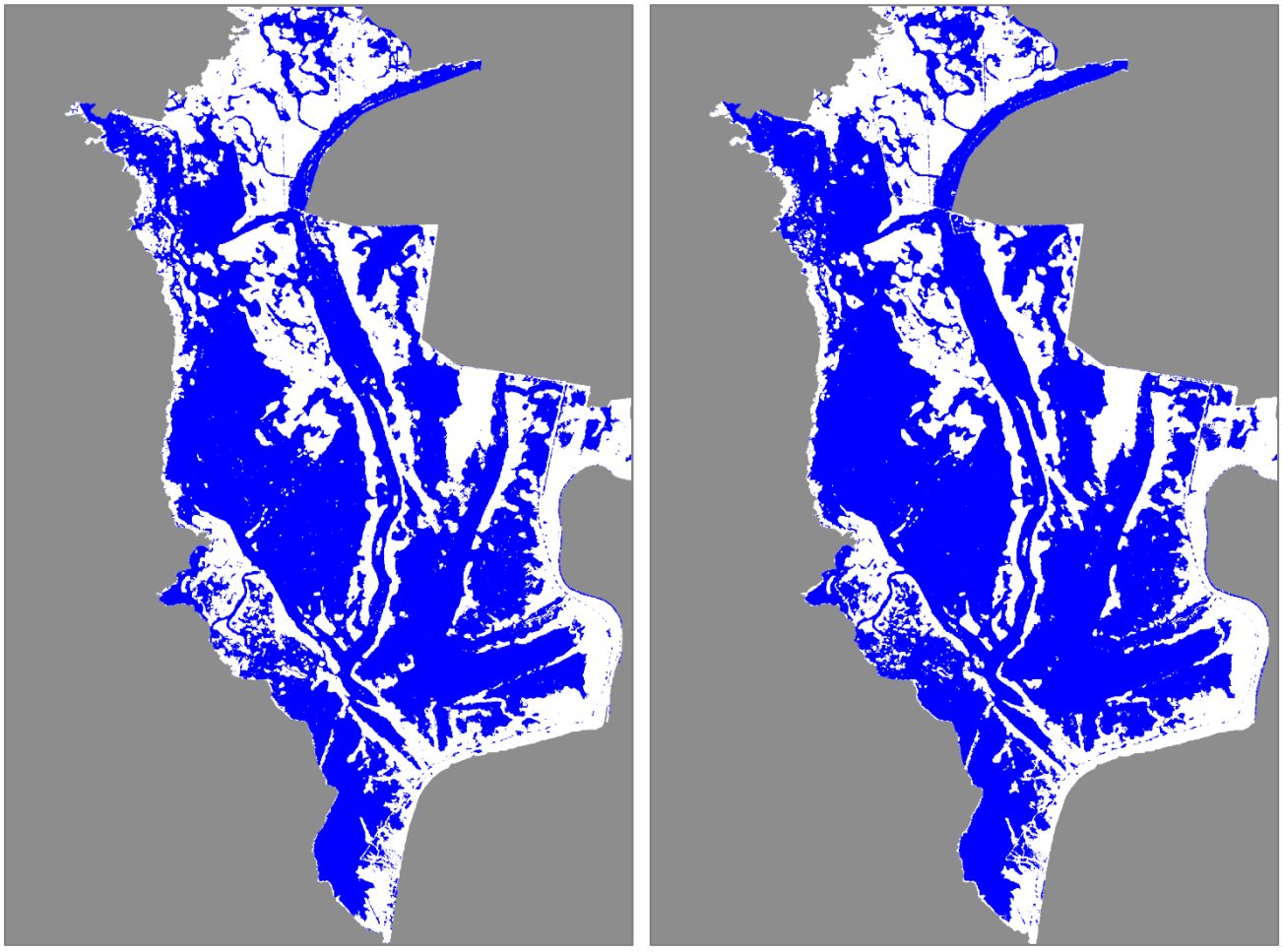

17 November 2006 20 November 2006

Fig. A1.3. Water elevation and accumulated precipitation evolution in the Doñana wetland during the 2006-2007 hydrologic year. Flood maps derived from Envisat/ASAR scenes for the two dates highlighted in green on the water elevation evolution chart.

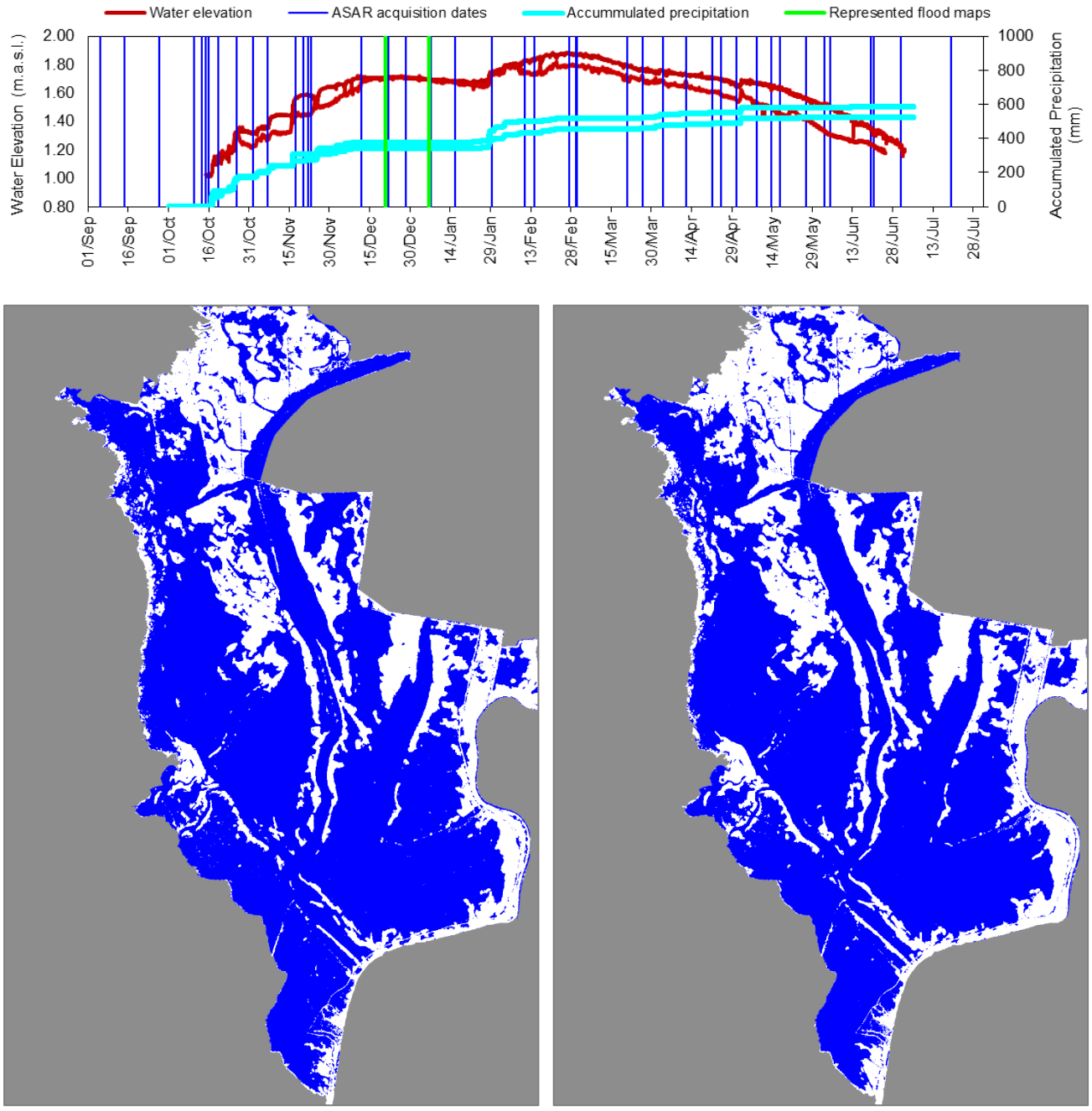

21 December 2006

6 January 2007

Fig. A1.4. Water elevation and accumulated precipitation evolution in the Doñana wetland during the 2006-2007 hydrologic year. Flood maps derived from Envisat/ASAR scenes for the two dates highlighted in green on the water elevation evolution chart.

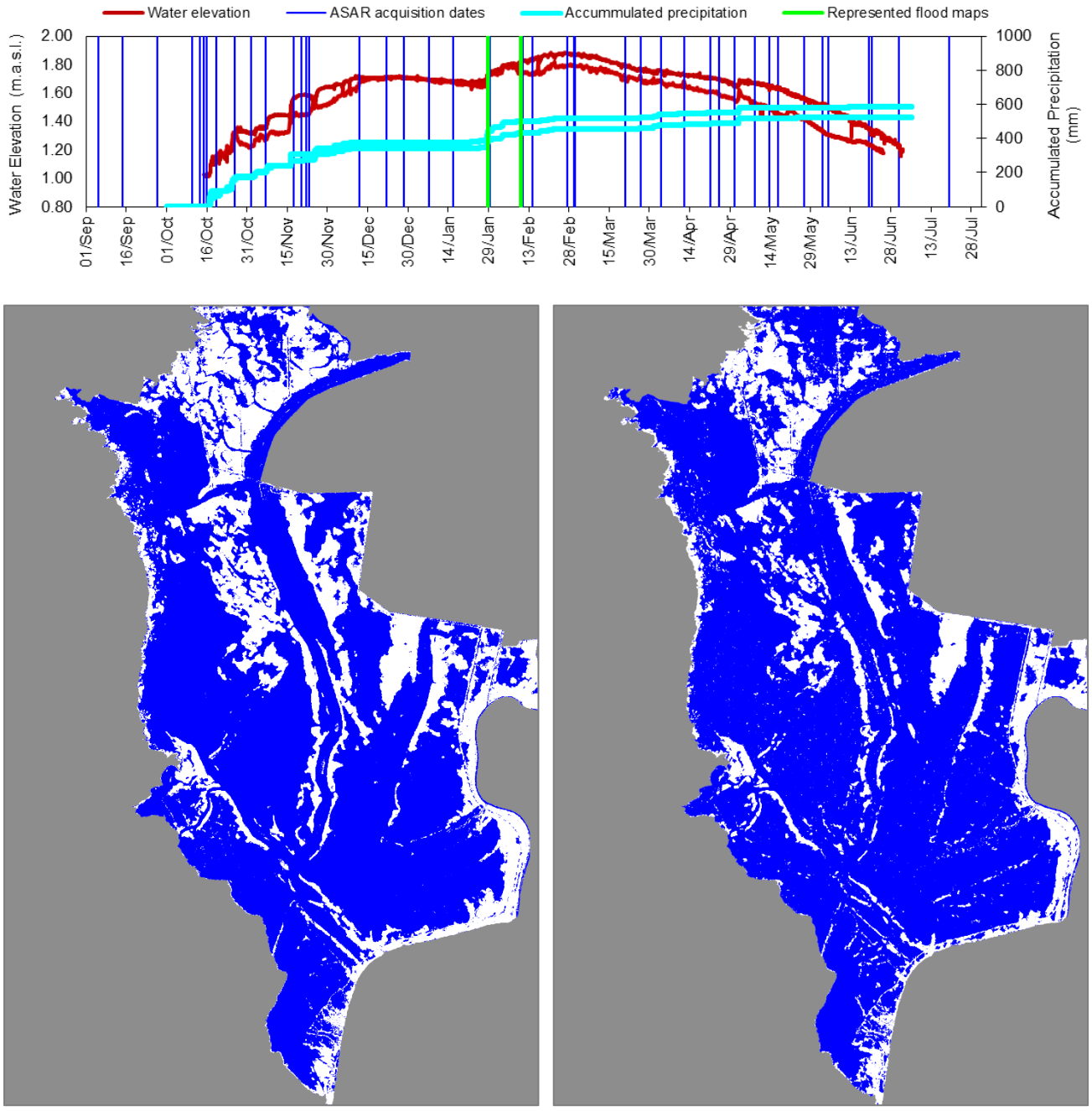

29 January 2007 10 February 2007

Fig. A1.5. Water elevation and accumulated precipitation evolution in the Doñana wetland during the 2006-2007 hydrologic year. Flood maps derived from Envisat/ASAR scenes for the two dates highlighted in green on the water elevation evolution chart.

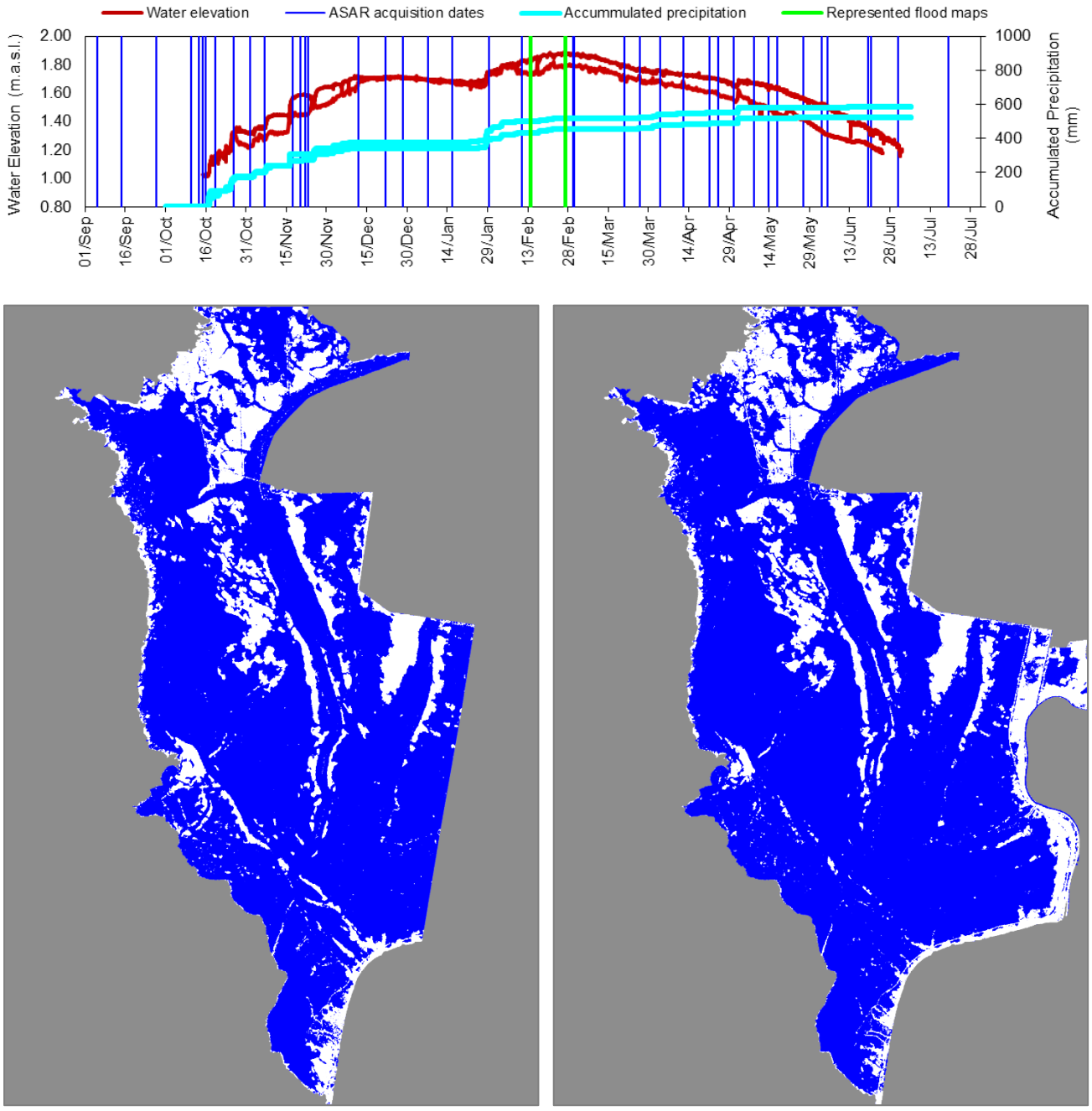

14 February 2007

27 February 2007

Fig. A1.6. Water elevation and accumulated precipitation evolution in the Doñana wetland during the 2006-2007 hydrologic year. Flood maps derived from Envisat/ASAR scenes for the two dates highlighted in green on the water elevation evolution chart.

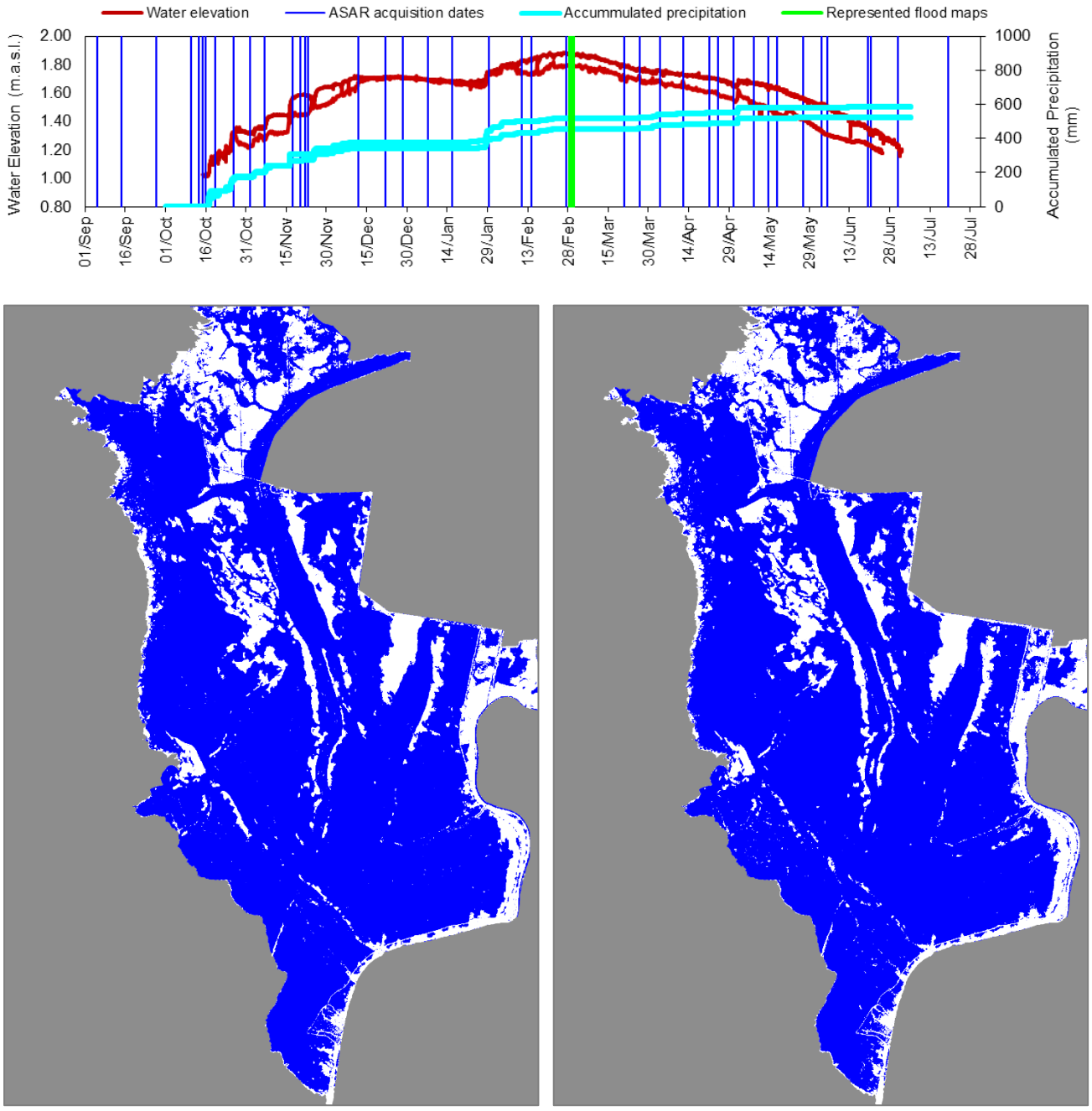

1 March 2007 2 March 2007

Fig. A1.7. Water elevation and accumulated precipitation evolution in the Doñana wetland during the 2006-2007 hydrologic year. Flood maps derived from Envisat/ASAR scenes for the two dates highlighted in green on the water elevation evolution chart.

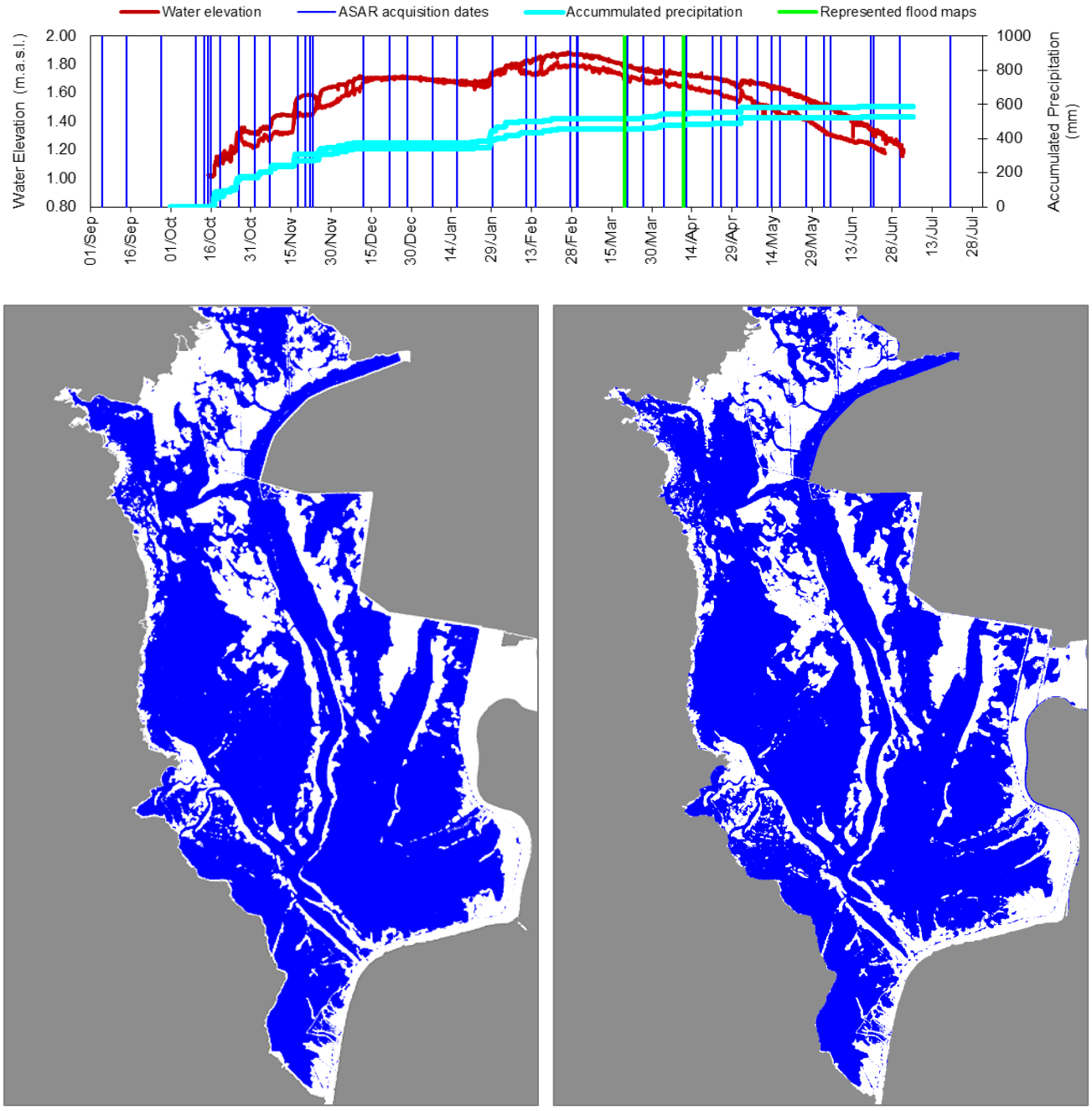

20 March 2007 11 April 2007

Fig. A1.8. Water elevation and accumulated precipitation evolution in the Doñana wetland during the 2006-2007 hydrologic year. Flood maps derived from Envisat/ASAR scenes for the two dates highlighted in green on the water elevation evolution chart.

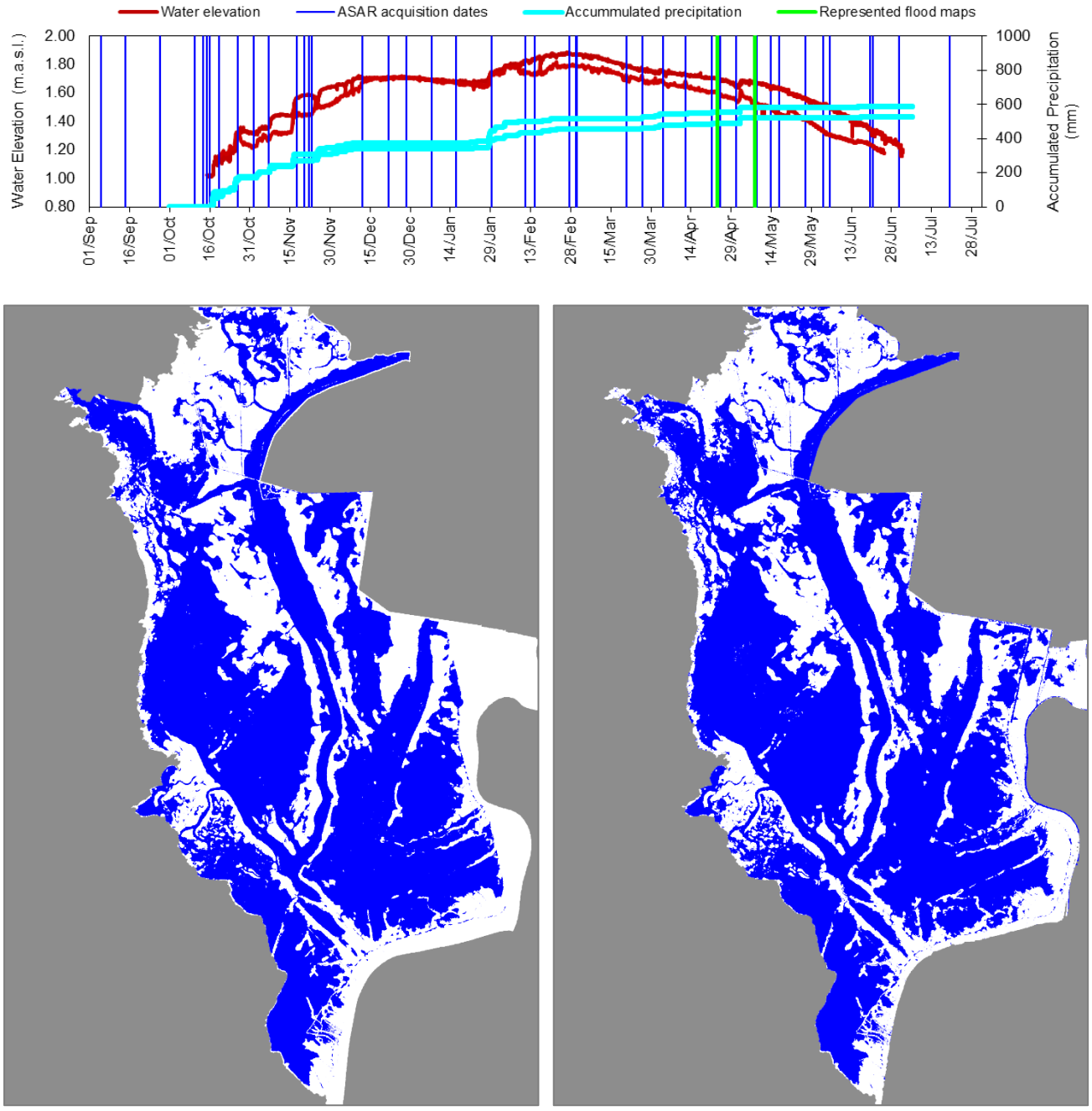

24 April 2007 8 May 2007

Fig. A1.9. Water elevation and accumulated precipitation evolution in the Doñana wetland during the 2006-2007 hydrologic year. Flood maps derived from Envisat/ASAR scenes for the two dates highlighted in green on the water elevation evolution chart.

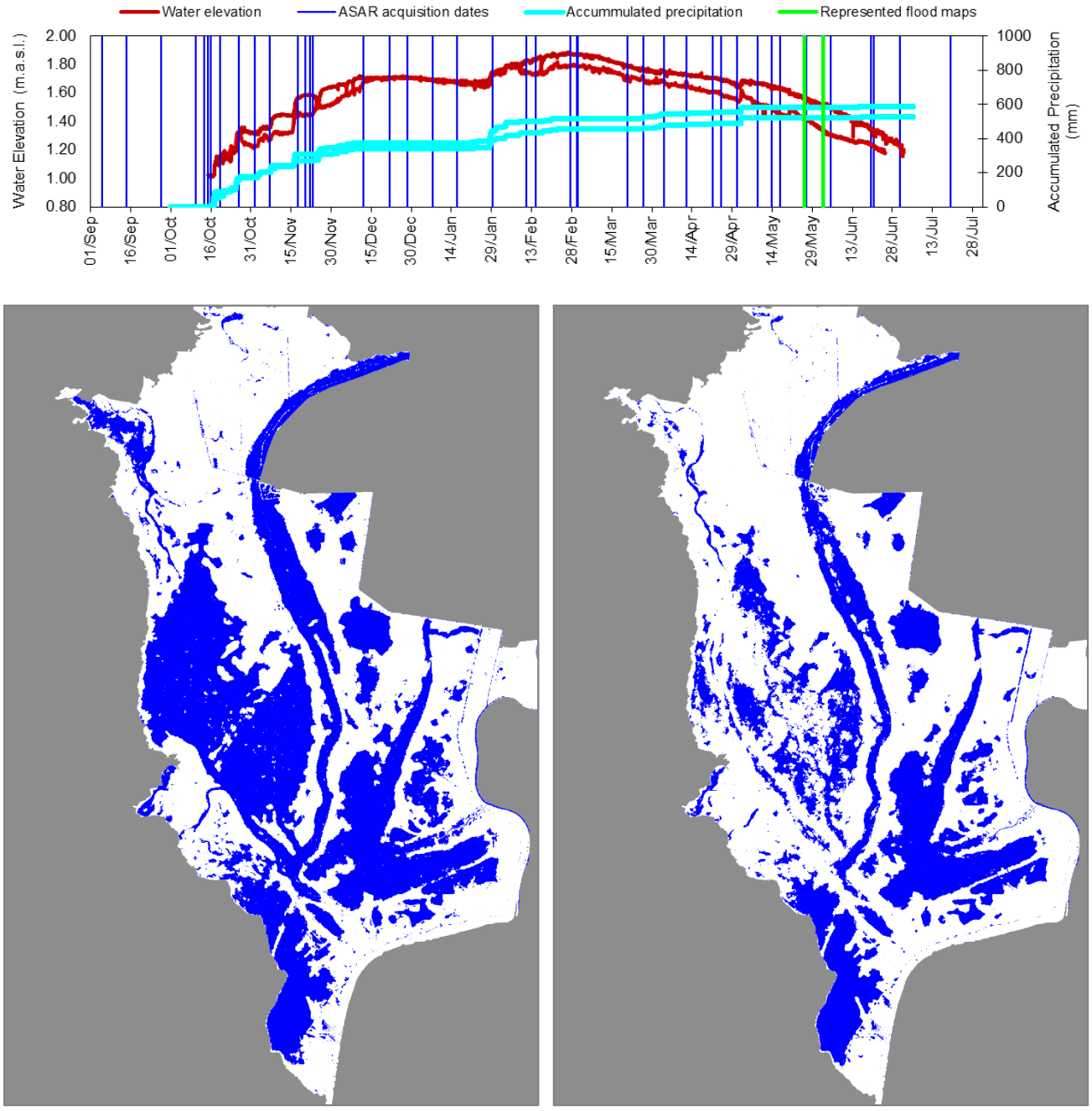

26 May 2007 2 June 2007

Fig. A1.10. Water elevation and accumulated precipitation evolution in the Doñana wetland during the 2006-2007 hydrologic year. Flood maps derived from Envisat/ASAR scenes for the two dates highlighted in green on the water elevation evolution chart.

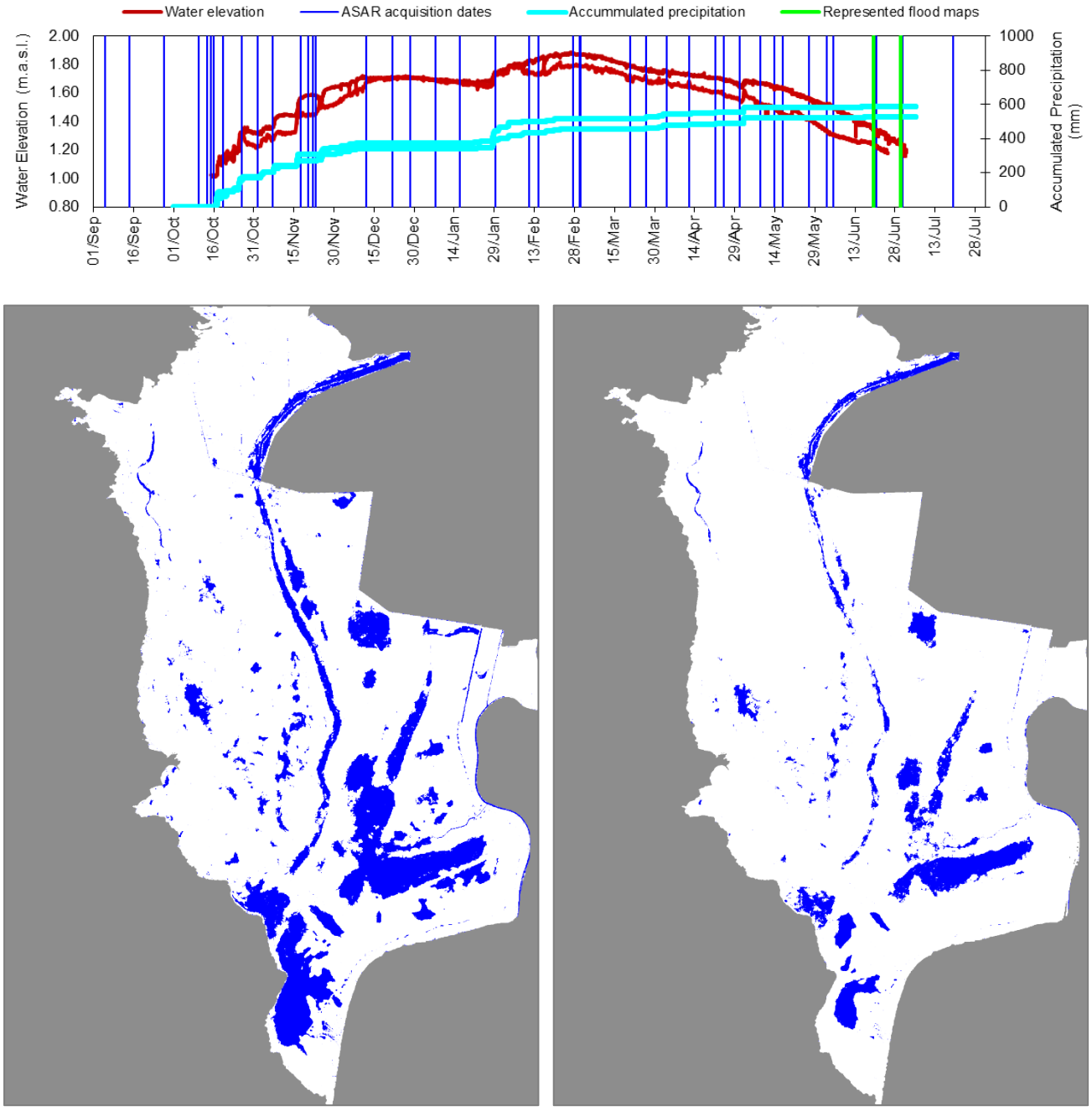

20 June 2007 30 June 2007

Fig. A1.11. Water elevation and accumulated precipitation evolution in the Doñana wetland during the 2006-2007 hydrologic year. Flood maps derived from Envisat/ASAR scenes for the two dates highlighted in green on the water elevation evolution chart.

Annex 2:
Inventory of Envisat/ASAR IM and AP Scenes of Doñana

Table A2.1. List of all ASAR/Envisat images acquired over Doñana wetland in Image and Alternated Polarization acquisition modes.

Acquisition Date	Acquisition Mode	Product	Start Time	Stop Time	Orbit	Track	Swath	Pass
19-Oct-2002	IM	ASA_IM__0P	22:12:33	22:12:49	3333	273	I2	A
04-Nov-2002	IM	ASA_IM__0P	22:09:43	22:09:59	3562	1	I1	A
08-Feb-2003	IM	ASA_IM__0P	10:37:55	10:38:11	4929	366	I2	D
08-May-2003	IM	ASA_IM__0P	10:40:47	10:41:03	6203	137	I2	D
02-Aug-2003	IM	ASA_IM__0P	10:38:07	10:38:23	7434	366	I2	D
30-Aug-2003	IM	ASA_IM__0P	22:12:44	22:13:00	7842	273	I2	A
11-Oct-2003	IM	ASA_IM__0P	10:38:06	10:38:22	8436	366	I2	D
08-Nov-2003	IM	ASA_IM__0P	22:12:37	22:12:53	8844	273	I2	A
13-Dec-2003	IM	ASA_IM__0P	22:12:38	22:12:54	9345	273	I2	A
30-Dec-2003	AP	ASA_APC_0P	10:23:53	10:24:09	9581	8	I7	D
08-Jan-2004	IM	ASA_IM__0P	10:40:55	10:41:11	9710	137	I2	D
17-Jan-2004	IM	ASA_IM__0P	22:12:37	22:12:53	9846	273	I2	A
24-Jan-2004	IM	ASA_IM__0P	10:38:02	10:38:18	9939	366	I2	D
06-Feb-2004	AP	ASA_APC_0P	10:29:30	10:29:46	10125	51	I4	D
25-Feb-2004	AP	ASA_APC_0P	10:32:20	10:32:36	10397	323	I4	D
28-Feb-2004	IM	ASA_IM__0P	10:38:02	10:38:18	10440	366	I2	D
27-Mar-2004	IM	ASA_IM__0P	22:12:39	22:12:55	10848	273	I2	A
01-May-2004	IM	ASA_IM__0P	22:12:36	22:12:52	11349	273	I2	A

Acquisition Date	Acquisition Mode	Product	Start Time	Stop Time	Orbit	Track	Swath	Pass
05-May-2004	AP	ASA_APC_0P	10:32:21	10:32:37	11399	323	I4	D
27-May-2004	IM	ASA_IM__0P	10:40:57	10:41:13	11714	137	I2	D
05-Jun-2004	IM	ASA_IM__0P	22:12:42	22:12:58	11850	273	I2	A
01-Jul-2004	IM	ASA_IM__0P	10:40:56	10:41:12	12215	137	I2	D
10-Jul-2004	IM	ASA_IM__0P	22:12:42	22:12:58	12351	273	I2	A
17-Jul-2004	IM	ASA_IM__0P	10:38:09	10:38:25	12444	366	I2	D
21-Aug-2004	IM	ASA_IM__0P	10:38:06	10:38:22	12945	366	I2	D
09-Sep-2004	IM	ASA_IM__0P	10:40:56	10:41:12	13217	137	I2	D
14-Oct-2004	IM	ASA_IM__0P	10:40:58	10:41:14	13718	137	I2	D
23-Oct-2004	IM	ASA_IM__0P	22:12:43	22:12:59	13854	273	I2	A
30-Oct-2004	IM	ASA_IM__0P	10:38:08	10:38:24	13947	366	I2	D
13-Dec-2004	IM	ASA_IM__0P	22:09:40	22:09:56	14584	1	I1	A
23-Dec-2004	IM	ASA_IM__0P	10:40:51	10:41:07	14720	137	I2	D
08-Jan-2005	IM	ASA_IM__0P	10:38:00	10:38:16	14949	366	I2	D
27-Jan-2005	IM	ASA_IM__0P	10:40:53	10:41:09	15221	137	I2	D
05-Feb-2005	IM	ASA_IM__0P	22:12:37	22:12:53	15357	273	I2	A
12-Feb-2005	IM	ASA_IM__0P	10:38:02	10:38:18	15450	366	I2	D
19-Mar-2005	IM	ASA_IM__0P	10:38:01	10:38:17	15951	366	I2	D
07-Apr-2005	IM	ASA_IM__0P	10:40:55	10:41:11	16223	137	I2	D
16-Apr-2005	IM	ASA_IM__0P	22:12:42	22:12:58	16359	273	I2	A
23-Apr-2005	IM	ASA_IM__0P	10:38:09	10:38:25	16452	366	I2	D
21-May-2005	IM	ASA_IM__0P	22:12:43	22:12:59	16860	273	I2	A
21-Jul-2005	IM	ASA_IM__0P	10:41:00	10:41:16	17726	137	I2	D
21-Jul-2005	IM	ASA_IM__0P	10:41:03	10:41:19	17726	137	I2	D
30-Jul-2005	IM	ASA_IM__0P	22:12:42	22:12:58	17862	273	I2	A
06-Aug-2005	IM	ASA_IM__0P	10:38:07	10:38:23	17955	366	I2	D
25-Aug-2005	IM	ASA_IM__0P	10:40:55	10:41:11	18227	137	I2	D
03-Sep-2005	IM	ASA_IM__0P	22:12:39	22:12:55	18363	273	I2	A
10-Sep-2005	IM	ASA_IM__0P	10:38:05	10:38:21	18456	366	I2	D

Acquisition Date	Acquisition Mode	Product	Start Time	Stop Time	Orbit	Track	Swath	Pass
03-Nov-2005	IM	ASA_IM__0P	10:40:58	10:41:14	19229	137	I2	D
12-Nov-2005	IM	ASA_IM__0P	22:12:41	22:12:57	19365	273	I2	A
19-Nov-2005	IM	ASA_IM__0P	10:38:05	10:38:21	19458	366	I2	D
29-Nov-2005	AP	ASA_APC_0P	10:23:49	10:24:05	19601	8	I7	D
28-Jan-2006	AP	ASA_APC_0P	10:37:55	10:38:11	20460	366	I2	D
10-Feb-2006	AP	ASA_APC_0P	10:29:24	10:29:40	20646	51	I4	D
16-Feb-2006	IM	ASA_IM__0P	10:40:46	10:41:02	20732	137	I2	D
23-Feb-2006	AP	ASA_APH_0P	10:20:52	10:21:08	20832	237	I7	D
25-Feb-2006	AP	ASA_APH_0P	22:12:30	22:12:46	20868	273	I1	A
26-Feb-2006	AP	ASA_APH_0P	10:26:33	10:26:49	20875	280	I5	D
28-Feb-2006	AP	ASA_APH_0P	22:18:11	22:18:27	20911	316	I4	A
01-Mar-2006	IM	ASA_IM__0P	10:32:14	10:32:30	20918	323	I4	D
04-Mar-2006	IM	ASA_IM__0P	10:37:55	10:38:11	20961	366	I2	D
13-Mar-2006	IM	ASA_IM__0P	22:09:38	22:09:54	21097	1	I1	A
14-Mar-2006	IM	ASA_IM__0P	10:23:41	10:23:57	21104	8	I6	D
17-Mar-2006	IM	ASA_IM__0P	10:29:22	10:29:38	21147	51	I4	D
20-Mar-2006	AP	ASA_APH_0P	10:35:03	10:35:19	21190	94	I3	D
23-Mar-2006	AP	ASA_APH_0P	10:40:43	10:40:59	21233	137	I1	D
01-Apr-2006	AP	ASA_APH_0P	22:12:26	22:12:42	21369	273	I2	A
02-Apr-2006	AP	ASA_APH_0P	10:26:30	10:26:46	21376	280	I5	D
04-Apr-2006	AP	ASA_APC_0P	22:18:09	22:18:25	21412	316	I4	A
05-Apr-2006	AP	ASA_APH_0P	10:32:12	10:32:28	21419	323	I4	D
10-Apr-2006	AP	ASA_APH_0P	22:29:33	22:29:49	21498	402	I7	A
17-Apr-2006	AP	ASA_APC_0P	22:09:41	22:09:57	21598	1	I1	A
18-Apr-2006	AP	ASA_APC_0P	10:23:44	10:24:00	21605	8	I6	D
20-Apr-2006	IM	ASA_IM__0P	22:15:22	22:15:38	21641	44	I3	A
21-Apr-2006	AP	ASA_APC_0P	10:29:26	10:29:42	21648	51	I4	D
23-Apr-2006	AP	ASA_APH_0P	22:21:04	22:21:20	21684	87	I4	A
24-Apr-2006	AP	ASA_APC_0P	10:35:08	10:35:24	21691	94	I3	D

Acquisition Date	Acquisition Mode	Product	Start Time	Stop Time	Orbit	Track	Swath	Pass
26-Apr-2006	AP	ASA_APH_0P	22:26:46	22:27:02	21727	130	I6	A
27-Apr-2006	AP	ASA_APH_0P	10:40:49	10:41:05	21734	137	I1	D
04-May-2006	IM	ASA_IM__0P	10:20:55	10:21:11	21834	237	I7	D
06-May-2006	AP	ASA_APH_0P	22:12:34	22:12:50	21870	273	I2	A
07-May-2006	IM	ASA_IM__0P	10:26:37	10:26:53	21877	280	I5	D
09-May-2006	AP	ASA_APC_0P	22:18:15	22:18:31	21913	316	I4	A
10-May-2006	AP	ASA_APH_0P	10:32:19	10:32:35	21920	323	I4	D
12-May-2006	AP	ASA_APC_0P	22:23:57	22:24:13	21956	359	I5	A
13-May-2006	IM	ASA_IM__0P	10:38:00	10:38:16	21963	366	I2	D
15-May-2006	IM	ASA_IM__0P	22:29:38	22:29:54	21999	402	I7	A
22-May-2006	IM	ASA_IM__0P	22:09:44	22:10:00	22099	1	I1	A
23-May-2006	IM	ASA_IM__0P	10:23:47	10:24:03	22106	8	I6	D
25-May-2006	IM	ASA_IM__0P	22:15:25	22:15:41	22142	44	I3	A
26-May-2006	IM	ASA_IM__0P	10:29:28	10:29:44	22149	51	I4	D
28-May-2006	AP	ASA_APH_0P	22:21:06	22:21:22	22185	87	I4	A
29-May-2006	AP	ASA_APH_0P	10:35:09	10:35:25	22192	94	I3	D
31-May-2006	AP	ASA_APH_0P	22:26:47	22:27:03	22228	130	I6	A
01-Jun-2006	AP	ASA_APH_0P	10:40:50	10:41:06	22235	137	I1	D
08-Jun-2006	AP	ASA_APH_0P	10:20:57	10:21:13	22335	237	I7	D
11-Jun-2006	AP	ASA_APH_0P	10:26:39	10:26:55	22378	280	I5	D
13-Jun-2006	AP	ASA_APH_0P	22:18:18	22:18:34	22414	316	I3	A
14-Jun-2006	AP	ASA_APH_0P	10:32:21	10:32:37	22421	323	I4	D
16-Jun-2006	AP	ASA_APH_0P	22:24:00	22:24:16	22457	359	I5	A
17-Jun-2006	AP	ASA_APH_0P	10:38:03	10:38:19	22464	366	I2	D
19-Jun-2006	AP	ASA_APH_0P	22:29:42	22:29:58	22500	402	I7	A
26-Jun-2006	AP	ASA_APH_0P	22:09:49	22:10:05	22600	1	I1	A
27-Jun-2006	AP	ASA_APH_0P	10:23:52	10:24:08	22607	8	I6	D
29-Jun-2006	AP	ASA_APH_0P	22:15:30	22:15:46	22643	44	I3	A
30-Jun-2006	AP	ASA_APH_0P	10:29:34	10:29:50	22650	51	I4	D

Acquisition Date	Acquisition Mode	Product	Start Time	Stop Time	Orbit	Track	Swath	Pass
02-Jul-2006	AP	ASA_APC_0P	22:21:12	22:21:28	22686	87	I4	A
03-Jul-2006	AP	ASA_APC_0P	10:35:15	10:35:31	22693	94	I3	D
05-Jul-2006	AP	ASA_APC_0P	22:26:53	22:27:09	22729	130	I6	A
06-Jul-2006	AP	ASA_APC_0P	10:40:56	10:41:12	22736	137	I1	D
15-Jul-2006	IM	ASA_IM__0P	22:12:41	22:12:57	22872	273	I2	A
31-Jul-2006	AP	ASA_APC_0P	22:09:50	22:10:06	23101	1	I1	A
04-Sep-2006	IM	ASA_IM__0P	22:09:45	22:10:01	23602	1	I1	A
05-Sep-2006	AP	ASA_APC_0P	10:23:48	10:24:04	23609	8	I6	D
14-Sep-2006	AP	ASA_APH_0P	10:40:51	10:41:07	23738	137	I1	D
23-Sep-2006	IM	ASA_IM__0P	22:12:36	22:12:52	23874	273	I2	A
27-Sep-2006	AP	ASA_APC_0P	10:32:21	10:32:37	23924	323	I4	D
02-Oct-2006	AP	ASA_APC_0P	22:29:42	22:29:58	24003	402	I7	A
09-Oct-2006	IM	ASA_IM__0P	22:09:48	22:10:04	24103	1	I1	A
10-Oct-2006	AP	ASA_APC_0P	10:23:51	10:24:07	24110	8	I6	D
12-Oct-2006	IM	ASA_IM__0P	22:15:29	22:15:45	24146	44	I3	A
13-Oct-2006	AP	ASA_APC_0P	10:29:33	10:29:49	24153	51	I4	D
15-Oct-2006	AP	ASA_APC_0P	22:21:11	22:21:27	24189	87	I4	A
16-Oct-2006	AP	ASA_APH_0P	10:35:14	10:35:30	24196	94	I3	D
19-Oct-2006	AP	ASA_APH_0P	10:40:55	10:41:11	24239	137	I1	D
26-Oct-2006	AP	ASA_APC_0P	10:21:01	10:21:17	24339	237	I7	D
28-Oct-2006	IM	ASA_IM__0P	22:12:39	22:12:55	24375	273	I2	A
29-Oct-2006	AP	ASA_APC_0P	10:26:43	10:26:59	24382	280	I5	D
01-Nov-2006	AP	ASA_APC_0P	10:32:24	10:32:40	24425	323	I4	D
03-Nov-2006	AP	ASA_APC_0P	22:24:02	22:24:18	24461	359	I5	A
04-Nov-2006	AP	ASA_APH_0P	10:38:05	10:38:21	24468	366	I2	D
06-Nov-2006	AP	ASA_APC_0P	22:29:43	22:29:59	24504	402	I7	A
16-Nov-2006	IM	ASA_IM__0P	22:15:29	22:15:45	24647	44	I3	A
17-Nov-2006	AP	ASA_APC_0P	10:29:32	10:29:48	24654	51	I4	D
20-Nov-2006	AP	ASA_APH_0P	10:35:14	10:35:30	24697	94	I3	D

Acquisition Date	Acquisition Mode	Product	Start Time	Stop Time	Orbit	Track	Swath	Pass
22-Nov-2006	AP	ASA_APC_0P	22:26:52	22:27:08	24733	130	I6	A
23-Nov-2006	AP	ASA_APH_0P	10:40:55	10:41:11	24740	137	I1	D
02-Dec-2006	IM	ASA_IM__0P	22:12:39	22:12:55	24876	273	I2	A
03-Dec-2006	AP	ASA_APC_0P	10:26:42	10:26:58	24883	280	I5	D
05-Dec-2006	AP	ASA_APH_0P	22:18:13	22:18:29	24919	316	I4	A
09-Dec-2006	AP	ASA_APH_0P	10:38:06	10:38:22	24969	366	I1	D
11-Dec-2006	AP	ASA_APC_0P	22:29:42	22:29:58	25005	402	I7	A
21-Dec-2006	AP	ASA_APC_0P	22:15:27	22:15:43	25148	44	I3	A
28-Dec-2006	AP	ASA_APH_0P	10:40:52	10:41:08	25241	137	I1	D
06-Jan-2007	AP	ASA_APC_0P	22:12:34	22:12:50	25377	273	I2	A
09-Jan-2007	AP	ASA_APV_0P	22:18:08	22:18:24	25420	316	I4	A
15-Jan-2007	AP	ASA_APC_0P	22:29:36	22:29:52	25506	402	I7	A
29-Jan-2007	AP	ASA_APC_0P	10:35:06	10:35:22	25699	94	I3	D
10-Feb-2007	AP	ASA_APC_0P	22:12:32	22:12:48	25878	273	I2	A
14-Feb-2007	AP	ASA_APC_0P	10:32:17	10:32:33	25928	323	I4	D
27-Feb-2007	AP	ASA_APC_0P	10:23:46	10:24:02	26114	8	I6	D
01-Mar-2007	AP	ASA_APC_0P	22:15:24	22:15:40	26150	44	I3	A
02-Mar-2007	AP	ASA_APC_0P	10:29:27	10:29:43	26157	51	I4	D
20-Mar-2007	AP	ASA_APC_0P	22:18:13	22:18:29	26422	316	I3	A
26-Mar-2007	AP	ASA_APC_0P	22:29:35	22:29:51	26508	402	I7	A
03-Apr-2007	AP	ASA_APC_0P	10:23:42	10:23:58	26615	8	I6	D
05-Apr-2007	AP	ASA_APC_0P	22:15:20	22:15:36	26651	44	I3	A
06-Apr-2007	AP	ASA_APC_0P	10:29:24	10:29:40	26658	51	I4	D
11-Apr-2007	AP	ASA_APC_0P	22:26:44	22:27:00	26737	130	I6	A
12-Apr-2007	IM	ASA_IM__0P	10:40:47	10:41:03	26744	137	I2	D
19-Apr-2007	AP	ASA_APC_0P	10:20:54	10:21:10	26844	237	I7	D
21-Apr-2007	AP	ASA_APC_0P	22:12:33	22:12:49	26880	273	I2	A
24-Apr-2007	AP	ASA_APC_0P	22:18:14	22:18:30	26923	316	I3	A
28-Apr-2007	IM	ASA_IM__0P	10:37:59	10:38:15	26973	366	I2	D

Acquisition Date	Acquisition Mode	Product	Start Time	Stop Time	Orbit	Track	Swath	Pass
30-Apr-2007	AP	ASA_APC_0P	22:29:38	22:29:54	27009	402	I7	A
08-May-2007	AP	ASA_APC_0P	10:23:46	10:24:02	27116	8	I6	D
10-May-2007	AP	ASA_APC_0P	22:15:24	22:15:40	27152	44	I3	A
13-May-2007	AP	ASA_APC_0P	22:21:06	22:21:22	27195	87	I4	A
16-May-2007	AP	ASA_APC_0P	22:26:47	22:27:03	27238	130	I6	A
17-May-2007	IM	ASA_IM__0P	10:40:50	10:41:06	27245	137	I2	D
24-May-2007	AP	ASA_APC_0P	10:20:57	10:21:13	27345	237	I7	D
26-May-2007	AP	ASA_APC_0P	22:12:35	22:12:51	27381	273	I2	A
02-Jun-2007	AP	ASA_APC_0P	10:38:01	10:38:17	27474	366	I2	D
04-Jun-2007	AP	ASA_APC_0P	22:29:40	22:29:56	27510	402	I7	A
14-Jun-2007	AP	ASA_APC_0P	22:15:26	22:15:42	27653	44	I3	A
20-Jun-2007	AP	ASA_APC_0P	22:26:49	22:27:05	27739	130	I6	A
21-Jun-2007	AP	ASA_APC_0P	10:40:52	10:41:08	27746	137	I1	D
30-Jun-2007	AP	ASA_APC_0P	22:12:36	22:12:52	27882	273	I2	A
19-Jul-2007	AP	ASA_APC_0P	22:15:27	22:15:43	28154	44	I3	A
26-Jul-2007	IM	ASA_IM__0P	10:40:52	10:41:08	28247	137	I2	D
03-Oct-2007	AP	ASA_APC_0P	22:26:45	22:27:01	29242	130	I6	A
04-Oct-2007	AP	ASA_APH_0P	10:40:48	10:41:04	29249	137	I1	D
20-Oct-2007	IM	ASA_IM__0P	10:38:04	10:38:20	29478	366	I2	D
07-Nov-2007	AP	ASA_APC_0P	22:26:44	22:27:00	29743	130	I6	A
08-Nov-2007	IM	ASA_IM__0P	10:40:56	10:41:12	29750	137	I1	D
26-Nov-2007	AP	ASA_APC_0P	22:29:32	22:29:48	30015	402	I7	A
12-Dec-2007	AP	ASA_APC_0P	22:26:42	22:26:58	30244	130	I6	A
29-Dec-2007	AP	ASA_APC_0P	10:37:55	10:38:11	30480	366	I2	D
07-Jan-2008	AP	ASA_APC_0P	22:09:39	22:09:55	30616	1	I1	A
10-Jan-2008	IM	ASA_IM__0P	22:15:12	22:15:28	30659	44	I3	A
16-Jan-2008	AP	ASA_APC_0P	22:26:43	22:26:59	30745	130	I6	A
26-Jan-2008	AP	ASA_APC_0P	22:12:29	22:12:45	30888	273	I2	A
02-Feb-2008	AP	ASA_APC_0P	10:37:55	10:38:11	30981	366	I2	D

Acquisition Date	Acquisition Mode	Product	Start Time	Stop Time	Orbit	Track	Swath	Pass
20-Feb-2008	AP	ASA_APC_0P	22:26:42	22:26:58	31246	130	I6	A
21-Feb-2008	AP	ASA_APC_0P	10:40:45	10:41:01	31253	137	I1	D
01-Mar-2008	AP	ASA_APC_0P	22:12:30	22:12:46	31389	273	I2	A
08-Mar-2008	AP	ASA_APC_0P	10:37:56	10:38:12	31482	366	I2	D
20-Mar-2008	AP	ASA_APC_0P	22:15:21	22:15:37	31661	44	I3	A
26-Mar-2008	AP	ASA_APC_0P	22:26:43	22:26:59	31747	130	I6	A
27-Mar-2008	AP	ASA_APC_0P	10:40:46	10:41:02	31754	137	I1	D
05-Apr-2008	AP	ASA_APC_0P	22:12:29	22:12:45	31890	273	I2	A
12-Apr-2008	AP	ASA_APC_0P	10:37:54	10:38:10	31983	366	I2	D
24-Apr-2008	AP	ASA_APC_0P	22:15:18	22:15:34	32162	44	I3	A
30-Apr-2008	AP	ASA_APC_0P	22:26:41	22:26:57	32248	130	I6	A
01-May-2008	AP	ASA_APC_0P	10:40:44	10:41:00	32255	137	I1	D
01-Jan-2009	IM	ASA_IM__0P	10:40:43	10:40:59	35762	137	I2	D
17-Jan-2009	IM	ASA_IM__0P	10:37:47	10:38:03	35991	366	I2	D
02-May-2009	IM	ASA_IM__0P	10:37:49	10:38:05	37494	366	I2	D
21-May-2009	IM	ASA_IM__0P	10:40:43	10:40:59	37766	137	I2	D
06-Jun-2009	IM	ASA_IM__0P	10:37:51	10:38:07	37995	366	I2	D
19-Sep-2009	IM	ASA_IM__0P	10:37:46	10:38:02	39498	366	I2	D
12-Nov-2009	IM	ASA_IM__0P	10:40:39	10:40:55	40271	137	I2	D
28-Nov-2009	IM	ASA_IM__0P	10:37:43	10:37:59	40500	366	I2	D
17-Dec-2009	IM	ASA_IM__0P	10:40:37	10:40:53	40772	137	I2	D
02-Jan-2010	IM	ASA_IM__0P	10:37:44	10:38:00	41001	366	I2	D
25-Feb-2010	IM	ASA_IM__0P	10:40:36	10:40:52	41774	137	I2	D
06-Mar-2010	AP	ASA_APC_0P	22:12:16	22:12:32	41910	273	I2	A
23-Mar-2010	AP	ASA_APC_0P	10:23:34	10:23:50	42146	8	I6	D
25-Mar-2010	AP	ASA_APC_0P	22:15:12	22:15:28	42182	44	I3	A
01-Apr-2010	AP	ASA_APC_0P	10:40:37	10:40:53	42275	137	I1	D
10-Apr-2010	AP	ASA_APC_0P	22:12:20	22:12:36	42411	273	I2	A
11-Apr-2010	AP	ASA_APC_0P	10:26:24	10:26:40	42418	280	I5	D

Acquisition Date	Acquisition Mode	Product	Start Time	Stop Time	Orbit	Track	Swath	Pass
27-Apr-2010	AP	ASA_APC_0P	10:23:31	10:23:47	42647	8	I6	D
15-May-2010	AP	ASA_APC_0P	22:12:19	22:12:35	42912	273	I2	A
16-May-2010	AP	ASA_APC_0P	10:26:23	10:26:39	42919	280	I5	D
21-May-2010	AP	ASA_APC_0P	22:23:42	22:23:58	42998	359	I5	A
22-May-2010	AP	ASA_APC_0P	10:37:45	10:38:01	43005	366	I2	D
06-Jun-2010	AP	ASA_APC_0P	22:20:51	22:21:07	43227	87	I4	A
07-Jun-2010	AP	ASA_APC_0P	10:34:55	10:35:11	43234	94	I3	D
23-Sep-2010	IM	ASA_IM__0P	10:40:34	10:40:50	44780	137	I2	D
09-Oct-2010	IM	ASA_IM__0P	10:37:37	10:37:53	45009	366	I2	D
19-Oct-2010	IM	ASA_IM__0P	10:23:31	10:23:47	45152	8	I6	D
04-May-2011	IM	ASA_IM__0P	10:29:55	10:30:11	47982	123	I6	D
01-Oct-2011	IM	ASA_IM__0P	10:31:59	10:32:15	50137	123	I6	D
31-Oct-2011	IM	ASA_IM__0P	10:32:14	10:32:30	50568	123	I6	D
30-Nov-2011	IM	ASA_IM__0P	10:32:26	10:32:42	50999	123	I6	D
30-Dec-2011	IM	ASA_IM__0P	10:32:34	10:32:50	51430	123	I6	D
29-Jan-2012	IM	ASA_IM__0P	10:32:39	10:32:55	51861	123	I6	D
28-Feb-2012	IM	ASA_IM__0P	10:32:41	10:32:57	52292	123	I6	D
29-Mar-2012	IM	ASA_IM__0P	10:32:48	10:33:04	52723	123	I6	D

Annex 3:
List of Publications and Conference Contributions

Publications in Scientific Journals

Martí-Cardona, B., Dolz-Ripollés, J., & López-Martínez, C., 2013. "Wetland inundation monitoring by the synergistic use of ENVISAT/ASAR imagery and ancilliary spatial data", *Remote Sensing of Environment*, 139(12), 171–184. doi:10.1016/j.rse.2013.07.028.

Martí-Cardona, B., López-Martínez, C., Dolz-Ripollés, J., & Bladé-Castellet, E., 2010. "ASAR polarimetric, multi-incidence angle and multitemporal characterization of Doñana wetlands for flood extent monitoring", *Remote Sensing of Environment*, 114(11), 2802–2815. doi:10.1016/j.rse.2010.06.015.

Ramos-Fuertes, A., Martí-Cardona, B., Bladé, E., & Dolz, J., 2013. "Envisat/ASAR images for the calibration of the wind drag action in Doñana wetlands 2D hydrodynamic model", *Remote Sensing*, 6(1), 379-406. doi:10.3390/rs6010379.

Currently in review:

Martí-Cardona, B., López-Martínez, C., & Dolz, J. "Local isotropy indicator for speckle filtering: Application to Doñana wetlands SAR images".

Conference Contributions

Martí-Cardona, B., & Dolz, J., 2013. “On the synergistic use of Envisat/ASAR imagery and ancillary spatial data for monitoring Doñana wetlands". In: *ESA Living Planet Symposium 2013: SP-722 proceedings*, 9-13 September 2013, Edinburgh. European Space Agency (ESA). ISBN 978-92-9221-286-5.

Martí-Cardona, B., Dolz, J. & López-Martínez, C., 2013. “Imágenes SAR para la cartografía de Doñana: beneficios del filtrado asistido por información espacial auxiliar*". I*n: *XV congreso de la Asociación Española de Teledetección: Sistemas operacionales de observación de la Tierra: actas,.* 22-24 Octubre, Torrejón de Ardoz. Instituto Nacinonal de Tecnología Aeroespacial (INTA). Copyright: M-29011-2013.

Martí-Cardona, B., López-Martínez, C. & Dolz, J., 2013. "Local texture stationarity indicator for filtering Doñana wetlands SAR images". In: *IGARSS 2012: International Geoscience and Remote Sensing Symposium: remote science for a dynamic Earth: proceedings,* 22-27 July 2012, Munich,. pp. 4903 - 4906. Institute of Electrical and Electronics Engineers (IEEE), 0007. ISBN 978-1-4673-1159-5.

Martí-Cardona, B., Ramos, A., Bladé, E., Duc Tran, T. & Dolz, J., 2011. "La teledetección como fuente de información para los modelos bidimensionales: aplicación al modelo Íber de las marismas de Doñana". In: *JIA: Jornadas de Ingeniería del Agua: modelos numéricos en dinámica fluvial*, Barcelona 5-6 Octubre 2011, pp. 1-8. Flumen (UPC). ISBN-13: 978-84-615-4023-5.

Martí-Cardona, B. López-Martínez, C. & Dolz, J., 2010. “ASAR multi-incidence angle, temporal backscattering signatures of Doñana marshes”, In: *URSI Commission F Microware Signtures 2010 and VI Italian National Workshop on Microwave Remote Sensing*, 4-8 October 2010, Florence. URSI Commission F Microware Signatures.

Martí-Cardona, B., Bladé, E., Duc Tran, T. & Dolz, J., 2010. “ASAR/Envisat images for the calibration of the wind hydrodynamic effect on Doñana wetland”, In: *Remote Sensing*

and Hydrology 2010 Symposium, 27-30 September 2010, Jackson Hole, WY,. pp. 459 - 463. IAHS publication 352. ISSN 0144-7815. ISBN: 978-1-907161-27-8.

Ramos, A., Martí-Cardona, B., Rabada, J., & Dolz, J., 2009. "Teledetección e información hidrometeorológica de campo en la marisma de Doñana", In: *I Jornadas de Ingenieria Hidráulica: Agua y Energía*, 2009, 27-28 Octubre 2009, Madrid, pp. 55-56. IAHR. ISBN: 978-90-78046-10-3.

Martí-Cardona, B., López-Martínez, C. & Dolz, J., 2009. "Efecto de la inundación sobre el coeficiente de retrodispersión de las marismas de Doñana en distintos swaths y polarizaciones de ASAR/Envisat", In: *XIII Congreso de la Asociación Española de Teledetección: Agua y Desarrollo Sostenible*, 23-26 Septiembre 2009, Calatayud. ISBN: 978-84-613-4257-0.

Martí-Cardona, B., López-Martínez, C., & Dolz, J., 2009. "Analysis of ASAR/Envisat polarimetric backscattering characteristics of Doñana National Park wetlands",In: 2009 *IEEE International Geoscience and Remote Sensing Symposium, IGARSS 2009,* 12-17 July, Cape Town, vol. 3, pp. 721-724. Institute of Electrical and Electronics Engineers (IEEE). ISBN: 978-1-4244-3395-7.

Martí-Cardona, B., Dolz, J., & Gili, J., 2006. "Monitoring of the flooding and dry-out processes in Doñana National Park for the calibration, refinement and operation of the hydrodynamic model of its marshes", In: *1st Glob Wetland Symposium: SP-634 proceedings*, 19-20 October 2006, Frascati, Italy. European Space Agency. ISBN 92-9092-945-6.

Annex 4:
Article

ASAR Polarimetric, Multi-Incidence Angle and Multitemporal Characterization of Doñana Wetlands for Flood Extent Monitoring

ATENCIÓ ¡

Les pàgines 257 a 270 de la tesi contenen el text de l'article que es pot consultar a la web de l'editor

ATENCIÓN ¡

Las páginas 257 a 270 de la tesis contienen el texto del articulo, que puede consultarse en la web del editor

ATTENTION ¡

Pages 257 to 270 of the thesis are availables at the editor's web

http://www.sciencedirect.com/science/article/pii/S0034425710002051

Annex 5:
Article

Wetland Inundation Monitoring
by the Synergistic Use of ENVISAT/ASAR Imagery
and Ancillary Spatial Data

ATENCIÓ ¡

Les pàgines 273 a 286 de la tesi contenen el text de l'article que es pot consultar a la web de l'editor

ATENCIÓN ¡

Las páginas 273 a 286 de la tesis contienen el texto del articulo, que puede consultarse en la web del editor

ATTENTION ¡

Pages 273 to 286 of the thesis are availables at the editor's web

http://www.sciencedirect.com/science/article/pii/S003442571300240X

Annex 6:
Article

Envisat/ASAR Images for the Calibration of the Wind Drag Action in the Doñana Wetlands 2D Hydrodynamic Model

Remote Sens. **2014**, *6*, 379-406; doi:10.3390/rs6010379

OPEN ACCESS

remote sensing

ISSN 2072-4292

www.mdpi.com/journal/remotesensing

Article

Envisat/ASAR Images for the Calibration of Wind Drag Action in the Doñana Wetlands 2D Hydrodynamic Model

Anaïs Ramos-Fuertes, Belen Marti-Cardona *, Ernest Bladé and Josep Dolz

Institut Flumen, Universitat Politècnica de Catalunya-BarcelonaTech and International Center for Numerical Methods in Engineering, Jordi Girona 1-3, E-08034 Barcelona, Spain;
E-Mails: anais.ramos@upc.edu (A.R.-F.); ernest.blade@upc.edu (E.B.); j.dolz@upc.edu (J.D.)

* Author to whom correspondence should be addressed; E-Mail: belen.marti@upc.edu;
Tel.: +34-934-016-881; Fax: +34-934-017-357.

Received: 28 October 2013; in revised form: 19 December 2013 / Accepted: 20 December 2013 / Published: 27 December 2013

Abstract: Doñana National Park wetlands are located in southwest Spain, on the right bank of the Guadalquivir River, near the Atlantic Ocean coast. The wetlands dry out completely every summer and progressively flood again throughout the fall and winter seasons. Given the flatness of Doñana's topography, the wind drag action can induce the flooding or emergence of extensive areas, detectable in remote sensing images. Envisat/ASAR scenes acquired before and during strong and persistent wind episodes enabled the spatial delineation of the wind-induced water displacement. A two-dimensional hydrodynamic model of Doñana wetlands was built in 2006 with the aim to predict the effect of proposed hydrologic restoration actions within Doñana's basin. In this work, on-site wind records and concurrent ASAR scenes are used for the calibration of the wind-drag modeling by assessing different formulations. Results show a good adjustment between the modeled and observed wind drag effect. Displacements of up to 2 km in the wind direction are satisfactorily reproduced by the hydrodynamic model, while including an atmospheric stability parameter led to no significant improvement of the results. Such evidence will contribute to a more accurate simulation of hypothetic or design scenarios, when no information is available for the atmospheric stability assessment.

Keywords: Doñana; wetlands; ASAR; flood mapping; hydrodynamic modeling; wind stress

---

1. Introduction

Doñana National Park (DNP) extents over 543 km^2 of the colmated Guadalquivir River paleo-estuary, in southwestern Spain. The area, considered the largest European habitat for migrating waterfowl, was declared a National Park in 1969, a Biosphere Reserve under the UNESCO Man and the Biosphere Programme in 1980, a Wetland of International Importance under the Ramsar Convention in 1982, a Special Protection Area under the European Union Directive on the Conservation of Wild Birds in 1988, and a UNESCO Natural World Heritage Site in 1994 [1]. About half of DNP's extension is marshland area, which experiences annual cycles of inundation and depletion. While flooded, Doñana marshes are a vast area of shallow lakes of variable size and degree of spatial connectivity, mainly depending on the regional pluvial regime and on the time of year. The natural hydrological cycle of the marshes, which constitutes the strategic basis for the entire ecosystem functioning, has been threatened by a number of past and present human actions [2–4]. The alteration of tributary water courses (channels, deforestation, pollution) and the intensive agricultural occupation of the marshes during the 20th century have deeply altered their hydrological scheme and reduced their extension from about 1,800 to 300 km^2 [5]. At present, the water exchange between the marshes and the Guadalquivir River is managed by DNP's authorities through a number of sluices located in an artificial 12 km long levee.

In order to restore the natural hydrological behavior of the marshes, Spanish authorities promoted in 1998 the project called Doñana 2005 [6]. The Institut Flumen, at the Universitat Politècnica de Catalunya and the International Center for Numerical Methods in Engineering, developed within the framework of this project a numerical model of DNP marshes in order to predict the hydrodynamic response of the wetland to the proposed restoration actions [7]. The rigorous calibration of the hydrodynamic model was assisted by field data from a network of *in situ* hydrometeorological gauging stations and by synoptic observations of the marshes through remote sensing images. Thus, Doñana images of the Advanced Synthetic Aperture Radar (ASAR) sensor on board on the Envisat satellite of the European Space Agency (ESA) [8], acquired since 2006 at different incidence angles and polarization configurations, enabled the calibration of different capabilities of the model, as well as the monitoring of the marshes' flood extent evolution and the seasonal development of helophyte vegetation [9].

Given the flatness of Doñana's topography, sustained winds can significantly modify the hydrodynamics and water extent of the marshes. Wind stress, as the vertical transfer of horizontal momentum between the atmosphere and surface, is considered a major driving force for shallow water circulation and mixing [10,11]. When sustained over a long period of time, it produces a setup of the water surface in the downwind direction. Various studies on shallow water bodies have documented the relationship between water level and local wind intensity, with short time lags of a few hours between wind speed changes and water level changes [12–14]. In the presence of low terrain slopes, as occurs in most wetlands and estuarine areas, this wind setup can eventually modify the inundation patterns [15]. If stratification occurs, persistent winds have also been identified as the cause of massive fish kills by upwellings of hypolimnetic water [16].

Current hydrodynamic modeling of wetlands and shallow reservoirs is normally taken into account using 2D depth averaged models based on either wastewater treatment or overseas experience [17–19].

Wind stress modeling over the wetland surface ranges from simple formulations using a constant wind drag coefficient [17] to more theoretically sounded complex formulations [20]. Despite wind being usually presumed as the major driver of water movement and studied phenomena such as seiche formation [17] or water turbidity [21], little discussion is found in the freshwater modeling literature about the choice of the wind stress formulation. However, wind drag modeling is still an ongoing discussion in coastal and marine engineering [22].

This paper describes the implementation of the wind stress action into the hydrodynamic model of Doñana marshes with the aid of Envisat/ASAR imagery. Two ASAR observation opportunities of an isolated water body are used to calibrate the observed wind-induced water displacement by choosing the most suitable wind stress formulation in the literature. The chosen formulation is also verified for another wind event observed in a different location of the marshes.

The paper is organized as follows. Second section describes the study area, Doñana marshes, and specifically the modeled ponds. Section 3 describes the study data, composed of radar imagery and field hydrometeorological data. Section 4 contains the methodology of flood mapping and hydrodynamic modeling. Section 5 presents and discusses the modeling results of the wind stress formulations tested at two observed events of wind-induced water displacement. Finally, Section 6 contains main conclusions and recommendations.

2. Study Area

Doñana marshes are composed of a variety of temporary shallow (<1.5 m depth) water bodies extended over an area of 298 km^2 on the right bank of the Guadalquivir River mouth (Figure 1). They are located at the former estuary of the river, which was filled by fine fluvial clayey sediment resulting in an extremely flat topography, with a maximum elevation difference of 2.50 m in its entire area. The main water inputs in the marshes come from direct precipitation and small and irregular northwestern tributaries, since they are disconnected from the Guadalquivir River and its tributaries by artificial structures. The climate is sub-humid Mediterranean with Atlantic influence [23], with mild winters (average temperature of 10 °C in January) and hot dry summers (24 °C in August). Mean annual precipitation is 537 mm [24], and average flooding periods occur from early autumn to late summer, when the marshes completely dry up [25,26]. On average, about 50% of the mean annual precipitation corresponds to the period from November to January, while less than 5% to the period from June to September [24]. However, the intra and inter-annual variability of the precipitation are high, resulting in flooding periods of variable magnitude and duration. Inside the marshes, small altitudinal gradients play an important role in defining the topographical elements (Figure 1), the water spatial and temporal distribution and the predominant vegetation communities.

In this work, two of the greater ponds (locally named "lucios") of the marshes are selected for the calibration and verification of the wind stress effect on the water extent, both at the southern part of the marshes (Figure 1). First, a wind-induced water displacement event observed at Membrillo pond is selected for calibration purposes (named "Membrillo event"). The pond's size is about 11.5 km^2 and has the main longitudinal axis oriented to the N-S direction. Using the chosen wind stress formula, one more event is simulated at the Ánsares pond (named "Ánsares event"), which has an area of about 7.5 km^2 and the main longitudinal axis at the WSW-ENE direction.

Figure 1. Location and digital terrain model of Doñana wetlands. The location of the modeled areas and gauging stations is indicated on the digital terrain model.

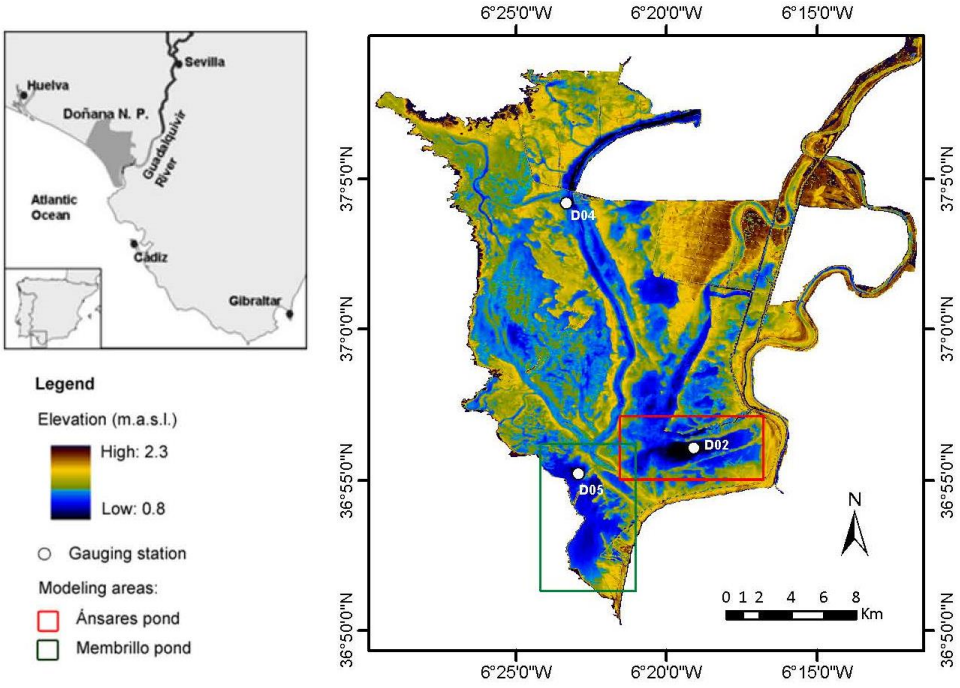

Most of the Membrillo and Ánsares ponds are formed by clayey bare soil, and virtually no vegetation develops in them at any time of the year [27]. Helophyte communities have colonized the pond's slightly higher terrain, located at the western and northern ends of Ánsares and Membrillo, respectively. These communities are dominated by *Scirpus maritimus* (Castañuela) and *Scirpus litorales* (Bayunco). The Castañuela is an herb of height ranging between 0.6 and 1.0 m. The Bayunco is reed-like, and often taller than 1.0 m. Both species start emerging from the water surface towards the end of February. They experience rapid growth throughout the spring season and then dry out during the summer. Their brown stems stick out of the water surface when the marshes flood in autumn, but they progressively decay and sink by the spring.

3. Study Data

3.1. Envisat/ASAR Imagery

Three images of the ASAR sensor were used in this study for mapping the inundation in the DNP marshes. The ASAR sensor was installed on board of the Envisat satellite of the ESA [8] and was operational since the launch of the satellite in 2002, until its failure in 2012. ASAR imaged the Earth's surface by emitting and receiving electromagnetic radiation at C-band (5.34 GHz) and could be operated in different measurement modes and at seven predetermined incidence angles or swaths, designated as IS1 to IS7. The appropriateness of the ASAR data for flood mapping and herbaceous wetlands monitoring has been widely reported. Some examples can be found in [28–34].

The images used in this study were acquired in Alternated Polarization and Image acquisition modes, and were received respectively in the form of Alternated Polarization Ellipsoid Geocoded (ASA_APG_1P) and Image Mode Precision (ASA_IMP_1P) products. Both products are multi-look, ground-range projected digital images, with a nominal resolution (range × azimuth) of 30 m × 30 m. In the Alternating Polarization mode, the ASAR sensor acquired data in two of the three polarization channels as follows: HH, VV and HV. In the HH and VV channels, also referred to as like-polar channels, the sensor antenna used respectively horizontally or vertically polarized radiation, and the same polarization was used for transmitting and receiving. HV is the cross-polar channel, where the transmitted and received pulses have different polarization. In the Image acquisition mode only one like-polar channel could be used, either HH or VV.

Table 1 summarizes the acquisition date, swath, incidence angle range, mode and polarization configuration for the images used in this study.

Table 1. Envisat/ASAR data.

Acquisition Date	ASAR Swath	Incidence Angle Range (°)	Acquisition Mode	Polarization Configuration
19 October 2006	IS1	15.0–22.9	Alternated polarization	HH/HV
1 March 2006	IS4	31.0–36.3	Image	HH
4 March 2006	IS2	19.2–26.7	Image	HH

3.2. In Situ *Hydrometeorological Measurements*

A network of six hydrometeorological gauging stations was progressively installed in Doñana marshes between September 2004 and September 2007. These stations were operational until October 2011 and acquired 10 min records of water level, water temperature, conductivity, dissolved oxygen, precipitation, wind direction and velocity, air temperature and humidity, soil temperature, incident and reflected solar radiation and net all-wave radiation [35]. The stations used in this study are shown in Figure 1. The following field data were available for each case of study:

- For the Membrillo event, measuring station D05 was still not operational. Wind speed and direction, air temperature and precipitation concurrent with the ASAR scenes were recorded at station D04. Water temperature was available at station D02.
- For the Ánsares event, wind speed, wind direction and precipitation concurrent with the ASAR scene were recorded at station D05. Water level was available at station D02.

Horizontal wind velocity and direction were measured at 2 m height by 0513-5 Young helicoid anemometers with precisions of 0.3 m/s in the wind velocity and 3° in the wind direction. Air temperature was measured with two Vaisala HMP45C sensors with 0.2 °C accuracy. Water level was measured with GE Druck PTX 1830 pressure sensors located 10 cm over the ground, with accuracy of 1.6 mm for water depths less than 1 m. Water temperature was measured by duplicated Campbell Scientific PT-100 probes (0.1 °C accuracy) at 0, 0.5 and 1 m above the ground. The surface water temperature, when needed, was obtained by selecting the highest underwater record of temperature with the aid of the water level measurements. All measurements were taken at 1 min time intervals (except for the anemometers, at 2 s time intervals) and recorded at 10 min averages by a Campbell Scientific's CR10 datalogger. Data were periodically downloaded by modem.

The wind drag effect was first observed in oscillations of the water level consistent with those of the wind speed and direction. Figure 2 shows hydrometeorological data from stations D02 and D04 (as named in Figure 1) from 20 February to 6 March 2006, coincident with the Membrillo event. The overall increasing tendency of water level responds to direct precipitation, since the marshes at that time were divided in several water bodies and the measurement points were disconnected from the northwestern tributaries. Short-term variations of the water level respond to the wind forcing, as they coincide with the wind velocity variations. Water level response to the sea breeze during calm days is of the order of 5 cm (e.g., 28 February–2 March in Figure 2), while wind events over 10 m/s can modify up to 10 cm the height of the water column (e.g., 26 February, 4 March in Figure 2). Further analyses of the temporal and spectral correlation of measured wind and water level at Doñana marshes are presented in [14].

Figure 2. Hydrometeorological records and ASAR acquisition dates from 20 February to 6 March 2006. Short-term wind induced variations of water depth are visible. Time series are recorded every 10 min and labeled according to measuring stations presented in Figure 1.

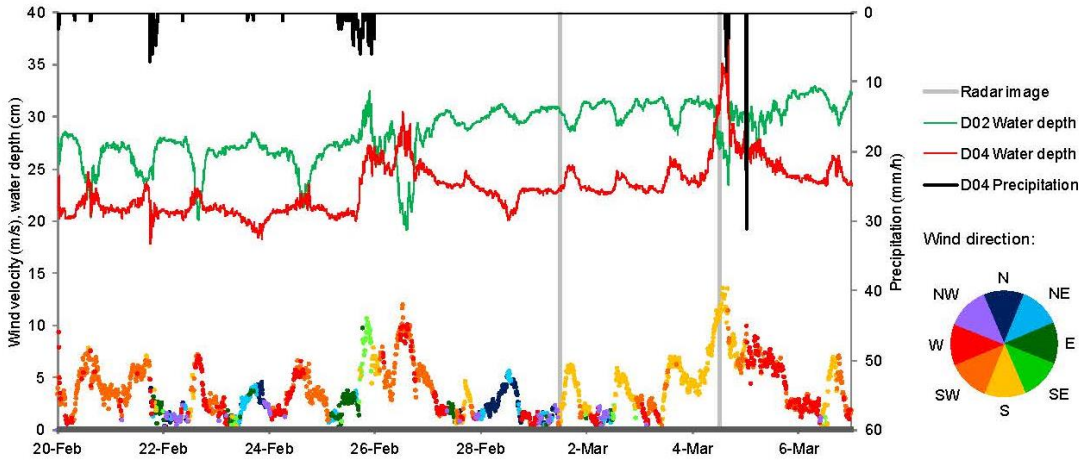

The water level response to wind stress depends on location and wind direction. In this work, the latter is not supposed to change significantly across the marshes due to the practical absence of topographical obstacles. Locations shown in Figure 2 respond in an opposite way to the same wind forcing, depending on their position in their respective water body. For the same location, opposite responses are also found for N-NE and S-SW wind events (e.g., 28 February and 1 March, respectively).

4. Methodology

4.1. Flood Mapping from the ASAR Images

The ASAR scenes in Table 1 were received from the ESA as radar brightness and calibrated to backscattering coefficient according to [36]. The images were then precisely co-registered to the existing DTM. Approximately 80 ground control points were selected to perform the co-registration. Due to the terrain flatness, the ASAR images approximated fairly the projected geometry of the DTM,

so a first degree polynomial and the nearest neighborhood methods were considered appropriate for the co-registration warping and resampling, respectively. The total root mean square error yielded values below 0.6 pixels for the co-registration of the three images.

4.1.1. ASAR Image Interpretation

Figure 3 shows the Membrillo pond on the calibrated ASAR images from 1 March and 4 March 2006. The Ánsares pond is depicted in the ASAR image from 19 October 2006 in Figure 4. The backscattering from these ponds was interpreted and related to their physical conditions at the time of the image acquisition, based on the concurrent wind records and the ASAR backscattering characterization of Doñana wetlands undertaken in [9]. This interpretation is explained as follows.

Figure 3. Membrillo pond on the calibrated ASAR images from (**a**) 1 March 2006, at swath IS4, HH polarization; (**b**) 4 March 2006, at swath IS2, HH polarization. Backscattering coefficient represented in dB. The study area is defined by the red line.

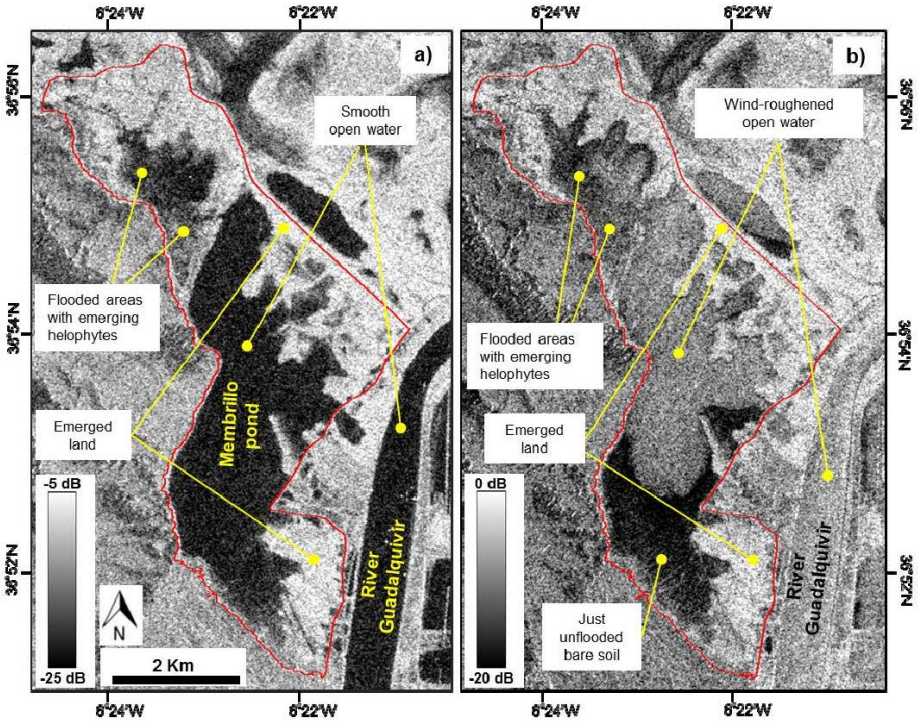

The ASAR image from 1 March 2006, in Figure 3a, was acquired under low wind conditions, as it can be appreciated in Figure 2. In this situation, open water surfaces are smooth and the radar beam is reflected specularly forward, away from the sensor. Hence, no return is received by the SAR antenna and the open water areas appear dark on the radar image. The brightest areas on the scene correspond to emerged land. Flooded surfaces with emerging sparse helophyte vegetation yield intermediate returns caused by the radar beam being partially reflected forward by the water surface and partially reflected back by direct and double bounce backscattering from the vertical stems [9].

Figure 4. Ánsares pond on the calibrated ASAR image from 19 October 2006, at swath IS1: (**a**) HV backscattering coefficient (dB); (**b**) HH backscattering coefficient (dB).

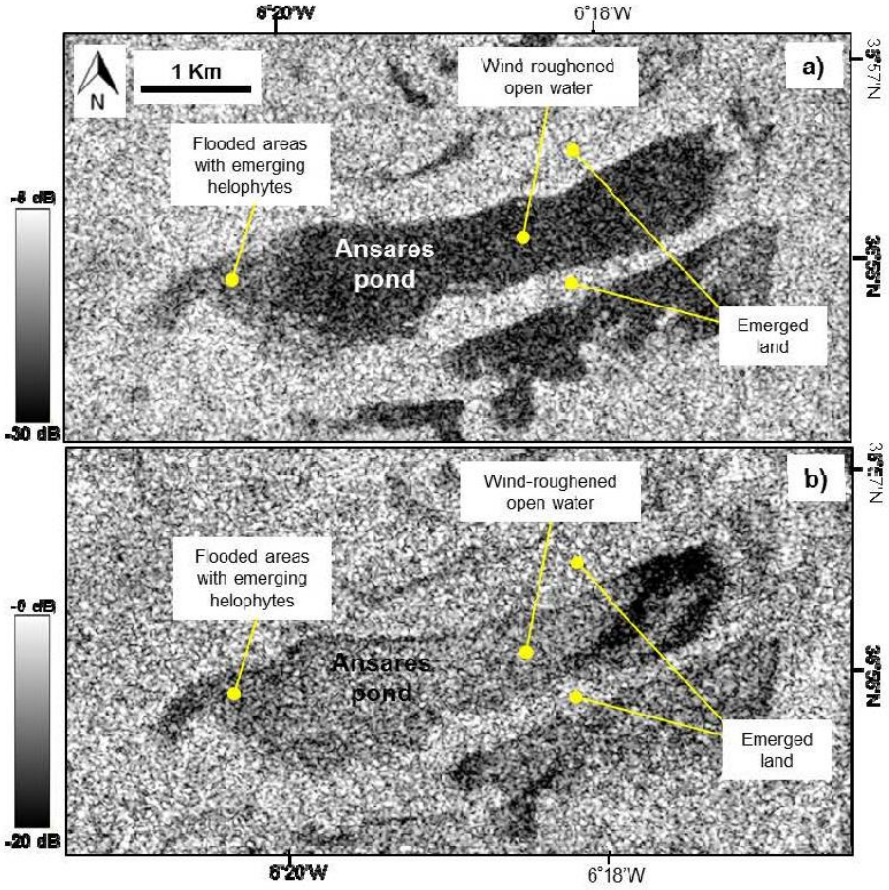

The March 4th image, in Figure 3b, was acquired after a sustained, strong-wind episode, as revealed by Figure 2. The wind-roughened water surface induces high backscattering on like-polarized SAR channels at low incidence angles [9], such as the IS2 swath of the March 4th HH-polarized image. As a consequence, open water areas in the Doñana ponds and the Guadalquivir River are bright on this scene, although not as much as the emerged land. A noticeable dark area appears on the upwind side (southern end) of several ponds. This phenomenon had been previously observed on a number of low incidence angle ASAR images acquired on windy days, and the nature of the dark area was verified by ground truth data. When the water mass is pushed by the wind, a portion of the pond's flooded area emerges at the upwind end. If the emerging surface consists of bare soil, this exhibits a smooth surface, formed by a puzzle of unconnected extremely shallow puddles, captured in Figure 5. The shallowness and reduced fetch of these paddles impede the formation of the waves responsible for the radar backscattering. Hence, bare soil areas emerging as a consequence of the wind drag action also cause forward specular reflection of the radar beam and appear dark on the ASAR images.

Figure 5. View of a bare soil area recently emerged due to the wind-induced water displacement.

The area of flooded helophytes at the pond's northern end in Figure 3b also shows lower backscattering than from the wind-roughened open water. As for the just unflooded bare soil, this phenomenon had already been observed on windy days. It was verified by field work that the flood surface among emerging vegetation remains smoother than in open water areas, and therefore appears darker than the latter on SAR images. This fact is attributable to the wind energy attenuation effect of the vegetation.

Figure 4a,b depicts the Ánsares pond in HV and HH polarization respectively, on the ASAR image from 19 October 2006. This scene was acquired after an episode of sustained southwest winds. The wind-roughened open water surface in Doñana ponds induces little depolarization of the radar signal, so backscatter from open water areas is low in the cross-polar channel and subsequently appears dark on Figure 4a. The HV return is most powerful on the emerged areas, were the volume scattering from the vegetation bushes causes depolarization in the radar signal. As for the March 1st image in Figure 3a, the HV power backscattered by flooded helophytes takes intermediate values, due to the combined volume backscattering from the vegetation and the specular reflection on the water surface.

In the HH channel, the emerged pastureland is again the cover type showing the largest backscattering. As already mentioned, the water surface roughness does induce significant radar returns in like-polar channels, and subsequently this target appears bright in Figure 4b. Although the open water shows slightly lower backscattering than the emerged land, both cover types are more easily separable in the HV channel, as can be observed by the simple visual contrast between them in Figure 4a.

Dark elongated features appear on the eastern end of the Ánsares pond, in Figure 4b. They are believed to correspond to patches of smoother water surface. This sort of dark patch with capricious geometries is often observed on wind-roughened water surfaces at low incidence angle SAR images. Some authors have related these patches to wind-induced upwellings in thermally stratified coastal water bodies [37]. However, the physical explanation to these features has not yet been studied in Doñana.

4.1.2. Image Filtering

Prior to the delineation of the ponds' flooded area, the ASAR images were filtered out to smooth backscattering fluctuations owing to the speckle noise. The applied filtering method takes advantage of the tight relationship found between Doñana's cover types and the terrain topography [26,27,38,39]. As a consequence of this relation, neighboring pixels at the same elevation are most likely to be of the same class and therefore constitute a stationary neighborhood. This peculiarity of Doñana's landscape was utilized as follows:

Figure 6. Membrillo pond on the filtered ASAR images from (**a**) 1 March 2006, at swath IS4, HH polarization; (**b**) 4 March 2006, at swath IS2, HH polarization. Backscattering coefficient represented in dB. The study area is defined by the red line.

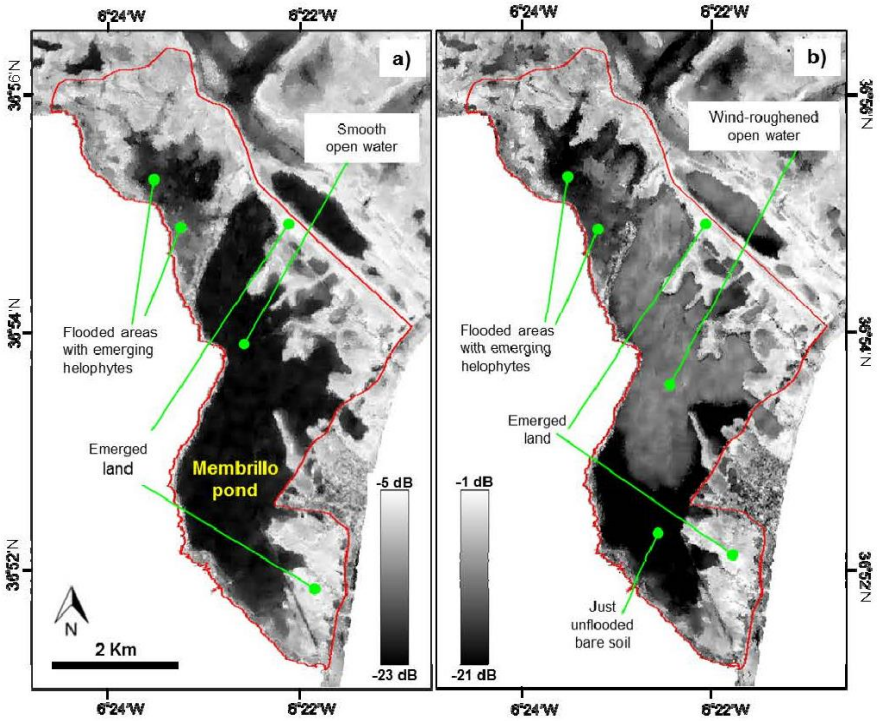

At every image location P, the algorithm selects those connected pixels which are ±25 mm apart from the pixel to be filtered, P. This set of pixels forms the P's irregular filtering neighborhood. The coefficient of variation (CV) is then used to assess the neighborhood stationarity. If compliant with the CV expected from the corresponding ASAR product ENL, pixel P's filtered value is computed as the filtering region mean. Otherwise, the neighborhood is iteratively split in a direction orthogonal to the region's main gradient, until the sub-part containing P meets the stationarity requirements. Further details on the filtering procedure and performance examples can be found in [38]. Figure 6 shows the filtering result for the scenes from 1 and 4 March 2006.

It is worth mentioning that the topography-based neighborhood sampling method is irrelevant for those pixels located in the middle of an open water patch. However, the flooded area perimeter still

approximates the terrain contours, so topography-based neighborhoods are more likely to adjust to them than square filtering windows. As a result, the flood boundaries in DTM-filtered images are notably sharper than those obtained with fixed filtering window geometries. This comparison is discussed and sample images included in [38,40,41].

4.1.3. Flood Mapping

Regions representative of the target's main land cover classes (ROIs) were selected on the three ASAR scenes. The selection was undertaken in the backscattering coefficient-terrain elevation space. The elevation data was introduced in order to increase the class separability. Figure 7 illustrates the ROIs selection for the March 4th image: points in Figure 7a's plot depict the image pixels by their filtered backscattering coefficient and their terrain elevation. Points in the plot with the highest elevation and backscattering values correspond almost certainly to emerged land pixels. Ring A in Figure 7a indicates the selection of the emerged land ROIs. Ring B encircles a large set of pixels with intermediate elevation and radar returns which correspond to wind-roughened water areas. Most of the low backscattering points, in Ring C, correspond to just unflooded pixels at the southern end of the Membrillo pond. Pixel clusters A, B and C are depicted on the corresponding ASAR image in Figure 7b.

Figure 7. Initial regions of interest (ROI's) for the image from 4 March 2006: (**a**) selection of the ROIs in the backscattering coefficient-terrain elevation space; (**b**) view of the selected ROIs on the ASAR image.

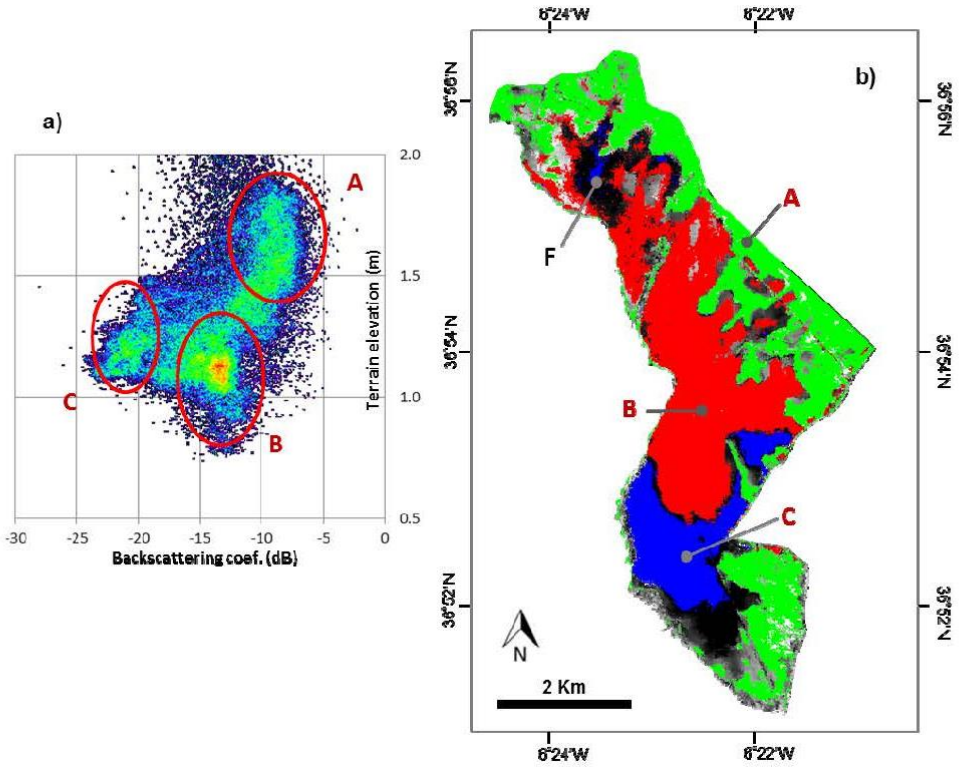

An iterative region growing procedure was then applied to extend the ROIs on the filtered image space. Firstly, the image pixels adjacent to the classes initial ROIs were selected. Next, the Mahalanobis distance [42] between every adjacent pixel and each class is computed. The elevation data was not used in the distance computation since it would somehow push the perimeter of the classes to be horizontal, and detection of the flood perimeter deviation from the horizontal plane was key for the wind drag action calibration. If the minimum Mahalanobis distance between an adjacent pixel and a sample class happens for the contiguous class, then the pixel is assigned to that class. When all assignments have been performed, the just classified pixels are adjoined to the sample regions. New adjacent pixels are determined and the whole process is repeated. The process ends when no new assignments are made in two consecutive iterations. Further details of the region growing procedure and sample results are included in [38].

Some flooded helophyte pixels were selected as just unflooded bare soil (region F in Figure 7b) at the ROIs selection stage. The reason is that backscattering and elevation values in flooded helophyte and recently unflooded bare soil areas overlap considerably in the backscattering-elevation space, and it was not possible to select two separate ROIs for them. As a consequence, the darkest flooded helophyte areas were classified as unflooded bare soil (blue class in Figure 7b), after the region growing procedure. Ancillary spatial data on Doñana marshes land cover types had to be applied to disentangle this confusion. The existing vegetation maps [43,44] indicate the presence of helophytes around region F. Such presence was corroborated by several ground truth campaigns. The unflooded bare soil class (blue in Figure 7b) resulting from the region growing procedure was intersected with the vegetation map. Those blue class areas at the north of the Membrillo pond coinciding with helophyte areas according to the vegetation map were reclassified as flooded helophytes.

It has to be said that the water/land discrimination accuracy would be greatly enhanced by the use of optical data. However, the wind-induced water displacement can change rapidly and capriciously with the wind speed and direction, so images taken only hours apart can show flooded areas shifts of hundreds of meters. Hence, an optical image appropriate to assist the water displacement delineation should have been acquired simultaneously to the ASAR observation, and such data were not available.

The above-described classification procedure was also applied to the ASAR images from 1 March 2006 and 19 October 2006 in order to determine the flood perimeter in the Membrillo and Ánsares ponds, respectively. For the October image, only the HV channel was used, since this polarization provides better discrimination than HH between wind-roughened open water and emerged land, as can be observed in Figure 4a. The March 1st scene was acquired under low wind conditions. As a consequence, the vast open water surface in the Membrillo pond was smooth and appears dark on the ASAR image. All this dark area was mapped as flooded by the classification algorithm. However, if waterlogged soil areas, as those depicted in Figure 5, were adjacent to the Membrillo open water, they would have not been discriminated from the open water and would be included as flooded in the resulting map.

Unfortunately, no ground truth data were collected coinciding with the ASAR acquisitions presented in this manuscript, so the flood mapping accuracy could not be assessed. However, the same flood mapping procedure was applied to other similar ASAR scenes of Doñana for which ground truth data were available. As reported in [38], the classification accuracy for those images was around 92%. This value provides an estimate of this study's flood mapping accuracy.

The flood perimeters for the Membrillo and Ánsares main water bodies obtained by the above presented methodology are shown in conjunction with the hydrodynamic modeling results in Section 5.

4.2. Hydrodynamic Modeling

Within the frame of the Doñana 2005 restoration project, a two-dimension hydrodynamic model of Doñana marshes was developed [7,45]. Given the boundary conditions (topography, inflow hydrographs, precipitation, wind speed and direction, situation of the sluices communicating the marshes with the Guadalquivir river and water levels in the river) and the loss functions (mainly evapotranspiration), the hydrodynamic model simulates the water level and velocity evolution in the marshes. This model was built on the basis of the Iber software [46], which is a numerical tool for the simulation of unsteady open-channel turbulent flow and sediment transport in two dimensions. The water movement is computed by solving the 2D Shallow Water Equations or Saint Venant equations.

4.2.1. Numerical Scheme

The equations solved by the hydrodynamic model are the 2D Saint Venant equations (or two-dimensional shallow water equations), which can be written in conservative form as:

$$\frac{\partial}{\partial t}\mathbf{U} + \nabla\mathbf{F} = \mathbf{H} \tag{1}$$

where U_{2D} is the conserved variables vector, F_{2D} is the flux tensor and H_{2D} is the source term. In this work the wind stresses have been included as part of the source term:

$$\mathbf{U} = \begin{pmatrix} h \\ hu \\ hv \end{pmatrix} \quad ; \quad \mathbf{F} = \begin{pmatrix} hu & hv \\ hu^2 + \frac{gh^2}{2} & huv \\ huv & uv^2 + \frac{gh^2}{2} \end{pmatrix} \quad ; \quad \mathbf{H} = \begin{pmatrix} i \\ gh(S_{ox} - S_{fx}) - \tau_x / \rho \\ gh(S_{oy} - S_{fy}) - \tau_y / \rho \end{pmatrix} \tag{2}$$

Here, h is the depth, u and v the two horizontal depth averaged velocity components, g gravity, S_o the bed slope, S_f the friction slope and τ the friction on the water surface induced by wind.

A high resolution finite volume scheme, based on the Godunov scheme and the Roe Approximate Riemann solver [47], and using the Finite Volume Method is used. Special care is taken in the discretization of geometric source terms following the ideas of improved treatment developed by Vazquez–Cendon [48].

The resulting scheme is explicit, and is the base of Iber, a numerical model for simulating turbulent free surface unsteady flow and environmental processes in rivers and estuaries [49]. The ranges of application of Iber cover river hydrodynamics, dam-break simulation, flood zones evaluation, sediment transport calculation and wave flow in estuaries. The model can be run over an irregular mesh of triangles, quadrilaterals or a combination of both of them [50]. The wind effect is considered in the source term H in Equation (2) through τ_x and τ_y, which are the decomposition in the x and y directions of the wind stress over the water surface τ.

4.2.2. Wind Stress Formulations

The wind stress over the surface is expressed in terms of the bulk drag relation:

$$\tau = \rho u_*^2 = \rho C_D U_z^2 \quad (3)$$

where ρ is the mass density of air (about 1.225 kg·m^{-3}) and μ_* is the friction velocity, which is replaced by the measured wind velocity at a reference height U_z and a dimensionless drag coefficient C_D corresponding to that height z. The wind velocity profile ($\partial U/\partial z$) depends on surface roughness and atmospheric stability, whose influence is usually included in C_D. A variety of wind drag formulations have appeared in the past literature, most of them referred to a reference height of 10 m. In this work, we test five different schemes in order to achieve a satisfactory balance between field data requirements and quality of the modeling results. Table 2 summarizes the main characteristics of the formulation used in each simulation, named S1 to S5.

Table 2. Characteristics of the wind drag formulations of the simulations performed at the Membrillo event.

Simulation	Wind Profile	Drag Formulation	Atmospheric Stability	Low Wind Speed Correction
S1	Exponential	Constant	Neutral	No
S2	Exponential	Van Dorn	Neutral	No
S3	Logarithmic	Charnock	Non-neutral	No
S4	Logarithmic	Charnock	Neutral	No
S5	Logarithmic (exponential for low wind)	Charnock, (Wuest and Lorke for low wind)	Neutral	Yes

The simplest option for the wind drag modeling is performed in simulation S1 as a constant value of $C_D = 2.6 \times 10^{-3}$ given by Munk [51] for wind speeds measured at 10 m. Simulation S2 uses Van Dorn [52] wind drag expression:

$$C_D = 1.2\times10^{-3} \text{ for } U_{10} \leq 5.6 \text{ m/s} \quad (4)$$

$$C_D = 1.2\times10^{-3} + 2.25\times10^{-3}\left(1-\frac{5.6}{U_{10}}\right) \text{ for } U_{10} > 5.6 \text{ m/s} \quad (5)$$

In both cases, the wind speed at 10 m height is obtained from the power law wind profile:

$$\frac{U_{z1}}{U_{z2}} = \left(\frac{z_1}{z_2}\right)^m \quad (6)$$

where $m = 0.11$ is the empirically derived coefficient obtained by Hsu [53] for neutral atmospheric stability over the sea.

Taking into account the more realistic logarithmic wind profile above the surface and non-neutral atmospheric stability conditions, C_D can be written as [54],

$$C_D = k^2\left[\ln\left(\frac{z}{z_0}\right) - \Psi_m\left(\frac{z}{L}\right)\right]^{-2} \quad (7)$$

where $k = 0.41$ is von Kármán's constant. The surface roughness length z_0 is defined according to Charnock [55],

$$z_0 = \alpha \frac{u_*}{g} \tag{8}$$

where α = 0.0185 is the Charnock constant [54] and g is the gravitational constant. $\psi_m(z/L)$ is the Monin–Obukhov similarity function for momentum flux, which is neglected under neutral stability conditions (simulations S4 and S5 in Table 2). Under non-neutral stability conditions (simulation S3), this function is defined according to Hsu [56]:

$$\psi_m\left(\frac{z}{L}\right) = -5\frac{z}{L} \text{ for stable conditions } (z/L \geq 0) \tag{9}$$

$$\psi_m\left(\frac{z}{L}\right) = 1.0496\left(-\frac{z}{L}\right)^{0.4591} \text{ for unstable conditions } (z/L < 0) \tag{10}$$

According to Donelan [57], the stability parameter (z/L) is related to the bulk Richardson number Ri_B, such that for unstable conditions (*i.e.*, $T_w > T_a$)

$$\frac{z}{L} = 7.6 Ri_B \tag{11}$$

and for unstable conditions (*i.e.*, $T_a > T_w$)

$$\frac{z}{L} = 6.0 Ri_B \tag{12}$$

T_a and T_w being the air and water temperatures, respectively, and [54,56]

$$Ri_B = \frac{gz(T_a - T_w)}{(T_a + 273.2)U_z^2} \tag{13}$$

Equations (3), (7) and (8) define an implicit scheme which is solved for C_D. The solution is shown in Figure 8 for the range of observed values of U_2 and $\psi_m(z/L)$ during the period of study.

Figure 8. Wind drag coefficient C_D for a reference height of 2 m and for the range of observed values of wind speed U_2 and similarity function $\psi_m(z/L)$. Solution of the implicit Equations (3), (7) and (8).

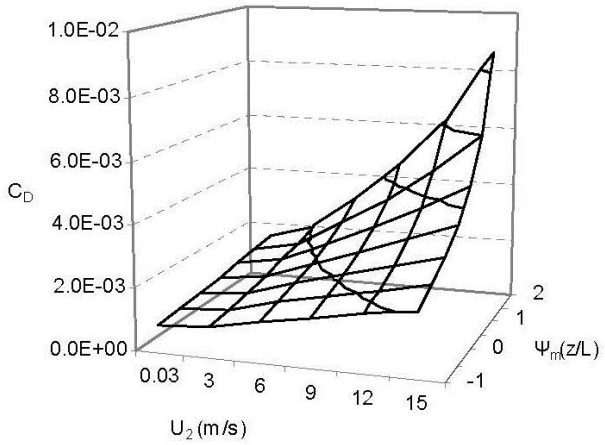

Furthermore, there is experimental evidence of the increase of C_D over water surfaces for weak winds under 5 m/s [58–60]. As about 60% of U_{10} estimations by Equation (6) during the modeling period fall under such wind conditions, simulation S5 performs the empirical expression proposed by Wuest and Lorke [61]:

$$C_D \approx 0.0044 U_{10}^{-1.15} \text{ for } U_{10} < 5 \text{ m/s} \quad (14)$$

4.2.3. Model Setup

The numerical model was based on a digital terrain model (DTM) of Doñana marshes built from a point elevation data set acquired on a LIDAR survey flight in September 2002. It has 2.00 m^2 and 0.15 m planimetric and elevation resolution, respectively [62]. The numerical computations were carried out on two irregular meshes of triangular elements (TIN), one for each of the two modeling areas of Ánsares and Membrillo drawn in Figure 1, obtained from the DTM.

Regarding the initial conditions, water volume for the Membrillo case of study was obtained via GIS techniques from the flood maps derived from the ASAR scenes together with the DTM of the marshes. For such purpose, the terrain elevation was subtracted from the water surface to obtain the observed water volume. In the Ánsares event, where water depth data were available, the water volume was chosen so as to coincide with the observed initial water depth at the measuring location. At initial time, a horizontal water surface is not expected to coincide with ASAR observations. For that reason, simulations started 4.5 days before the first ASAR observation of the Membrillo event, and 1.5 days before the unique ASAR observation of the Ánsares event.

Bottom friction of each case, implemented as a manning value, was chosen according to field observations by the authors. For the Membrillo event, a spatial distinction was made in the modeling area, setting a value of 0.125 at the scarcely vegetated northern third of the pond and a value of 0.030 at the non-vegetated rest of the pond. The Ánsares case was performed as a completely non-vegetated area with a manning value of 0.023.

Wind stress formulations are implemented in the numerical model without spatial variations or dependence on the presence of vegetation. Further details of the model setup of each case of study are shown in Table 3.

Table 3. Characteristics of the model setup for each case of study.

Case of Study	Computational Mesh (TIN)				Initial Volume (m^3)	Initial Time	Final Time
	Num. of Elements	Num. of Nodes	Min. Element Size (m)	Max. Element Size (m)			
Membrillo	52,348	27,381	12.5	200	1,956,337	25 February 2006 0000 h	4 March 2006 1,200 h
Ánsares	7,352	3,804	13.6	398	550,000/600,000	18 October 2006 0000 h	20 October 2006 0000 h

4.2.4. Model Performance

As the wind stress exerted over the water surface is theoretically dependent on atmospheric conditions, a greater number of observed events would be necessary to perform a desirable calibration-verification

procedure. For this reason, wind stress formulations are tested but calibration of their parameters is not performed.

In order to quantify the degree of agreement between simulated and ASAR imagery based flood maps, the fitting index in Equation (15) has been used [63–65]:

$$F = \frac{A}{B + C - A} \tag{15}$$

Parameter B in Equation (15) represents the observed flooded area on the ASAR image. C corresponds to the simulated flooded area at the time of the image acquisition. A is the overlapping between areas B and C.

5. Results and Discussion

5.1. Comparison of Wind Stress Formulations, Membrillo Event

Figure 9a shows the time series of the bulk wind drag coefficient C_D of the simulations performed in the Membrillo case of study, whose wind conditions were shown in Figure 2. To make them comparable, S1 and S2 coefficients have been adapted to a reference height of 2 m using the power law relation for neutral atmospheric stability Equation (6). The constant value of C_D in simulation S1 is noticeably higher than the rest, being from 1.74 to 2.54 times the average value of the other computed C_D coefficients during the period of study. The low wind speed correction used in simulation S5 greatly modifies the time evolution of C_D with respect to those time-dependant C_D of simulations S2, S3 and S4. However, as the highest values of C_D in S5 correspond to the lowest wind intensities, this difference is barely transferred to the effective wind stress exerted over the water surface, as shown in Figure 9b. According to the resulting wind drag coefficient, the highest wind stress is computed in simulation S1. Its intensity is only reached by the Van Dorn formulation (S2) in the case of strong winds, as can be seen on days 25, 26 February and 4 March. During most of the simulation period, wind stress computed in simulation S2 remains at a medium magnitude between S1 and the Charnock-based formulations of simulations S3, S4 and S5.

In order to better distinguish the effect of the different formulations performed, Figure 9c shows the accumulated wind stress over the water surface. At the end of the study period, simulations S1 and S2 have performed an accumulated stress of 1.89 and 1.32 times the wind stress obtained by the Charnock formulation for neutral stability (S4), respectively.

Modifications of the Charnock formulation computed in simulations S3 and S5 are intended to account for the physically sounded effect of the atmospheric stability and for previously reported experimental evidences of higher wind stresses at lower wind speeds, respectively. However, their accumulated effect over the 7.5 days of simulation only differs from the wind stress computed in simulation S4 by ±5%, as shown in Figure 9c. From a practical point of view, the influence of such modifications in this work seems to be negligible, taking into account their higher field data and computational requirements.

Figure 9. (**a**) Time series of simulated wind drag coefficient (notice that S1 and S2 are adapted to a 2 m reference height); (**b**) Time series of simulated wind stress at the water surface; (**c**) Time series of accumulated wind stress. Series are named according to Table 2.

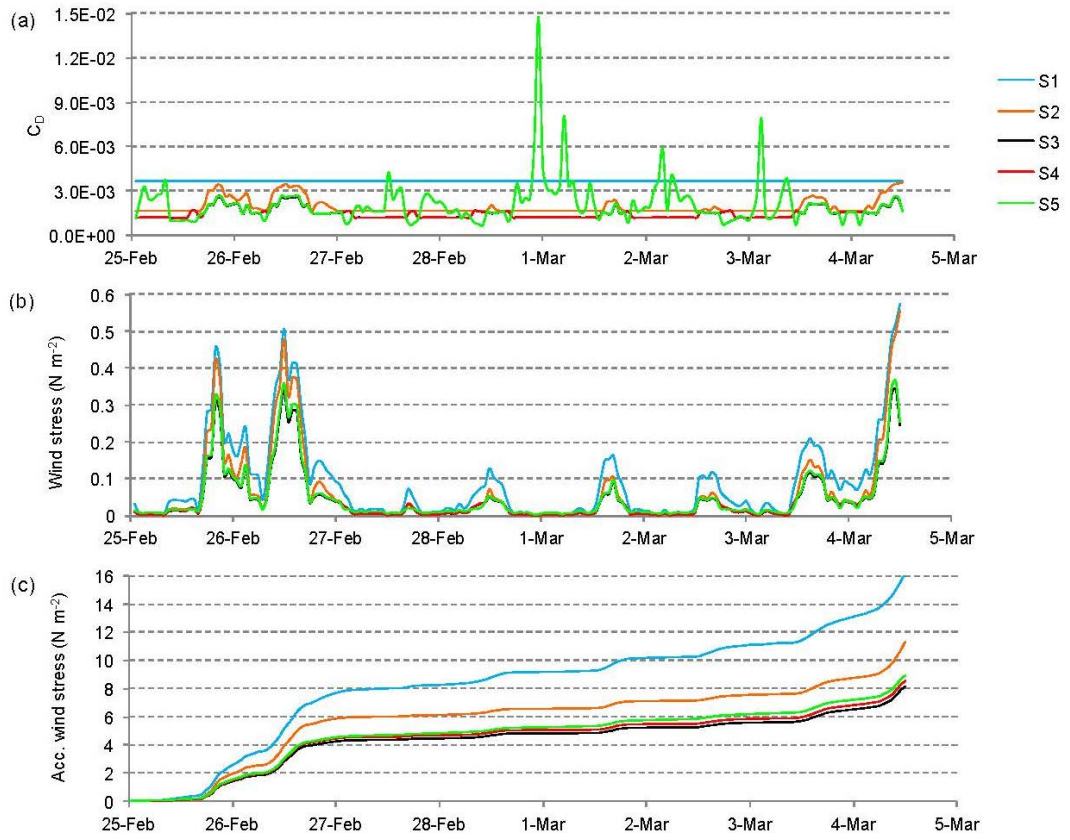

5.2. Modeling Results

5.2.1. Selection of the Wind Stress Formulation (Membrillo Event)

In order to assess the model capability to reproduce the wind-driven water movement and to choose the most suitable wind stress formulation, the flood extent of each simulation coincident with the ASAR scenes were compared with the flood contours obtained from the ASAR images. F parameters obtained for these comparisons are shown in Table 4.

As expected from the results presented in the previous section, little differences could be found between the Charnock-based formulations S3, S4 and S5, with a maximum model performance difference of 1% (F parameters in Table 4). Little but negligible differences were also found between them and the results of simulation S2, which despite having lower data requirements performs 1% better the flood extent of the second ASAR scene. Simulation S1 produced similar results for the first ASAR scene (1 March 2006), but overestimated the wind drag action at the time coincident with the second ASAR image (4 March 2006, the analogous situation of Figure 10d). Overall mean F values are 0.77 for simulations S2 to S5 and 0.76 for simulation S1. Tested formulations performed flood extent

on 1 March 2006 between 1% and 4% better than on 4 March 2006, mainly due to the excess of water displacement to the vegetated northern part of the pond. This points to the necessity of introducing wind stress spatial variations or an excess of resistance to flood (manning value) if modeling more vegetated areas during the growing season.

Table 4. F parameters obtained for the water extent of each simulation at the ASAR observation times.

	ASAR 01Mar06	ASAR 04Mar06	F med
S1	0.78	0.74	**0.76**
S2	0.78	0.77	**0.77**
S3	0.78	0.76	**0.77**
S4	0.79	0.76	**0.77**
S5	0.79	0.76	**0.77**
F med	**0.78**	**0.76**	**0.77**

By balancing field data requirements, computational efforts and modeling results, wind stress formulation of simulation S2 was chosen for further analyses and recommendations. Using the same data requirements as the formulation of S1, S2 performs an improvement up to 3% on the flood area estimation (Table 4). Charnock-based formulations S3 to S5 require more field data and computational time though they do not perform more than 1% improvement of the water extent estimation.

5.2.2. Analysis of the Membrillo Event

Figure 10 shows four time steps of the chosen model configuration: initial condition of horizontal water surface (Figure 9a); maximum flooded extension towards the south (Figure 10b); simulation time step coincident with the first ASAR image (Figure 10c); and simulation time step coincident with the second ASAR image (Figure 10d).

The initial time of all simulations is settled 4.5 days before the acquisition of the first ASAR image, a period of time expected to be long enough to minimize the influence of the initial condition of horizontal water surface. About 1.5 days before the first image, the wind starts to blow consistently from the north, with maximum intensity about 23 h before the time of the image acquisition (Figure 2). As shown in Figure 10b, the maximum simulated flooded extension towards the south, on 28 February 2006 1,500 h, approximates the flood contour of 1 March 2006. However, during the last 17 h before the ASAR image is taken, the wind remains calm (mostly under 1.5 m/s, Figure 2), and the water body tends to recover the horizontal surface. The lack of coincidence of the southern flooded area at the very same time of the first ASAR image, in Figure 10c, may respond to the different sensitivity of the techniques applied to determine the water extent. In the absence of vegetation, the algorithms applied to the ASAR image may be classified as a water-saturated sediment that was flooded a few hours before, whereas the numerical model identifies this area as dry through a wet-dry threshold of 1 mm of water height over a smooth computational mesh.

Figure 10. Modeling results of simulation S2, Membrillo case of study. (**a**) Horizontal water surface at initial time step, 25 February 2006 0000 h; (**b**) Maximum flooded extension towards the south, 28 February 2006 1,500 h; (**c**) Results coincident with first ASAR image, 1 March 2006 1,200 h; (**d**) Results coincident with second ASAR image, 4 March 2006 1,200 h.

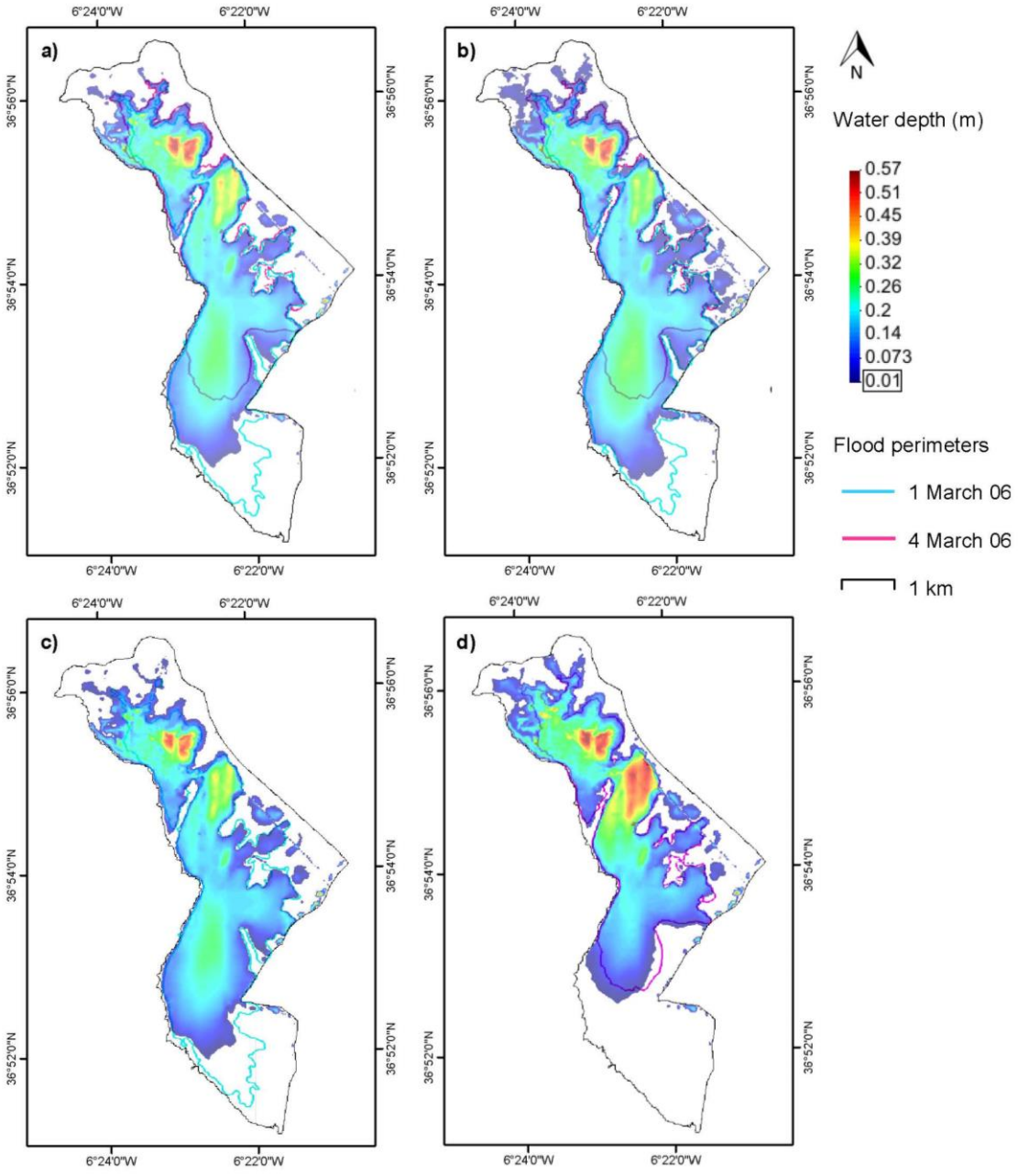

After the time of occurrence of the first image, a S-SW wind event starts to develop with maximum intensity approximately at the time of acquisition of the second ASAR image, as is represented in

Figure 10d. Both flooded areas compared in this figure coincide to a great extent. However, the numerically simulated water area seems to be moved towards the west with respect to the flood contour obtained from the ASAR image. The cause of this difference might be twofold: on the one hand, small altimetric errors in the marshes' DTM or in the computational TIN can change significantly the simulated water extent in this area, as the slopes of the terrain are minima; on the other hand, the wind measurement station D04 is located about 14 km from the modeling area, and slight rotations of the wind direction can occur inside the marshes despite their flatness, which are not accounted for in the numerical model.

5.2.3. Analysis of the Ánsares Event

The time series of measured wind velocity, wind direction and water depth during the Ánsares event on 18–19 October 2006 are shown in Figure 11, together with the estimated water depth at the measurement point by two simulations with different initial water volume. According to the measured water depth at the initial time, the event is firstly modeled with 5.5×10^5 m^3 (green line in Figure 11). In this configuration, the average error for estimated water depth is -8.8×10^{-3} m and the mean absolute error is 10.8×10^{-3} m. The model satisfactorily reproduces the observed water depth variations on 18 October, reproducing a decrease of up to 6 cm about 3 h after the wind event reaches its maximum velocity of 9.4 m/s. However, initial water volume seems to be insufficient, since water depth on 19 October with lower wind velocities tends to underestimate the measurements by 15×10^{-3} m. Moderate winds measured at the beginning of the simulation could explain a non-horizontal water surface and a higher water volume. Thus, a second simulation with an initial volume of 6.0×10^5 m^3 is also presented (blue line in Figure 11). In this case, average error for estimated water depth is 5.3×10^{-3} m and mean absolute error is 7.6×10^{-3} m. Although the results of 18 October are less satisfactory (mean error of 11.7×10^{-3} m), the modeled water depth on 19 October coincides to a great extent with measurements (mean error of -1.1×10^{-3} m). At the time of radar image acquisition, the error of water depth estimation is reduced to -3.3×10^{-3} m.

Figure 11. Comparison of field data and modeling results of the Ánsares case study. Two simulations are presented: estimated water depth with initial volume of 5.5×10^5 m^3 (green line) and with initial volume of 6.0×10^5 m^3 (blue line).

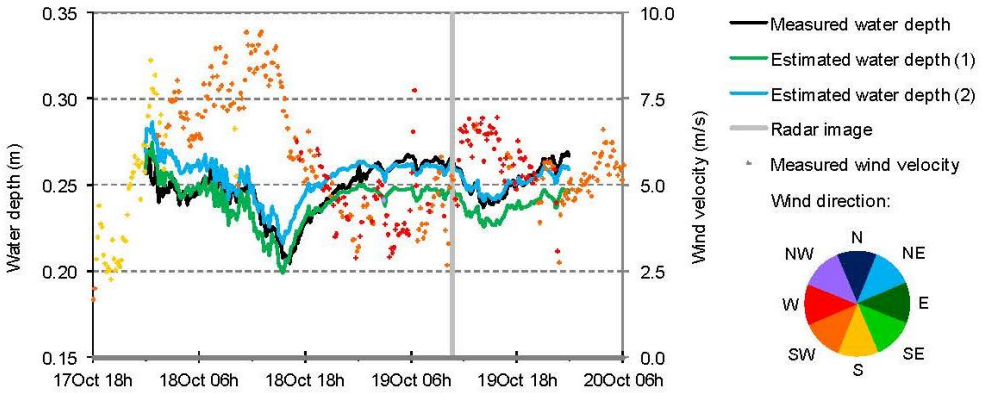

Figure 12 shows the water level and the water extent obtained at three different time steps of the Ánsares event simulation using an initial water volume of 6×10^5 m^3, together with the location of the D02 gauging station and the water perimeter obtained from the ASAR scene. Figure 12a shows the horizontal water surface at the beginning of the simulation (18 October 2006, 0000 h). The maximum water displacement towards the east due to the wind event on 18 October is presented in Figure 12b. At that time, the water body performs about 1 km displacement from the initial position and develops a mean surface slope of 0.1%, reaching the eastern water perimeter estimated by remote sensing techniques. Similar to the Membrillo event studied previously, the ASAR image is taken when the water body is recovering its horizontal surface (Figure 12c). The lack of coincidence of the eastern perimeter at the time of the ASAR image is also explained by the different sensitivity of the techniques applied to determine the water extent. This assumption is reinforced by results of simulated water depth in Figure 11.

Figure 12. Modeling results of the Ánsares event: Water level at (**a**) Initial time step, 18 October 2006 0000 h; (**b**) Maximum water displacement towards the east, 18 October 2006 1,530 h; (**c**) Date of ASAR image acquisition, 19 October 2006 1,040 h. Measurement point D02 and flood perimeter estimated from the ASAR scene are also shown (red dot and red line, respectively).

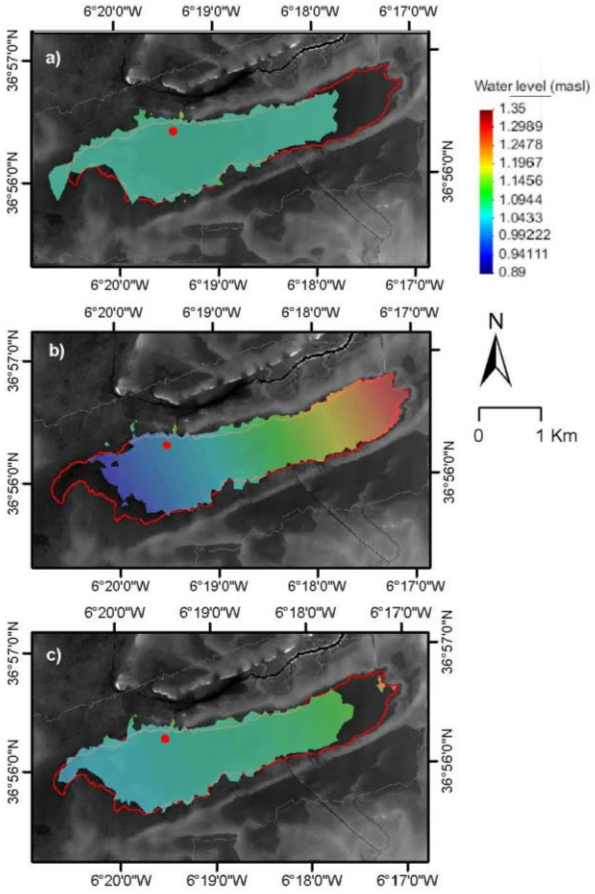

Taking into account that both Figure 12b and Figure 12c are jointly compared to the water extent obtained by the ASAR scene, simulated flood extents at those time steps were superimposed to evaluate the model performance. F values obtained were 0.87 for both initial water volumes of 5.5 and 6×10^5 m^3.

6. Conclusions

This paper describes the implementation of the wind stress action into the two-dimensional hydrodynamic model of Doñana marshes with the aid of Envisat/ASAR imagery. Given the flatness of the Doñana's terrain, remote sensing images provided valuable spatial data on the wind-induced water bodies' displacement. This information could barely be achieved by point field measurements.

Five wind stress formulations in the literature were introduced in the marshes' hydrodynamic model. On-site wind records were then used to simulate the water wind drag effect in an isolated water body, the Membrillo pond, by using the five formulations. Two ASAR observations of the Membrillo pond flooded area during the same wind episode were used to assess the modeling results.

The Van Dorn's expression [52] and the power law wind profile for neutral stability conditions were selected as the most appropriate wind stress modeling technique. This formulation requires less field data and computational effort than the Charnock-based expressions, and yielded satisfactory results with an overall F coefficient value of 0.77 [63–65]. The chosen formulation was verified by simulating a different wind event at the Ánsares pond, for which on-site wind records and ASAR imagery were also available.

Wind-induced water displacements up to 2 km were satisfactorily reproduced by the selected formulation, and water level variations were modeled with an average absolute error under 11 mm at 10 min calculation time steps. The maximum water displacements took place in time intervals of 12 to 18 h, in response to moderate and rather frequent wind velocities, below 15 m/s. In the presented study cases, the inclusion of atmospheric stability considerations and the increase of the wind drag coefficient at low wind speeds led to no significant improvement of the modeling results, with an increment of the F value under 1%.

Future lines of research will aim at mapping vegetation biomass by using polarimetric SAR imagery. These vegetation data will be implemented in the hydrodynamic model to spatially reproduce bedload resistance to flow, surface wind shear-stress reduction and evapotranspiration water losses. Further efforts will focus on modeling and calibrating water quality parameters of ecological relevance, such as wind-induced sediment resuspension and turbidity.

Acknowledgments

The ASAR data used in this study was provided by the European Space Agency within the frame of a Category 1 User Agreement with the Flumen Institute. The study was undertaken in the frame of projects funded by the Plan Nacional de I+D+i of the Spanish Ministry of Science and Innovation (projects CGL2006-02247/BOS and CGL2004-05503-C02), by the Andalusian Water Agency and by the European Commission VII Framework Programme (project RAMWASS GOCE-CT-2006-037081). The authors would also like to express their gratitude to the Col·legi d'Enginyers de Camins, Canals i

Ports de Catalunya for its important sponsorship to PhD students and to the technicians of the Doñana Natural Area: Carlos Urdiales, Abel Valero and Diego García, for their valuable and friendly assistance.

Conflicts of Interest

The authors declare no conflict of interest.

References

1. García-Novo, F.; Marín-Cabrera, C. *Doñana: Agua y Biosfera*; Ministerio de Medio Ambiente: Sevilla, Spain, 2005.
2. Gómez-Rodríguez, C.; Bustamante, J.; Díaz-Paniagua, C. Evidence of hydroperiod shortening in a preserved system of temporary ponds. *Remote Sens.* **2010**, *2*, 1439–1462.
3. Suso, J.; Llamas, M.R. Influence of groundwater development on the Doñana-National-Park ecosystems (Spain). *J. Hydrol.* **1993**, *141*, 239–269.
4. Muñoz-Reinoso, J.C. Vegetation changes and groundwater abstraction in SW Doñana, Spain. *J. Hydrol.* **2001**, *242*, 197–209.
5. Menanteau, L. Evolución Histórica y Consecuencias Morfológicas de la Intervención Humana en las Zonas Húmedas: El Caso de las Marismas del Guadalquivir. In *Las Zonas Húmedas en Andalucía*; Dirección General de Medio Ambiente, Ministerio de Obras Públicas y Urbanismo: Madrid, Spain, 1984; pp. 43–76.
6. Saura, J.; Bayán, B.; Casas, J.; Ruiz de Larramendi, A.; Urdiales, C. *Documento Marco Para el Desarrollo del Proyecto Doñana 2005. Regeneración Hídrica de las Cuencas y Cauces Vertientes a las Marismas del Parque Nacional de Doñana*; Ministerio de Medio Ambiente: Madrid, Spain, 2001.
7. Bladé-Castellet, E.; Gómez, M. *Modelación del Flujo en Lámina Libre Sobre Cauces Naturales. Análisis Integrado en una y dos Dimensiones (Monografía CIMNE, 97)*; CIMNE: Barcelona, Spain, 2006.
8. European Space Agency. *ASAR Product Handbook, Issue 2.2*; ESA: Paris, France, 2007.
9. Marti-Cardona, B.; Lopez-Martinez, C.; Dolz-Ripolles, J.; Bladé-Castellet, E. ASAR polarimetric, multi-incidence angle and multitemporal characterization of Doñana wetlands for flood extent monitoring. *Remote Sens. Environ.* **2010**, *114*, 2802–2815.
10. Ferrarin, C.; Umgiesser, G.; Scroccaro, I.; Matassi, G. Hydrodynamic modeling of the lagoons of Marano and Grado, Italy. *GeoEcoMarina* **2009**, *15*, 13–19.
11. Kjerfve, B.; Magill, K.E. Geographic and hydrodynamic characteristics of shallow coastal lagoons. *Mar. Geol.* **1989**, *88*, 187–199.
12. Pasternack, G.B.; Hinnov, L.A. Hydrometeorological controls on water level in a vegetated Chesapeake Bay tidal freshwater delta. *Estuar. Coast. Shelf Sci.* **2003**, *58*, 367–387.
13. Reed, R.E.; Dickey, D.A.; Burkholder, J.M.; Kinder, C.A.; Brownie, C. Water level variations in the Neuse and Pamlico Estuaries, North Carolina due to local and remote forcing. *Estuar. Coast. Shelf Sci.* **2008**, *76*, 431–446.

14. Ramos-Fuertes, A. Hidrometeorología y Balance Térmico de la Marisma de Doñana. Ph.D. Thesis, Universitat Politècnica de Catalunya, Escola Tècnica Superior d'Enginyers de Camins, Canals i Ports de Barcelona, Barcelona, Spain, 2012.
15. Ji, Z.G.; Morton, M.R.; Hamrick, J.M. Wetting and drying simulation of estuarine processes. *Estuar. Coast. Shelf Sci.* **2001**, *53*, 683–700.
16. Marti-Cardona, B.; Steissberg, T.E.; Schladow, S.G.; Hook, S.J. Relating fish kills to upwellings and wind patterns in the Salton Sea. *Hydrobiologia.* **2008**, *604*, 85–95.
17. Mans, C.; Bramato, S.; Baquerizo, A.; Losada, M. Surface seiche formation on a shallow reservoir in complex terrain. *J. Hydraul. Eng.* **2011**, *137*, 517–529.
18. Somes, N.L.G.; Bishop, W.A.; Wong, T.H.F. Numerical simulation of wetland hydrodynamics. *Environ. Int.* **1999**, *25*, 773–779.
19. Min, J.; Wise, W.R. Depth-averaged, spatially distributed flow dynamic and solute transport modelling of a large-scaled, subtropical constructed wetland. *Hydrol. Process.* **2010**, *24*, 2724–2737.
20. Markfort, C.D.; Perez, A.L.S.; Thill, J.W.; Jaster, D.A.; Porté-Agel, F.; Stefan, H.G. Wind sheltering of a lake by a tree canopy or bluff topography. *Water Resour. Res.* **2010**, *46*, doi:10.1029/2009WR007759.
21. Cózar, A.; Gálvez, J.A.; Hull, V.; García, C.M.; Loiselle, S.A. Sediment resuspension by wind in a shallow lake of Esteros del Iberá (Argentina): A model based on turbidimetry. *Ecol. Model.* **2005**, *186*, 63–76.
22. Zijlema, M.; van Vledder, G.P.; Holthuijsen, L.H. Bottom friction and wind drag for wave models. *Coast. Eng.* **2012**, *65*, 19–26.
23. Martín, M.; López, J.A.; López, L.; Mantecón, R.; Cantos, R.; Coleto, I. *Hidrogeologia del Parque Nacional de Doñana y su entorno*; Instituto Tecnólogico Geominero de España: Madrid, Spain, 1992.
24. Siljeström, P.; Clemente, L.; Rodriguez-Ramirez, A. Clima. In *Parque Nacional de Doñana*; García Canseco, V., Ed.; Canseco Editores: Talavera de la Reina, Spain, 2002; pp. 43–56.
25. Bayán, B.J.; Dolz, J. Las aguas superficiales y la marisma del Parque Nacional de Doñana. *Revista de Obras Públicas* **1995**, *142*, 17–29.
26. Aragonés, D.; Díaz-Delgado, R.; Bustamante, J. Tratamiento de una Serie Temporal Larga de Imágenes Landsat Para la Cartografía de la Inundación Histórica de las Marismas de Doñana. In Proceedings of the XI Congreso Nacional de Teledetección, Puerto de la Cruz, Tenerife, Spain, 21–23 September 2005; pp. 407–410.
27. García, J.I.; Mintegui, J.A.; Robredo, J.C. *La Vegetación en la Marisma del Parque Nacional de Doñana en Relación con su Régimen Hidráulico*; Organismo Autónomo de Parques Nacionales: Madrid, Spain, 2005.
28. Salvia, M.; Franco, M.; Grings, F.; Perna, P.; Martino, R.; Karszenbaum, H.; Ferrazzoli, P. Estimating flow resistance of wetlands using SAR images and interaction models. *Remote Sens.* **2009**, *1*, 992–1008.
29. Grings, F.; Ferrazzoli, P.; Karszenbaum, H.; Tiffenberg, J.; Kandus, P.; Guerriero, L.; Jacobo-Berrles, J.C. Modeling temporal evolution of junco marshes radar signatures. *IEEE Trans. Geosci. Remote Sens.* **2005**, *43*, 2238–2245.

30. Reschke, J.; Bartsch, A.; Schlaffer, S.; Schepaschenko, D. Capability of C-band SAR for operational wetland monitoring at high latitudes. *Remote Sens.* **2012**, *4*, 2923–2943.
31. Kuenzer, C.; Guo, H.; Huth, J.; Leinenkugel, P.; Li, X.; Dech, S. Flood mapping and flood dynamics of the Mekong delta: ENVISAT-ASAR-WSM based time series analyses. *Remote Sens.* **2013**, *5*, 687–715.
32. Kussul, N.; Shelestov, A.; Skakun, S. Flood Monitoring on the Basis of SAR Data. In *Use of Satellite and in-situ Data to Improve Sustainability, NATO Science for Peace and Security Series C: Environmental Security*; Kogan, F., Powell, A., Fedorov, O., Eds.; Springer: Dordrecht, The Netherlands, 2011; pp. 19–29.
33. Skakun, S. A neural network approach to flood mapping using satellite imagery. *Comput. Inform.* **2010**, *29*, 1013–1024.
34. Cossu, R.; Schoepfer, E.; Bally, P.; Fusco, L. Near real-time SAR-based processing to support flood monitoring. *J. Real Time Image Process.* **2009**, *4*, 205–218.
35. Ramos, A.; Martí-Cardona, B.; Rabadà, J.; Dolz, J. Hydrometeorology and Heat Balance in a Shallow Wetland: Contribution of Field Data and Remote Sensing to the Understanding of Doñana Marshes. In Proceedings of the International Conference on Ecohydrology and Climate Change, Tomar, Portugal, 10–12 September 2009.
36. Rosich, B.; Meadows, P. *Absolute Calibration of ASAR Level 1 Products Generated with PF-ASAR*; ESA-ESRIN: Frascati, Italy, 2004.
37. Kozlov, I.E.; Kudryavtsev, V.N.; Johannessen, J.A.; Chapron, B.; Dailidiene, I.; Myasoedov, A.G. ASAR imaging for coastal upwelling in the Baltic Sea. *Adv. Space Res.* **2012**, *50*, 1125–1137.
38. Marti-Cardona, B.; Dolz-Ripolles, J.; Lopez-Martinez, C. Wetland inundation monitoring by the synergistic use of ENVISAT/ASAR imagery and ancilliary spatial data. *Remote Sens. Environ.* **2013**, *139*, 171–184.
39. Díaz-Delgado, R.; Bustamante, J.; Pacios, F.; Aragonés, D. Hydroperiod of Doñana Marshes: Natural or Anthropic Origin of Inundation Regime? In Proceedings of the 1st GlobWetland Symposium: Looking at Wetlands from Space, Frascati, Italy, 19–20 October 2006.
40. Marti-Cardona, B.; Dolz-Ripolles, J. On the Synergistic Use of Envisat/ASAR Imagery and Ancillary Spatial Data for Monitoring Doñana Wetlands. In Proceedings of the ESA Living Planet Symposium, Edinburgh, UK, 9–13 September 2013.
41. Marti-Cardona, B.; Dolz-Ripolles, J.; Lopez-Martinez, C. Imágenes SAR para la Cartografía de Doñana: Beneficios del Filtrado Asistido por Información Espacial Auxiliar. In Proceedings of the XV Congreso de la Asociación Española de Teledetección, Madrid, Spain, 22–24 October 2013.
42. Mahalanobis, P.C. On the generalized distance in statistics. *Proc. Natl. Inst. Sci. (Calcutta)* **1936**, *2*, 49–55.
43. Luque, C.J.; Rubio-Casal, A.E.; Álvarez, A.A.; Muñoz, J.; Vecino, I.; Doblas, D.; Leira, P.; Redondo, S.; Castillo, J.; Mateos, E.; *et al. Memoria de Vegetación: Parque Nacional de Doñana. Proyecto de Cartografía y Evaluación de la Flora y Vegetación Halófita y de los Ecosistemas de Marismas que se encuentren dentro de la Red de Espacios Naturales Protegidos de Andalucía*; Consejería de Medio Ambiente de la Junta de Andalucía & Universidad de Sevilla: Sevilla, Spain, 2005.

44. García-Murillo, P.; Fernández-Zamudio, R.; Cirujano, S.; Sousa, S. Flora y vegetación de la marisma de Doñana en el marco del proyecto de restauración ecológica Doñana 2005. *Limnetica* **2007**, *2*, 319–330.
45. Dolz, J.; Bladé Castellet, E.; Gili, J.A. Modelo Numérico de la Hidrodinámica de la Marisma de Doñana. In *Doñana, Agua y Biosfera*; García Novo, F., Marín Cabrera, C., Eds.; Confederación Hidrográfica del Guadalquivir, Ministerio de Medio Ambiente: Madrid, Spain, 2005; pp. 149–150.
46. Iberaula. Available online: http://www.iberaula.es (accessed on 6 May 2013).
47. Roe, P.L. Approximate Riemann solvers, parameter vectors, and difference schemes. *J. Comput. Phys.* **1981**, *43*, 357–372.
48. Vázquez-Cendón, M.E. Improved treatment of source terms in upwind schemes for the shallow water equations in channels with irregular geometry. *J. Comput. Phys.* **1999**, *148*, 497–526.
49. Bladé, E.; Cea, L.; Corestein, G.; Escolano, E.; Puertas, J.; Vázquez-Cendón, E.; Dolz, J.; Coll, A. Iber—River modelling simulation tool. *Revista Internacional de Métodos Numéricos para Cálculo y Diseño en Ingeniería* **2014**, *30*, 1–10.
50. Bladé, E.; Gómez-Valentín, M.; Dolz, J.; Aragón-Hernández, J.L.; Corestein, G.; Sánchez-Juny, M. Integration of 1D and 2D finite volume schemes for computations of water flow in natural channels. *Adv. Water Resour.* **2012**, *42*, 17–29.
51. Munk, W.H. Wind stress on water: An hypothesis. *Q. J. R. Meteorol. Soc.* **1955**, *81*, 320–332.
52. Van Dorn, W.G. Wind stress on an artificial pond. *J. Mar. Res.* **1953**, *12*, 249–276.
53. Hsu, S.A.; Meindl, E.A.; Gilhousen, D.B. Determining the power-law wind-profile exponent under near-neutral stability conditions at sea. *J. Appl. Meteorol.* **1994**, *33*, 757–765.
54. Arya, S.P. *Introduction to Micrometeorology*, 2nd ed.; Academic Press: San Diego, CA, USA, 2001.
55. Charnock, H. Wind stress on a water surface. *Q. J. R. Meteorol. Soc.* **1955**, *81*, 639–640.
56. Hsu, S.A. Estimating overwater friction velocity and exponent of power-law wind profile from gust factor during storms. *J. Waterw. Port Coast. Ocean Eng.* **2003**, *129*, 174–177.
57. Donelan, M. The Dependence of the Aerodynamic Drag Coefficient on Wave Parameters. In Proceedings of the First International Conference on Meteorology and Air-Sea Interaction of the Coastal Zone, The Hague, The Netherlands, 1982; pp. 381–387.
58. Bradley, E.F.; Coppin, P.A.; Godfrey, J.S. Measurements of sensible and latent heat flux in the western equatorial Pacific Ocean. *J. Geophys. Res.: Ocean.* **1991**, *96*, 3375–3389.
59. Yelland, M.; Taylor, P.K. Wind stress measurements from the open ocean. *J. Phys. Oceanogr.* **1996**, *26*, 541–558.
60. Mitsuta, Y.; Tsukamoto, O. Drag coefficients in light wind. *Bull. Disaster Prev. Res. Inst.* **1978**, *28*, 25–32.
61. Wüest, A.; Lorke, A. Small-scale hydrodynamics in lakes. *Annu. Rev. Fluid Mech.* **2003**, *35*, 373–412.
62. Ibáñez, E. Validación de Modelos Digitales del Terreno de Precisión a Partir de Datos Láser Escáner Aerotransportado. Aplicación a la Marisma del Parque Nacional de Doñana. Ph.D. Thesis, Universitat Politècnica de Catalunya, Escola Tècnica Superior d'Enginyers de Camins, Canals i Ports de Barcelona, Barcelona, Spain, 2008.
63. Prestininzi, P.; di Baldassarre, G.; Schumann, G.; Bates, P.D. Selecting the appropriate hydraulic model structure using low-resolution satellite imagery. *Adv. Water Resour.* **2011**, *34*, 38–46.

64. Bates, P.D.; de Roo, A.P.J. A simple raster-based model for flood inundation simulation. *J. Hydrol.* **2000**, *236*, 54–77.
65. Horritt, M.S.; Bates, P.D. Predicting floodplain inundation: Raster-based modelling *versus* the finite-element approach. *Hydrol. Process.* **2001**, *15*, 825–842.

Annex 7:
Manuscript

Local Isotropy Indicator for SAR Image Filtering: Application to Envisat/ASAR Images of the Doñana Wetlands

LOCAL ISOTROPY INDICATOR FOR SAR IMAGE FILTERING: APPLICATION TO ENVISAT/ASAR IMAGES OF THE DOÑANA WETLANDS

Belén Martí-Cardona[1], Carlos López-Martínez[2], Josep Dolz-Ripollés[1]

1. Flumen Institute, Dept. of Hydraulic, Maritime and Environmental Eng., Universitat Politècnica de Catalunya (UPC), Barcelona, Spain
2. Remote Sensing Lab., Dept. of Signal Processing and Communications, Universitat Politècnica de Catalunya (UPC), Barcelona, Spain

Corresponding author: Belen Marti-Cardona, Jordi Girona 1 D1-208, 08034 Barcelona, Spain.
Email: belen.marti@upc.edu; telephone: (34)934016881.

ABSTRACT

Most recent speckle filtering algorithms combine statistical and geometrical criteria to reduce speckle noise while preserving image structure in SAR images. The statistical and geometrical criteria are generally based on the coefficient of variation and the ratio edge detector, respectively. These filters normally aim at reconstructing the scene local radar cross section, and the filtering degree is reduced over textured areas with high coefficient of variation relative to the image equivalent number of looks. As a consequence, intensity fluctuations within textured cover types are less smoothed, hindering a posterior land cover classification.

Envisat/ASAR scenes of the Doñana wetlands, in southwest Spain, showed high variance texture over some flooded vegetation areas. Additionally, boundaries between cover types were often smooth transitions, giving rise to backscattering spatial gradients on the image. This paper presents a geometrical operator, named Ds, for local isotropy assessment on SAR images. It is assumed that isotropic intensity distributions in natural areas, either textured or non-textured, correspond to a single cover type. The intensities within isotropic areas were averaged in order to flatten fluctuations within cover types and facilitate a subsequent land cover classification.

The speckle statistical properties were used to determine suitable Ds thresholds for discriminating heterogeneous targets from textured cover types at different window sizes. An assessment of Ds as an edge detector showed similar sensitivity than the ratio edge operator to spot straight, sharp boundaries, centered in the processing window, but significantly larger for detecting the inclusion of heterogeneities during the window expansion in multi-resolution filtering. Additionally, Ds presents the advantage versus the ratio edge coefficient of being

rotationally invariant, and its computation indicates the direction of the main intensity gradient in the processing window. Furthermore, the Ds parameter is shown to have a known statistical distribution over homogeneous areas.

The Ds operator was used in a multi-resolution fashion for filtering Doñana marshes ASAR scenes, acquired at diverse phenological stages and incidence angles. Results showed high degree of smoothing within cover classes, plus effective spatial adaptation to gradient gentleness and irregular boundaries, substantiating the usefulness of this operator.

1. INTRODUCTION

The Doñana National Park wetlands, in southwest Spain, constitute a highly dynamic landscape: up to 30,000 ha flood throughout fall and winter, helophyte vegetation emerges from large part of the water surface during the springtime and all water bodies plus helophytes dry up in summer [1], [2], [3], [4]. Flood extent in Doñana was monitored from September 2006 to July 2007 using Envisat/ASAR images in Alternated Polarization mode and HH/VV channels [5]. The scenes were acquired at the seven ASAR incidence angles in order to achieve high observation frequency during the inundation process, when the flood extent increases rapidly.

Delineation of the flooded areas required filtering the scenes to smooth out backscattering fluctuations owing to speckle and texture. Literature on speckle filtering is vast. Among the simplest methods are the boxcar or median filters, which perform well at smoothing speckle, but blur edges between different land cover types. Lee [6], Frost [7] and Kuan´s [8] algorithms improve SAR image filtering performance by making use of the statistical properties of speckle [9]. These algorithms use the coefficient of variation (*CV*) to measure local stationarity of pixel intensities and different degrees of filtering are applied accordingly. They are effective to approximate the terrain's mean backscattering coefficient in homogeneous and textured targets but, again, might smear edges to some degree.

In order to preserve image structure and border sharpness, geometric criteria were introduced in the filtering process. The aim was to identify edges within the processing window and adapt the filtering neighborhood to them. In this line Lee [10] proposed the use of gradient operators to detect edges in four directions (up-down, right-left, and diagonals). Touzi [11] adopted a similar approach but used ratio operators, referred to as r_2, more adapted to the multiplicative nature of speckle noise than the gradient operators. Ever since different authors have successfully combined geometrical criteria based on ratio edge detectors and statistical filters, mostly Lee's

and Frost's, to smooth speckle effects while preserving boundary definition in SAR images [12], [13], [14], [15], [16], [17].

The ratio edge detector, used by the above referenced authors, is well adapted to spot straight and abrupt edges. But in natural environments, where boundaries take capricious geometries and can be gradual, its effectiveness can be improved, as shown is this work. The filtering of Doñana marshes scenes for flood mapping brought up the need to determine maximum homogeneous areas in presence of texture and of irregular or gentle edges. Following this need, a new geometrical operator named *Ds* is proposed to assess local isotropy on SAR images in Section 2.1. The isotropy of a processing window is assumed to be an indicator of homogeneity or single class membership. The Ds performance as a heterogeneity detector is assessed in the same section. Its capability to identify the border between targets is compared to that of the *CV* and r2 operators in different scenarios: presence of straight and irregular boundaries, and in the case of spatial gradients. Section 3 introduces a methodology for the use of the *Ds* operator as an isotropy indicator in the multi-resolution speckle filtering of SAR images. This methodology is applied to a series of Envisat/ASAR images of the Doñana marshes and results for scenes acquired at different incidence angles and marshes phenological stages are presented in Section 3.4.

2. PARAMETER *DS* FOR LOCAL ISOTROPY ASSESSMENT

2.1 Definition

Expressions (1), (2) and (3) define a geometrical operator, named *Ds*, for local isotropy assessment on SAR images. In these expressions *I* stands for pixel value, *i, j* denote image row and column, *N* represents the processing neighborhood and C_i, C_j are the image coordinates of the neighborhood geometrical center.

$$D_i = \frac{\sum_i \sum_j \ i \cdot I(i,j)}{\sum_i \sum_j I(i,j)}, \quad \forall\, (i,j) \in N \qquad (1)$$

$$D_j = \frac{\sum_i \sum_j \ j \cdot I(i,j)}{\sum_i \sum_j I(i,j)}, \quad \forall\, (i,j) \in N \qquad (2)$$

$$Ds = \sqrt{(D_i - C_i)^2 \ + \ (D_j - C_j)^2} \qquad (3)$$

Ds is referred to as geometrical because its definition depends on the pixel values spatial arrangement, so that image windows with identical histograms can have different *Ds* values. *Ds*

represents the first order central moment of the processing neighborhood, normalized by the total intensity. More intuitively, *Ds* represents the distance in pixels between the neighborhood geometrical centroid and what would be the gravity center if the pixel values were masses, referred to as intensity centroid. This distance provides a measurement of the intensities spatial imbalance, so that Ds yields small values for isotropic distributions (where geometrical and intensity centroids would be almost coincident) and large ones when high and low intensities are preferently clustered in two different segments of the neighborhood. Fig. 1 aids the interpretation of the Ds parameter.

Some interesting properties of the Ds parameter can be readily drawn from its definition: firstly, the Ds value is rotationally invariant. Secondly, the image physical dimensions (intensity, amplitude, etc.) are cancelled out by the denominator in (2) and (3), so the *Ds* parameter can be used as an isotropy measure on any image type. Finally, the vector defined by the neighborhood geometrical and intensity centers, vector (Dj-Cj, Di-Ci), indicates the direction of the spatial the imbalance.

When using Ds for filtering SAR images, the speckle noise stochastic properties are introduced through the thresholds used to discriminate between homogeneous and heterogeneous targets, as discussed in Section 2.2.

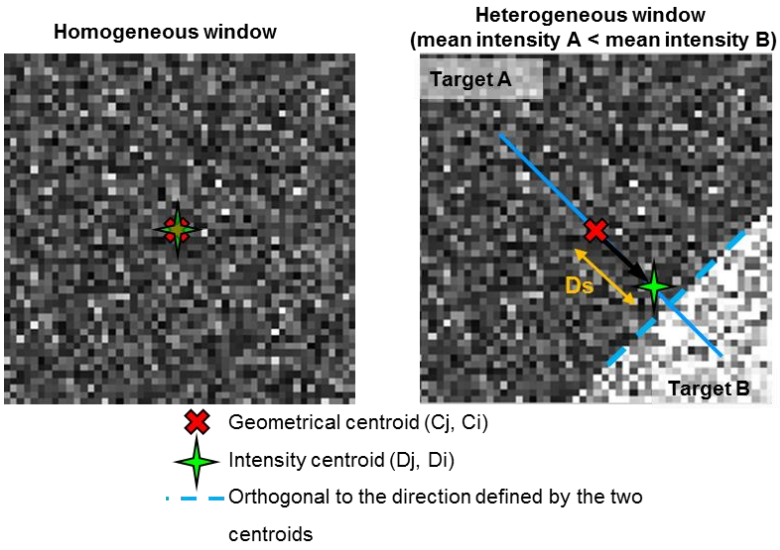

Fig. 1. Graphical representation of the filtering window geometrical centroid, intensity centroid, and Ds value.

2.2 Assessment of *Ds* as a heterogeneity detector

The pdf of parameter *Ds* operating over a SAR image of a homogeneous target has been estimated through Monte Carlo simulations. In absence of texture and spatial correlation, homogeneous target intensities can be modeled by independent realizations of a negative exponential distribution for single-look SAR images, and a gamma distribution when the number of looks is higher than 1 [18]. A synthetic square image was generated so that pixel values were independent realizations of the same gamma distribution (same *CV* and mean) and the corresponding *Ds* value was computed through expressions (1), (2) and (3). This process was repeated 20,000 times. The occurrence frequency of the *Ds* values approximates the *Ds* pdf. Fig. 2 shows some of the resultant pdf's, which are independent of the mean intensity and window size. They depend only on the *CV*, becoming wider as the *CV* increases.

If the synthetic image is generated using other intensity distributions (eg. Gaussian, Negative Exponential, Rayleigh, etc.), the Ds pdf turned out to be the same in all cases, as shown in Fig. 3. Hence, it can be said that the Ds pdf over a homogeneous target, meaning by homogeneous that the pixels' intensity can be modeled by independent realizations of the same statistical distribution, does not depend on the distribution type, the mean intensity, nor the processing window size. The Ds pdf is only determined by the pixel values' standard deviation to mean ratio or CV.

The value of *Ds* over a heterogeneous window comprising pixels of two different gamma distributions was simulated in presence of straight and irregular, sharp and gentle boundaries, and in the case that the edge is or not centered within the processing window. Fig. 4 depicts the simulated geometries. Fig. 5 and Fig. 6 show the *Ds* pdf of a heterogeneous target (geometry A in Fig. 4) computed using different window sizes and contrast values.

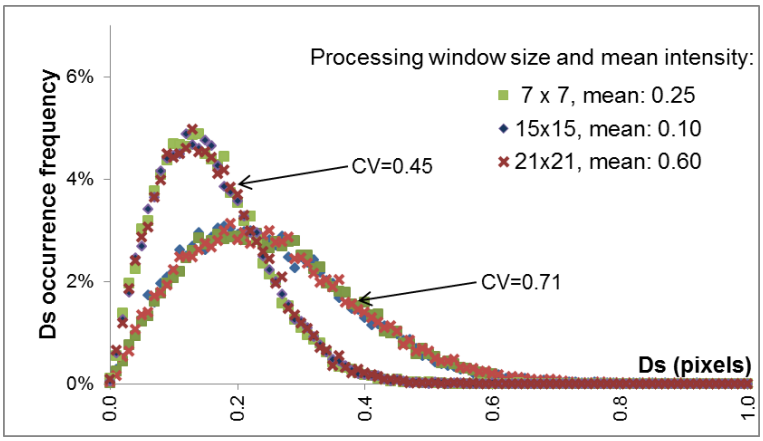

Fig. 2. *Ds* pdf obtained through Monte Carlo simulations of synthetic SAR images with different sizes and gamma-distributed pixel intensities.

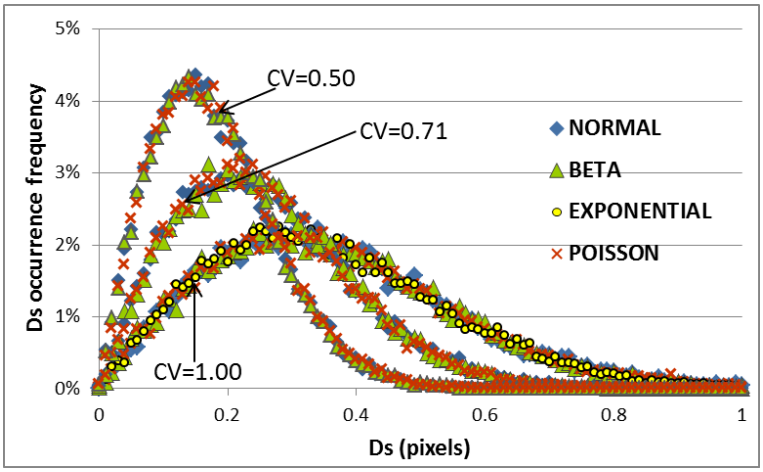

Fig. 3. Ds pdf obtained through Monte Carlo simulations of homogeneous target SAR images, for different pixel intensity distributions.

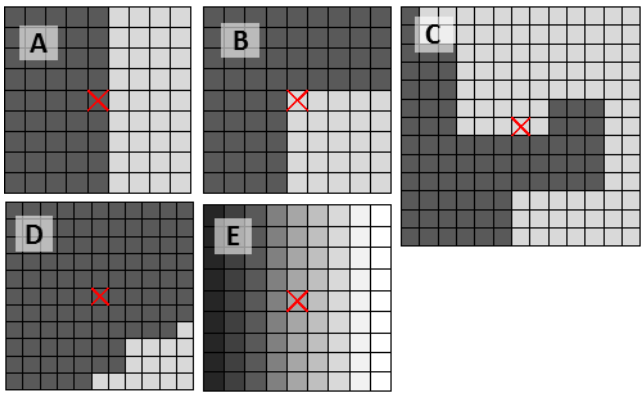

Fig. 4. Processing window geometries.

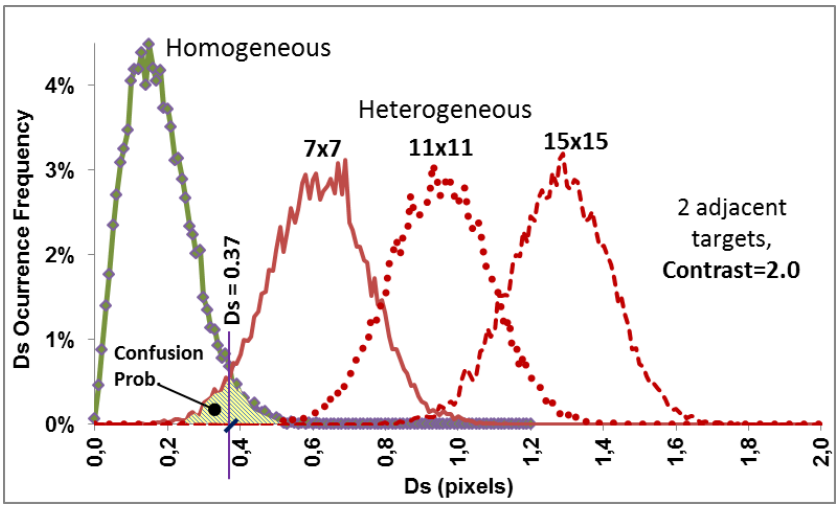

Fig. 5. *Ds* pdf obtained through Monte Carlo simulations of heterogeneous targets (geometry A) of contrast 2 and different window sizes (ENL=4).

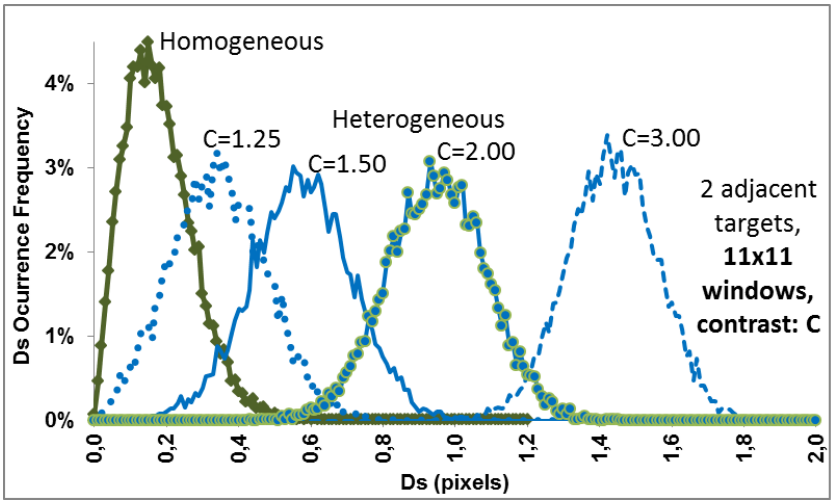

Fig. 6. *Ds* pdf obtained through Monte Carlo simulations of heterogeneous targets (geometry A) of different contrasts in 11x11 pixel windows (ENL=4).

When filtering speckle and texture fluctuations in a SAR image, it is necessary to test the stationarity of the processing window, so that the computation of filtered values avoids using pixels from different targets. In order to decide on the stationarity of a pixel neighborhood based on the corresponding *Ds* value, a threshold needs to be chosen, as done with the ratio edge detector or the *CV* [14], [15], [16]. To evaluate the performance of *Ds* as a heterogeneity indicator, the confusion probability has been defined as the average likelihood of missrecognizing a heterogeneous window as homogeneous or conversely. Given a *Ds* threshold, *Th*, the confusion probability is computed through expression (4) and graphical interpretation is given by the shaded area in Fig. 5, for threshold 0.37, window size 7x7 and contrast 2.

$$\boldsymbol{PConf}(Th) = \frac{\boldsymbol{PHomo}(Ds \geq Th) + \boldsymbol{PHetero}(Ds < Th)}{2} \qquad (4)$$

Given a particular window size and contrast, the best performance threshold will be the one that minimizes the confusion probability of (4). This best threshold coincides with the *Ds* value where homogeneous and heterogeneous pdf curves intersect (e.g. value 0.37 for window size 7x7 and contrast 2 in Fig. 5). When moving a processing window on a SAR image the user can fix the window size, but edges with many different contrasts can be found. Then the optimal threshold might be selected for each window size as the one which minimizes the confusion probability integrated over the entire range of contrasts to be considered. The confusion probability when using Ds for detecting edges in an 11x11 processing window is plotted in Fig. 7 as a function of the used Ds threshold and for different contrasts between adjacent targets. For this window size, 0.31 is the optimal threshold, that is, the thresholds minimizing the confusion probability when contrasts between 1.25 and 4.0 are considered.

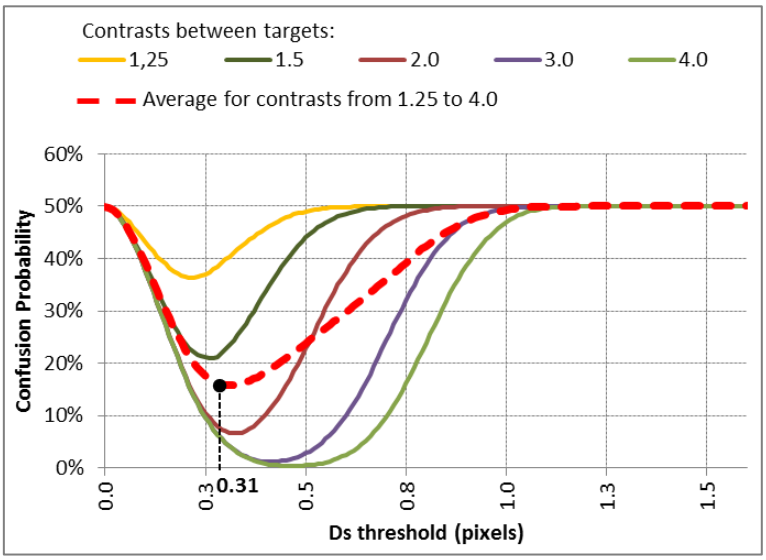

Fig. 7. Confusion probability when using the Ds operator as an edge detector, as a function of the Ds threshold used and for different contrasts between targets (11x11 window, edge geometry A, SAR ENL=4).

Optimal *Ds* thresholds were computed for edge geometries A, B, C and D, and for different window sizes by minimizing the integral of the confusion probability curves from contrast 1.25 to 4.0. Fig. 8 illustrates the confusion probability computed for optimal Ds thresholds, as a function of the processing window size and contrast, and for edge geometry A.

Fig. 9 depicts the confusion probability associated to edge geometries A, B, C and D for their corresponding optimal *Ds* thresholds. The confusion probability of the *CV* and the ratio edge detector r_2 [11] for the same geometries, and also for their best performance thresholds computed in the same way than for Ds, is plotted for comparison. Note that for the computation of r_2's confusion probability, the inequalities in (4) need to be inverted because r_2 takes higher values on homogeneous windows than on heterogeneous ones.

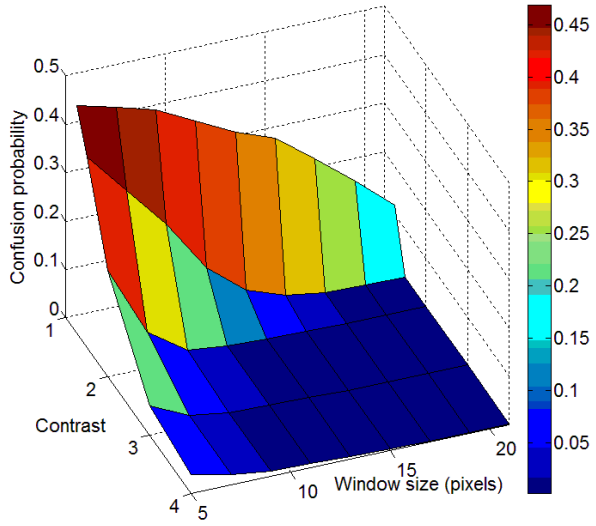

Fig. 8. Confusion probability computed for the optimal *Ds* threshold at each window size (edge geometry A and ENL=4).

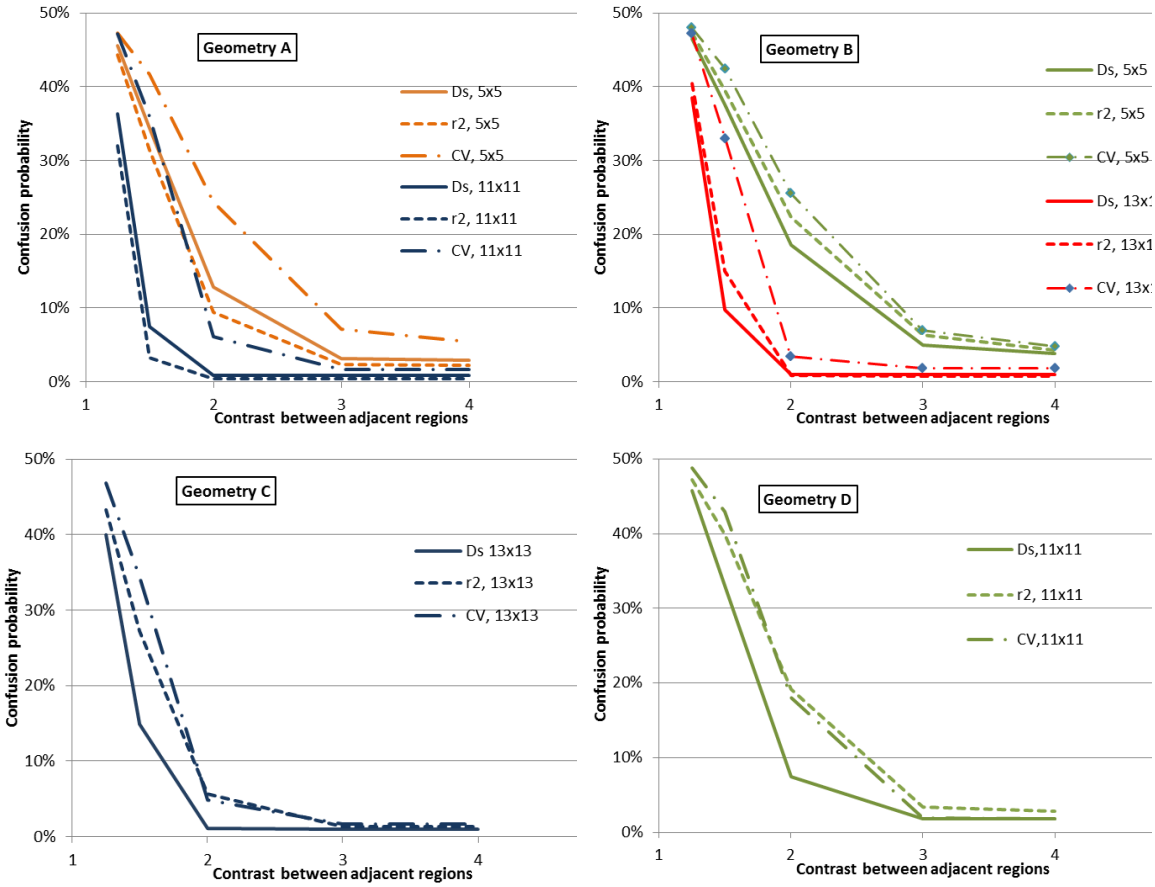

Fig. 9. Confusion probability of *Ds*, *CV* and r_2 for different window sizes for heterogeneous target structures A, B, C and D. The confusion probabilities correspond to the optimal thresholds (ENL=4).

Fig. 9 A, B and C illustrate the capacity of the *Ds*, r2 and CV operators to spot the presence of a boundary through the processing window center. These figures reveal that all three operators perform well at spotting edges between targets with contrast higher than 3. For lower contrasts and geometries A and B, Ds and r2 show better edge sensitivity than CV. r2 yields slightly lower confusion probability than Ds for geometry A, though their sensitivities get closer with increasing window sizes. The relative performance of both operators is approximately inverted for geometry B. In the case of the irregular edge C, Ds shows the lowest confusion probability. Other irregular edges were tested and yielded similar results. However, the possible irregular geometries are countless, and no general conclusions are attempted for them in this article.

Plot 8.D compares the capacity of *Ds*, *r2* and *CV* to detect non-stationarity due to the presence of a non-centered edge (geometry D in Fig. 4). *CV* makes use of the one-dimensional information of the window histogram to assess stationarity, while the two-dimensional

information contained in the pixel values spatial distribution, regarding the isotropy-anisotropy of the target, is omitted. *Ds* exploits this spatial information and, in light of Fig. 9.D, leads to lower false alarm plus missed detection rates than *CV*, for edges non-centered within the processing window.

2.3 Use of Ds for the assessment of target homogeneity in multi-resolution filtering

A key issue in multi-resolution filtering is to determine the largest stationary window where the filtering algorithm can be applied. Implementing the Ds operator for this goal requires the use of thresholds dependent on the processing window dimension, so that the best edge presence/absence split value is used at each window size. Fig. 10 depicts the optimal thresholds found by minimizing the integral of the confusion probability for window sizes between 5x5 and 21x21 and different ENLs. Knowledge of the best performance threshold trends, as provided by Fig. 10, can greatly assist the selection of these values, which are critical for the quality of the results. These trends have been used in the multi-resolution filtering of Doñana ASAR scenes, presented in the next section.

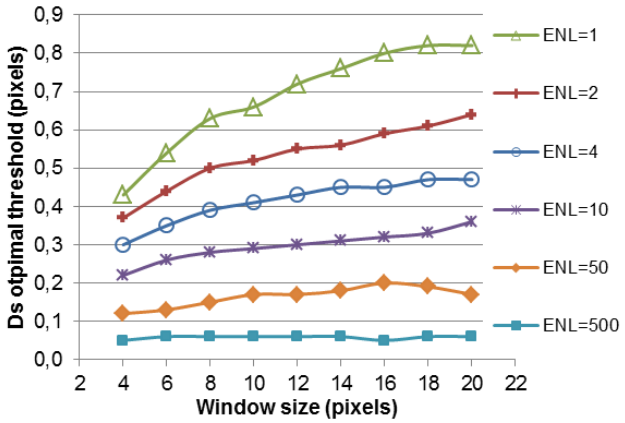

Fig. 10. Optimal *Ds* thresholds as a function of window size, for different ENL's (geometry A).

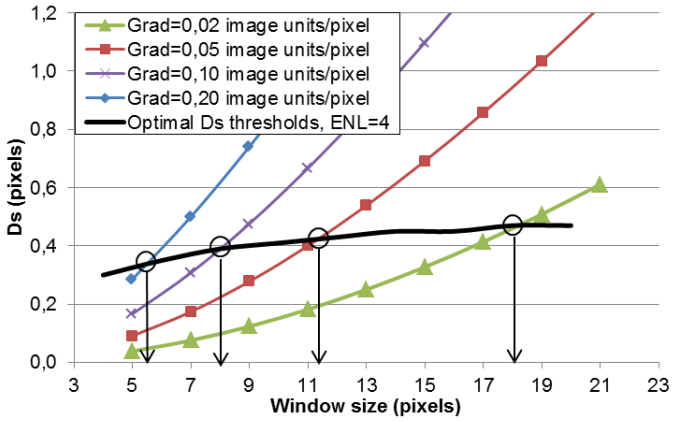

Fig. 11. Ds values of transitional targets with different gradients and maximum stationary window size for filtering purposes.

Gradual boundaries or transitions between targets, sketched in Fig. 4.E, can be modeled as consecutive edges of very low contrast. If *Ds* is used on this target type to determine the largest stationary neighborhood, this will depend on the target gradient magnitude, i.e., the maximum ratio between pixel increments in value and distance on the image. Fig. 11 shows this dependence: average *Ds* values of gradual boundaries are plotted as a function of window size for three different gradients. The intersections of these curves with the line of Ds thresholds show the window size that would be chosen for filtering each transitional area. It can be seen that, the lower the image gradient, the larger the filtering window size.

Several authors have proposed multi-resolution speckle filtering algorithms exploiting the conjunctive use of the *CV* and r_2 operators for the detection of stationary-nonstationary state [12], [13], [14], [15], [16]. In [16], after discarding the presence of an edge through the center pixel by thresholding r_2, significant increments in the *CV* and r_2 values were successfully used to spot the introduction of new targets during the window expansion. The sensitivity of *Ds* increments for the same goal has been tested and compared to the r_2's and CV's. The dots in Fig. 12 show the average *Ds*, *CV* and r_2 values in a processing window incorporating two columns of a new target B. The black lines depict the average Ds, CV and r2 values for homogeneous windows. The distance of the dots to the black lines indicates the expected increment in Ds, CV and r2 caused by the introduction of a new target B during the filtering window expansion. As intuitively expected, r_2 increments decrease with the window size, since the larger the processing window, the smaller the ratio represented by the new target area. Conversely, *Ds* increments keep increasing given that values in the periphery of the processing window contribute with a higher weight in the computation of *Ds* than those in the center.

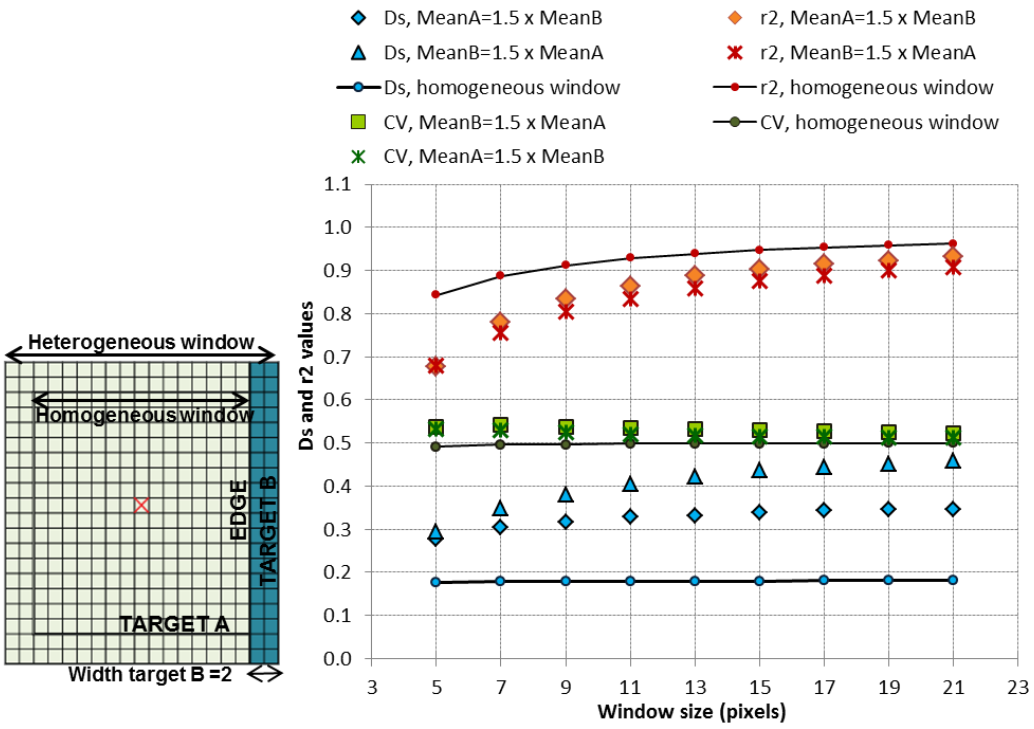

Fig. 12. Average *Ds*, r_2 and *CV* values when the processing window encompasses 2 columns of a new target (contrast between adjacent targets: 1.5; image ENL assumed in the simulations: 4).

3. USE OF *DS* OPERATOR IN THE MULTIRESOLUTION FILTERING OF DOÑANA ENVISAT/ASAR SCENES

3.1 Site description

Doñana wetlands extent over 30,000 ha on the right bank of the Guadalquivir River, near its mouth on the Atlantic Ocean coast. The wetlands undergo yearly cycles of inundation in fall and drying out at the end of the spring season, with a flood extension varying considerably among years [1], [2], [4].

In Doñana there are virtually no man-made structures. Edges occur in the contact between different land cover types or between flooded and emerged land. They are very often associated to the terrain contours, with capricious geometries, and normally are not as sharp as crop boundaries or roads, but show some sort of transition. Due to the terrain flatness, even the inundation perimeter often becomes a wide swamped strip.

At the end of the wintertime vertical stalks of helophyte vegetation start emerging sparsely from large part of the flooded areas [3]. In this situation, high CV's have been observed on SAR images due, presumably, to the different helophyte developmental stage of neighboring pixels. As a consequence of the large CV values, some common speckle filters reduce the filtering degree and large intensity fluctuations remain, complicating the classification of those areas as a single cover type.

3.2 Imagery data

More than forty Envisat/ASAR scenes of Doñana marshes were acquired from fall 2006 to summer 2007 with the main purpose to monitor the flood extent evolution [5]. The images were acquired in Alternated Polarization and Image Modes, with HH/VV and HH polarization configurations, respectively, and using the seven ASAR's predetermined incidence angles or swaths [19]. Both acquisition modes had an azimuth and range resolution of 30 m. The image product provided by the European Space Agency had a pixel spacing of 12.5 m and the ENL indicated in Table 1 for each incidence angle [20]. The scenes were calibrated to backscattering coefficient as explained in [5].

Table 1. ASAR incidence angles, their ENL and number of Doñana scenes acquired from fall 2006 to summer 2007.

ASAR swath	IS1	IS2	IS3	IS4	IS5	IS6	IS7
Incidence angle range (º)	15.0-22.9	19.2-26.7	26.0-31.4	31.0–36.3	35.8-39.4	39.1-42.8	42.5-45.2
ENL	1.76	1.73	2.25	2.66	3.30	3.78	3.73

3.3 Methodology

Delineation of the flooded areas from the ASAR imagery required filtering the scenes to smooth out backscattering fluctuations owing to speckle and texture within cover classes. Filtering was carried out in a multi-resolution fashion and the *Ds* value was used to decide on the maximum stationary window: the processing window becomes as large as 21x21 pixels in homogenous areas and is progressively reduced when approaching edges, so that it does not ride over different land cover types. In presence of gradual boundaries, the filtering window size adapts to the gradient steepness.

The ASAR image products showed a significant spatial correlation between contiguous pixels due to the fact that the pixel spacing (12.5 m) is lower than half the sensor's spatial resolution (30 m). The assessments and thresholds derived in Section 2 assumed that the pixel values were spatially independent realizations of a given statistical distribution. In order to decorrelate the ASAR pixels, new images were formed by selecting every other pixel from the original ones. Combining odd/even row with odd/even column pixels, four half size images were obtained from each ASAR one. Fig. 13 shows the decomposition of an ASAR image fragment into four half-size fragments of approximately spatially uncorrelated pixels

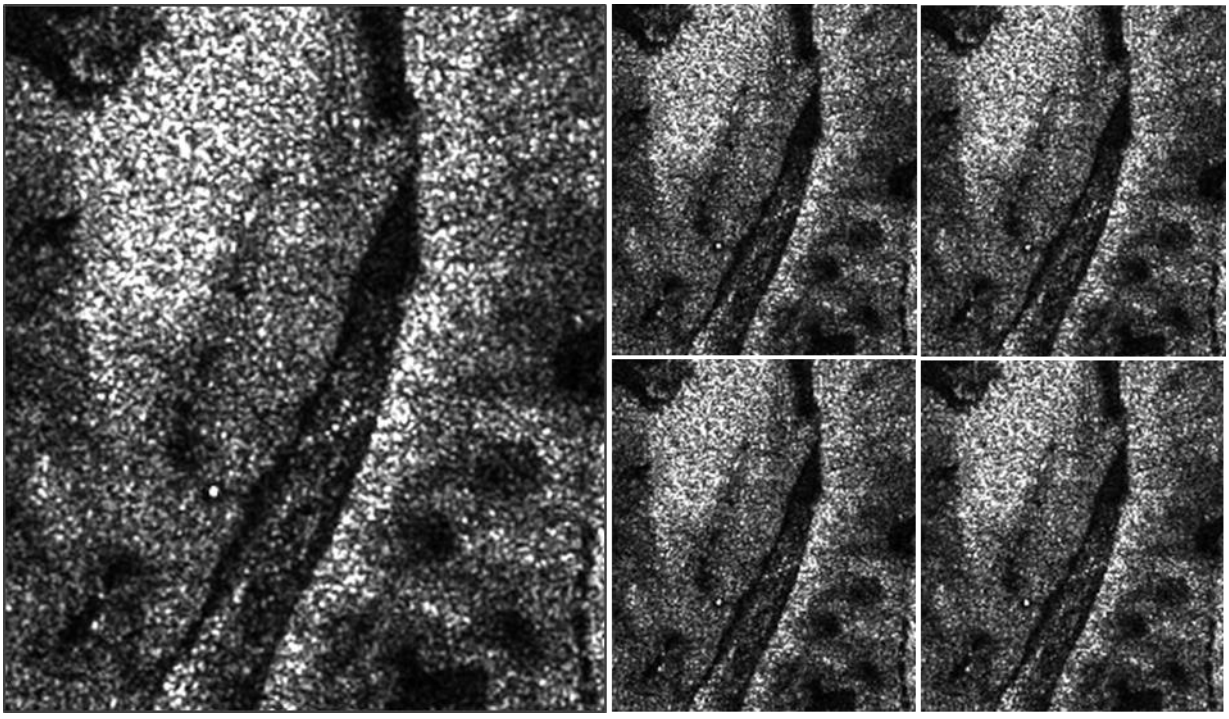

Fig. 13. Decomposition of an ASAR image fragment into four half-size fragments of approximately spatially decorrelated pixels. The image was acquired at VV polarization and swath IS6 on 27 Feb. 2007. The ASAR image product had an ENL of 3.78.

The *Ds* parameter was computed at every pixel of the four sub-sampled images for odd window sizes ranging from 5x5 to 21x21. The Ds values were then placed back to their corresponding pixel's original location in the full-size ASAR image. Fig. 14 depicts the Ds values obtained for the image in Fig. 13 and for a 9x9 processing window. CV and r2 are also depicted for comparison. The filtering method presented as follows used the full-size Ds and ASAR images.

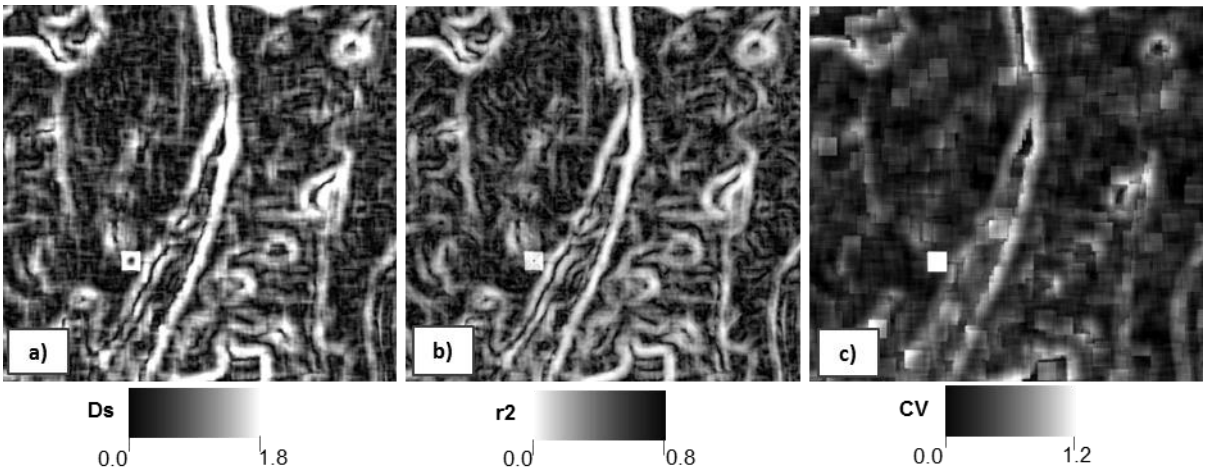

Fig. 14. Ds, r2 and CV values obtained for the image in Fig. 13 and depicted as gray-scale images.

The optimal set of *Ds* thresholds as a function of the window size was selected accordingly with the scene ENL (Fig. 10). The *Ds* values at each pixel (i,j) are compared to the thresholds of the corresponding window sizes *Th*(L), starting from LxL=5x5. If *Ds*(5)<*Th*(5) then pixel (i,j)'s neighborhood is considered isotropic at least in a 5x5 window. For progressively increasing odd-side windows the conditions (5) and (6) below are tested. Fig. 15 assists their interpretation:

$$Ds(L+2) < Th(L+2), \text{ at pixel (i,j) to be filtered} \quad (5)$$

$$Ds(L) < Th(L), \text{ for all pixels contiguous to (i,j)} \quad (6)$$

Only if both conditions (5) and (6) are satisfied, window (L+2)x(L+2) is considered isotropic and the next window size is assessed in a similar way, up to a maximum size of 21x21. If one of the above conditions is not fulfilled, then LxL is taken as the maximum isotropic window, which is used for filtering pixel (i,j).

Fig. 15 depicts an (L+2)x(L+2) window centered on pixel (i,j). Pixels contiguous to (i,j) are indicated with rings and the LxL sub-windows for two of them are highlighted with grey and hatched backgrounds. Windows centered on symmetric features, such as curvilinear features (e.g. narrow water courses) or strong backscatterers, yield low *Ds* values and could be confused as isotropic neighborhoods by condition (5). Condition (6) assures that isotropy is accomplished in non-centered sub-windows, preventing that sort of confusion.

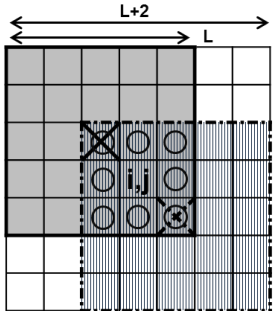

Fig. 15. Pixels contiguous to (i,j) and the LxL sub-windows for two of them.

If *Ds*(L)<*Th*(L) is not satisfied for the starting window size 5x5, *Ds* is computed for all 3x3 windows which include the pixel to be filtered (i,j) at any position. If the minimum resultant *Ds* is lower than threshold *Th*(3), then pixel (i,j) is filtered out using the values within the minimum *Ds* 3x3 window. Otherwise (i,j) is left unfiltered.

Once the maximum isotropic window had been determined following the methodology above, the pixel's filtered value was determined by simply averaging the window's intensities, since it was assumed that isotropic neighborhoods corresponded to a single cover type, the aim of the filtering was a subsequent classification and texture preservation was not a requirement.

3.4 Results and discussion

Fig. 16, Fig. 17 and Fig. 18 show fragments of ASAR image products calibrated to backscattering coefficient and their filtered versions using the methodology described in the previous section. These sample ASAR images correspond to different incidence angles, polarizations and marshes phenological stages. Fig. 16 and Fig. 17 also present the maximum isotropic window size determined by Ds thresholding and used for computing the pixels' filtered value. The window size ranges from 1 for unfiltered pixels to 21 in the largest isotropic areas. Fig. 18 includes sample data profiles of the calibrated and filtered images.

The data profile in Fig. 18 reveals the high degree of speckle reduction achieved, which greatly facilitates the segmentation of the ASAR images. The filtering window size depicted in Fig. 16c and Fig. 17c shows the adaptation of this window to the sharpness of the image structure, which is accomplished by means of the *Ds* parameter thresholding. Filtering windows are progressively reduced when approaching a sharp edge, intermediate sizes are adopted in the transition areas depending on the gradient gentleness and the maximum size is reached over isotropic regions.

In the processed images, the *Ds* thresholds used to decide on the windows' isotropy were somewhat higher than those presented in Fig. 10. The latter optimal thresholds were computed assuming non-textured homogeneous targets, with pixel backscattering coefficients being independent realizations of the same gamma distribution. Certain Doñana marshes covers exhibit some texture. As a result, the *Ds* standard deviation to mean ratio on the real scenes is larger than those on the simulated ones. This is presumably the reason why the optimal thresholds turned out to be greater too. However, the thresholds satisfactorily used for filtering the Doñana images followed an increasing trend proportional to that found for synthetic targets. This allowed investigating just one scaling factor for the corresponding ENL Ds trend, instead of assessing new Ds thresholds for every filtering window size.

No especial treatment was given to the signal from strong scatterers. Model-based filtering algorithms generally detect the presence of such targets and preserve their signals, because they do not exhibit speckle fluctuations [9]. In Doñana there are some metal fences and gauging station cages, both behaving as strong backscatterers (e.g. at the top left of Fig. 16). The location of fences and cages is precisely known, so they can be masked out and a detection algorithm of this target type is not required. However, such a detector could be easily incorporated as a first step into the presented methodology for its application to SAR images of other environments.

Further application examples of the Ds operator for the filtering and classification of Doñana ASAR scenes can be found in [21] and [22].

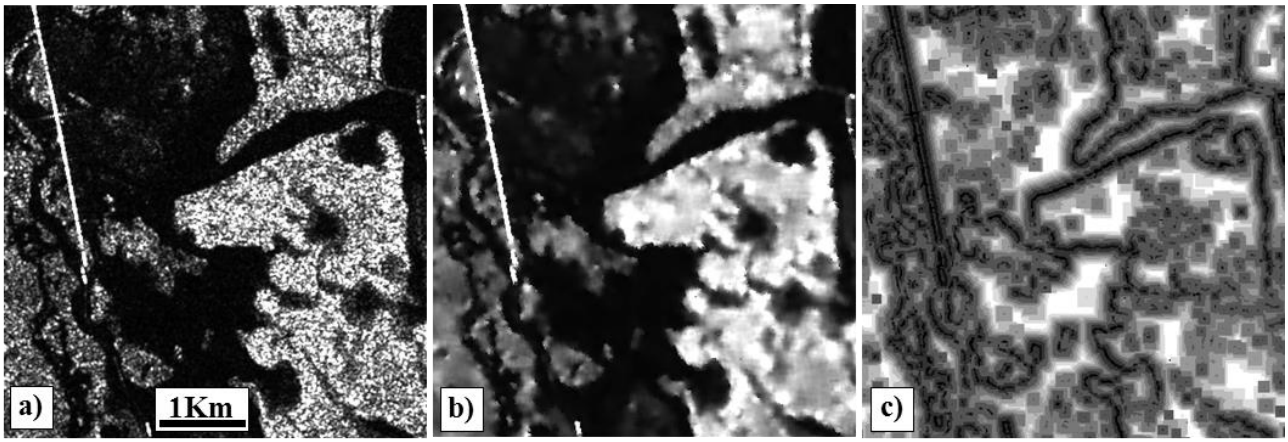

Fig. 16. Area in Doñana marshes captured by ASAR on 22 November 2006 at swath IS6 and HH polarization: a) image calibrated to backscattering coefficient; b) filtered image; c) filtering window size (from 1x1 in black to 21x21 in white).

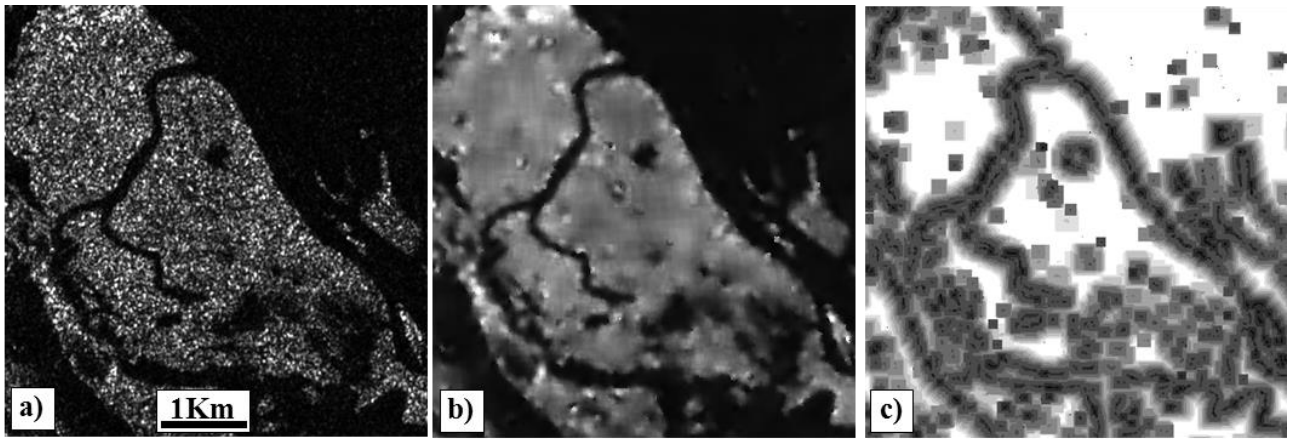

Fig. 17. Area in Doñana marshes captured by ASAR on 02 March 2007 at swath IS4 and HH polarization: a) image calibrated to backscattering coefficient; b) filtered image; c) filtering window size (from 1x1 in black to 21x21 in white).

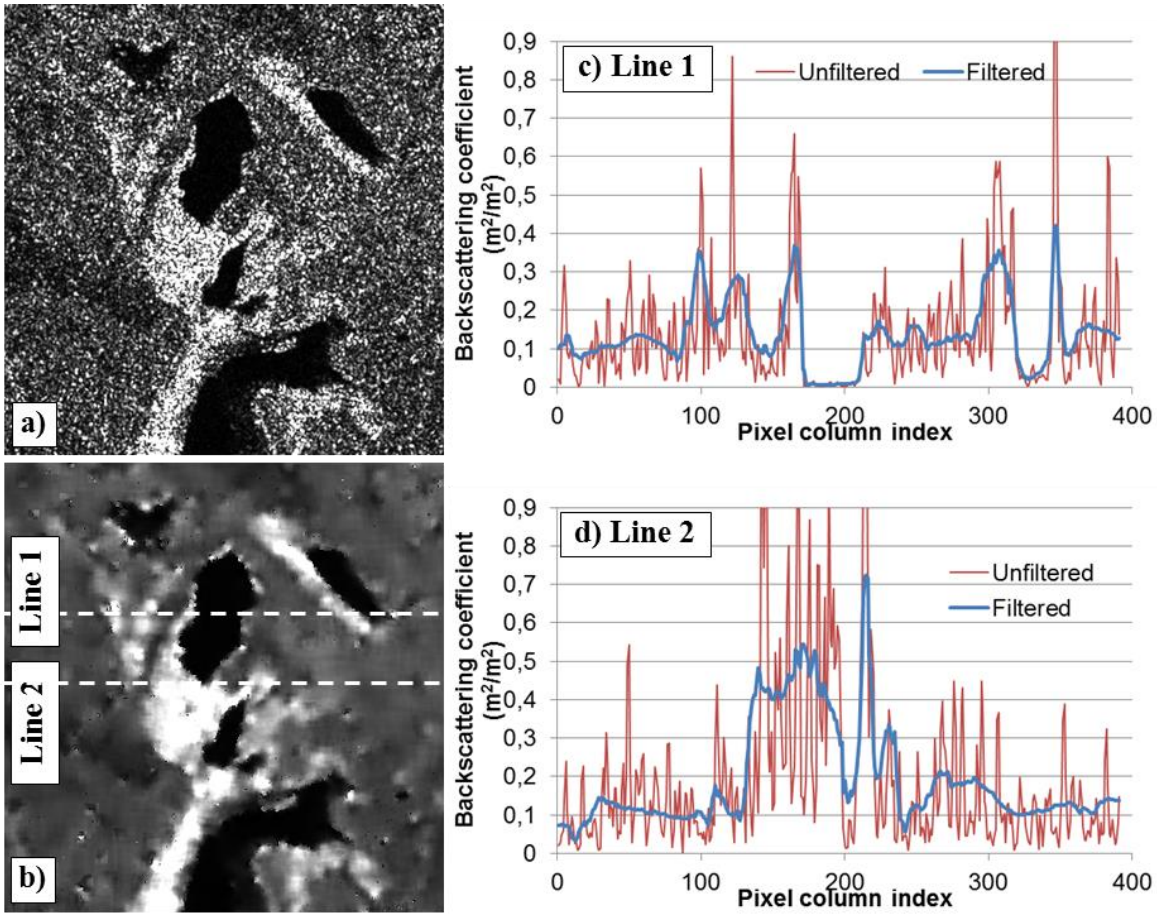

Fig. 18. Area in Doñana marshes captured by ASAR on 30 June 2007 at swath IS2 and VV polarization: a) image calibrated to backscattering coefficient; b) filtered image; c) and d) original and filtered data profiles.

4. CONCLUSIONS

A new operator, named *Ds*, has been proposed for local isotropy assessment on SAR images. *Ds* is rotationally invariant, and its calculation indicates the direction of the main intensity imbalance in the processing window. When filtering SAR images, the speckle statistical properties are introduced to determine suitable Ds thresholds for discriminating heterogeneous targets from textured cover types at different window sizes.

Simulations of the confusion probability have shown similar edge sensitivity of *Ds* compared to that of the r2 detector in presence of straight, sharp, centered boundaries. In the case of non-centered ones, Ds performs notably better than r2 and CV, which makes this operator more appropriate to spot the inclusion of heterogeneities during the processing window expansion in multi-resolution filtering.

The motivation for using the Ds parameter was that some natural areas in the Doñana marshes ASAR images show relatively high CV, and large pixel intensity fluctuations remain after applying common filtering algorithms. In this study, isotropic neighborhoods are assumed to correspond to a single cover type and the intensities within were averaged regardless their CV, in order to flatten fluctuations and facilitate a subsequent land cover classification.

The use of *Ds* in a multi-resolution fashion for filtering Doñana marshes ASAR scenes has substantiated the usefulness of such operator. The results show the adaptation of the processing window size to the sharpness of the image structure, which is accomplished by means of the *Ds* thresholding; filtering windows are progressively reduced when approaching a sharp edge, intermediate sizes are adopted in the transition areas depending on the gradient gentleness and the maximum size is reached over homogeneous regions. The homogeneity-heterogeneity *Ds* threshold selection for each window size was considerably simplified by using the optimal threshold trend corresponding to the scene ENL, although at least one absolute value needs to be adjusted by the user to set the scale of the trend.

5. ACKNOWLEDGEMENTS

The ASAR data used in this study was provided by the European Space Agency within the frame of a Category 1 User Agreement with the Flumen Institute. The research has been funded by the Plan Nacional de I+D+i of the Spanish Ministerio de Ciencia e Innovación (projects CGL2006-02247 and CGL2009-09801) and by the Agencia Andaluza del Agua of the Junta de

Andalucía. The authors would also like to express their gratitude to the Col·legi d'Enginyers de Camins, Canals i Ports de Catalunya for their important sponsorship to PhD students, to Dr. Juan José Egozcue from the Universitat Politècnica de Catalunya for his knowledgeable and gentle advice, and to the researchers of the Espacio Natural de Doñana and the Estación Biológica de Doñana for their continuous support.

6. REFERENCES

[1] B. Bayán-Jardín and J. Dolz-Ripollés, "Las aguas superficiales y la marisma del Parque Nacional de Doñana", *Revista de Obras Públicas*, 3340, pp. 17−29, 1995.

[2] Clemente, L., García, L. V., Espinar, J. L., Cara, J. S., & Moreno, A. (2004). Las marismas del Parque Nacional de Doñana. Investigación y Ciencia (pp. 332).

[3] García, J. I., Mintegui, J. A., & Robredo, J. C. (2005). La vegetación en la marisma del parque nacional de Doñana en relación con su régimen hidráulico. Madrid, Spain: Ministerio de Medio Ambiente.

[4] L. Serrano, M. Reina, G. Martín, I. Reyes, A. Arechederra, D. León and J. Toja, "The aquatic systems of Doñana (SW Spain): watersheds and frontiers", *Limnetica*, 25(1-2), pp. 11-32, 2006.

[5] B. Marti-Cardona, C. Lopez-Martinez, J. Dolz-Ripolles and E. Bladè-Castellet, "ASAR polarimetric, multi-incidence angle and multitemporal characterization of Doñana wetlands for flood extent monitoring," *Remote Sensing of Environment*, vol. 114, pp. 2802–2815, Nov. 2010.

[6] J. S. Lee, "Digital image enhancement and noise filtering by use of local statistics," *IEEE Trans. Pattern Anal. Machine Intell.*, vol. PAMI-2, pp.165–168, 1980.

[7] V. S. Frost, J. A. Stiles, K. S. Shanmugan, and J. C. Holtzman, "A model for radar images and its application to adaptive digital filtering of multiplicative noise," *IEEE Trans. Pattern Anal. Machine Intell.*, vol. PAMI-4, pp. 157–166, 1982.

[8] D. T. Kuan, A. A. Sawchuk, T. C. Strand, and P. Chavel, "Adaptive noise smoothing filter for images with signal-dependent noise," *IEEE Trans. Pattern Anal. Machine Intell.*, vol. PAMI-2, pp. 165–177, 1985.

[9] J. W. Goodman, *Laser speckle and related phenomena*, J. C. Dainty Ed., New York: Springer-Verlag, 1975.

[10] J.S. Lee, "Refined filtering of image noise using local statistic," *Computer graphics and image processing*, Vol.24, pp.255-269, 1983.

[11] R. Touzi, A. Lopes, and P. Bousquet, "A statistical and geometrical edge detector for SAR images," *IEEE Trans. Geosci. Remote Sensing*, vol. 26, pp. 764–773, Nov. 1988.

[12] A. Lopes, R. Touzi, and E. Nezry, "Adaptive speckle filters and scene heterogeneity," *IEEE Trans. Geosci. Remote Sensing*, vol. 28, pp. 992–1000, Nov., 1990.

[13] E. Nezry , A. Lopes and R.Touzi, "Detection of structural and textural features for SAR images filtering," *Proc. of IGARSS'91*, Espoo, Vol.4, pp.2169-2172, Jun. 1991.

[14] Y.L. Desnos and V. Matteini, "Review on structure detection and speckle filtering on ERS-1 images," *EARSeL Advances in Remote Sensing*, Vol. 2, No.2- VI, pp. 52-65, 1993.

[15] A. Lopes, E. Nezry, R. Touzi, and H. Laur, "Structure detection and statistical adaptive speckle filtering in SAR images," *Int. J. Remote Sens.*, vol. 14, pp. 1735–1758, 1993.

[16] R. Touzi, "A review of speckle filtering in the context of estimation theory", *IEEE Trans. Geosci. Remote Sensing*, vol. 40, no. 11, pp. 2392–2404, Nov. 2002.

[17] A. Baraldi and F. Parmiggiani, "A refined gamma MAP SAR speckle filter with improved geometrical adaptivity", *IEEE Trans. Geosci. Remote Sensing*, vol. 33, pp. 1245–1257, Sep. 1995.

[18] C. Oliver and S. Quegan, *Understanding synthetic aperture radar images*, SciTech Publishing Inc., Raleigh, NC, 2004.

[19] European Space Agency, *ASAR product handbook*, ESA, 2006.

[20] European Space Agency, *Envisat ASAR monthly reports*, 2007, (available at http://earth.eo.esa.int/pcs/envisat/asar/public_reports/).

[21] B. Martí-Cardona, J. Dolz-Ripollés and C. López-Martínez, "Wetland inundation monitoring by the synergistic use of ENVISAT/ASAR imagery and ancilliary spatial data", *Remote Sensing of Environment*, vol. 139, no. 12, pp. 171–184, Dec. 2013. Doi:10.1016/j.rse.2013.07.028.

[22] A. Ramos-Fuertes, B. Martí-Cardona, E. Bladé and J. Dolz, "Envisat/ASAR images for the calibration of the wind drag action in Doñana wetlands 2D hydrodynamic model", *Remote Sensing*, vol. 6, no. 1, pp. 379-406, Dec. 2013. Doi:10.3390/rs6010379.